Multispectral Remote Sensing and Spatiotemporal Mapping of the Environment and Natural Disasters Using Small UAS

Saket Gowravaram

Submitted to the graduate degree program in Department of Aerospace Engineering and the Graduate Faculty of the University of Kansas in partial fulfillment of the requirements for the degree of Doctor of Philosophy.

Committee members

Dr. Haiyang Chao, Chairperson

Dr. Craig McLaughlin

Dr. Zhi Jian Wang

Dr. Huixuan Wu

Dr. Jude Kastens

Dr. Joshua Roundy

Date Defended: Jan 28, 2022

The Dissertation Committee for Saket Gowravaram certifies
that this is the approved version of the following dissertation :

Multispectral Remote Sensing and Spatiotemporal Mapping of the Environment and Natural Disasters Using Small UAS

Dr. Haiyang Chao, Chairperson

Date approved: Jan 28, 2022

Abstract

This dissertation focuses on development of new methods for multispectral remote sensing, measurement, and mapping of the environment and natural disasters using small Unmanned Aircraft Systems (UAS). Small UAS equipped with multispectral cameras such as true color (RGB), near infrared (NIR), and thermal can gather important information about the environment before, during, and after a disaster without risking pilots or operators. Additionally, small UAS are generally inexpensive, easy to handle, and can detect features at small spatiotemporal scales that are not visible in manned aircraft or satellite imagery. Four important problems in UAS remote sensing and disaster data representation are focused in this dissertation. First, key considerations for the development of UAS disaster sensing systems are provided, followed by detailed descriptions of the KHawk system and representative environment and disaster data sets. Second, a new method is proposed and demonstrated for accurate mapping and measurement of grass fire evolution using multitemporal thermal orthomosaics collected by a fixed-wing UAS flying at low altitudes. Third, a low-cost and effective solution is further developed for spatiotemporal representation and measurement of grass fire evolution using time-labeled UAS NIR orthomosaics and a novel Intensity Variance Thresholding (IVT) method is proposed for grass fire front extraction to support fire spread metrics measurement of fire front location and rate of spread (ROS). A UAS grass fire observation data set is also presented including thermal and NIR orthomosaics and supporting weather and fuel data. Fourth, a new Satellite-based Cross Calibration (SCC) method is proposed for surface reflectance estimation of UAS images in digital numbers (DN) using free and open calibrated satellite reflectance

data. This also serves as a solid foundation for data-enabled multiscale remote sensing and large scale environmental observations. Finally, the main conclusions and future research considerations are summarized.

Acknowledgements

I would first like to thank my parents, Susmita Gowravaram and Sivaramakrishna Gowravaram, and my late grandmother Syamala Kamaraju for their love and support. If not for you, I would not have had the strength, confidence, or character to battle difficult obstacles in my career and personal life. Thanks for all your sacrifices, I will never forget them.

I owe my professional achievements to my Ph.D. advisor, Dr. Haiyang Chao. Thank you for trusting me and giving me the opportunity to work under your guidance. You taught me how to learn, how to conduct research, and more importantly how to solve difficult problems. Thank you for guiding me at all times and motivating me to reach higher and think bigger. I sincerely hope that I can continue to collaborate with you and learn from you well into my professional life. I promise you that I will always ask myself, "What is new and who will benefit from my work?".

I would like to thank my Ph.D. committee members for being patient with me and reviewing my work and provide constructive criticism. A special thank you to Dr. ZJ Wang, who has recommended me and helped me gain important opportunities during my graduate studies.

Thanks to all my research collaborators, Dr. Tiebiao Zhao, Sheena Parsons, Dr. Guanghui Wang, and Dr. Andrew Molthan for your expert opinions and many constructive meetings. I thank my colleagues at the CUSL Lab, Dr. Pengzhi Tian and Dr. Harold Flanagan who trained me and helped me fit in at very early stage. Thank you also to Jacksen Goyer, Justin Matt, Zhenghao Lin, and Mosarruf Hossain for your contributions in the lab and flight test participation.

Finally, I would like to acknowledge the funding support: KU Research GO Grant, US Department of Agriculture NIFA NRI Grant, Kansas Water Research Institute, and the NASA EPSCoR Grant. I would also like to thank the KU Department of Mathematics and Dr. Joseph Brennan for giving me the opportunity to serve as a Graduate Teaching Assistant during the first year of my Ph.D.

Contents

List of Figures

List of Tables

Chapter 1

Introduction

1.1 Dissertation Roadmap

This dissertation focuses on development of new methods for multispectral remote sensing, measurement, and mapping of the environment and natural disasters using small Unmanned Aircraft Systems (UAS). Multispectral images from UAS are already being used in many civilian and military applications including precision agriculture, structural inspection, surveillance, search & rescue, vegetation damage assessment, and post-disaster mapping. The increased frequency and severity of natural disasters including wildfires, floods, hail storms, and tornadoes demand more accurate and robust observation systems that can not only assist in post-disaster recovery but can also measure important spatiotemporal metrics of disasters. For example, location, spread direction, and spread speed of a fast-evolving wildfire or flood, origin of a chemical leak, and tornado damage intensity. Small UAS equipped with multispectral cameras can gather this information without risking pilots or operators, especially since they are inexpensive, easy to handle, and can detect features at small spatiotemporal scales that are not visible in manned aircraft or satellite imagery. However, several critical challenges have to be addressed before wide uses of UAS in such applications. For instance, how can a low-flying UAS be used for accurate mapping and quantitative measurement of fast-evolving large-scale environmental processes like wildland fires or floods? Is there a low-cost and safe UAS solution for accurate observation and mapping of large scale wildland fires? How can UAS multispectral maps be integrated with existing satellite observations for enhanced observations of environment and disasters? This dissertation answers these questions by developing, demonstrating, and validating novel methods in real-world scenarios. Ad-

ditionally, this dissertation also shares important discussions and lessons learned that will greatly contribute towards wider and more efficient uses of small UAS in mapping and measurement of the environment and natural disasters.

1.2 Research Motivations

The main motivation of this dissertation is to develop effective and robust UAS remote sensing methods for accurate mapping and measurement of the environment and natural disasters that may be difficult to obtain using other remote sensing systems such as manned aircraft and satellites. Multispectral remote sensing includes sensing in true color (RGB), near infrared (NIR), and thermal bands. Images in different bands can be used to infer different properties of the environment and disasters. For example, in fire monitoring applications, RGB images can be used for smoke detection and situational awareness, NIR images can be used to differentiate burned and unburned areas, and thermal images are generally used for fire front extraction and temperature measurement (see Fig. 1.1).

Figure 1.1: Aerial view of a prescribed grass fire from RGB (left), NIR (center), and thermal cameras (right).

The vision of this dissertation is to acquire, calibrate, represent, and integrate new UAS data into existing environment and disaster mapping products from manned aircraft and satellites, and to support future multiscale and multisource remote sensing. The objective of such an integrative multisource system is to maximize the desirable characteristics of each remote sensing system. For example, UAS can provide data and measurements at high spatiotemporal resolutions while satellites and manned aircraft can provide coarser measurements with large area coverage and reliable

spatial and spectral properties, as illustrated in Fig. 1.2. Such systems can greatly enhance earth observations and enable better understanding of environmental processes and natural disasters.

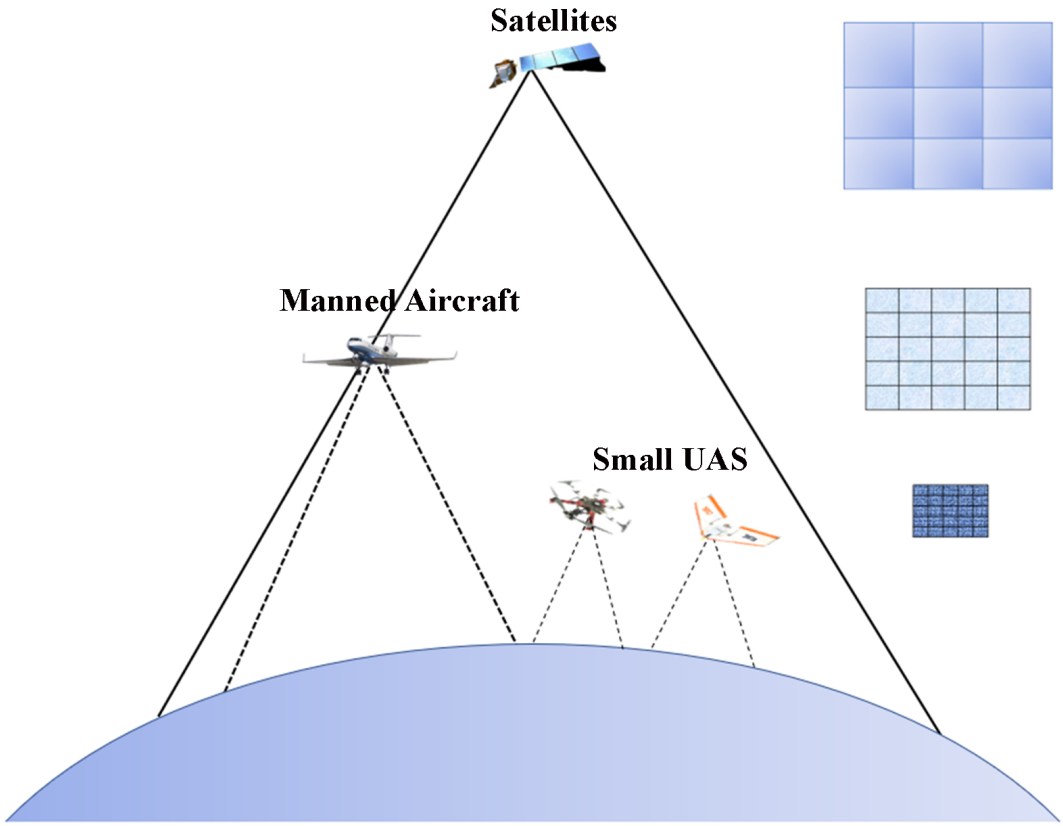

Figure 1.2: Multiscale remote sensing systems.

1.2.1 Role of Small UAS in Environment and Natural Disaster Mapping

Small UAS can contribute to existing environment and disaster mapping and measurement systems in the following ways.

1. Quick deployment before, during, and after a disaster for quick data acquisition and situational awareness;

2. Close observations of disaster evolution;

3. Quantitative measurement of location, spread speed, and direction of fast-evolving processes at high spatial and temporal resolutions;

4. Provide accurate measurements that can be used to evaluate and improve disaster spread models such as fire spread models;

5. Acquire data between satellite and aircraft flybys;

6. Acquire information over fields that may be obstructed by clouds in satellite images.

1.2.2 Challenges of Small UAS in Environment and Natural Disaster Mapping

Major challenges that limit the use of UAS in disaster mapping missions include:

1. Safe and efficient operations in dangerous disaster environments;

2. accurate recapture or reconstruction of a fast-evolving process using UAS images with limited footprints;

3. Many UAS operators are limited by budget and cannot afford expensive cameras that are often required for accurate measurements;

4. UAS multispectral data require vicarious radiometric calibration for reflectance estimation and comparison with data from other sources.

This dissertation mainly addresses challenges 2-4. Chapters 3 & 4 provide solutions to challenges 2 and 3 by developing novel methods for the accurate mapping and measurement of grass fire metrics such as location and ROS using thermal and low-cost NIR cameras. Chapter 5 addresses challenge 4 by proposing a new satellite-based cross calibration method for UAS reflectance estimation.

1.3 Dissertation Contributions

The main contributions of this dissertation can be summarized as follows:

1. Developed a new and effective method for accurate recapturing of grass fire evolution using multitemporal thermal orthomosaics collected by a small fixed-wing UAS at low altitude;

2. Developed a new and low-cost method for the spatiotemporal representation and measurement of grass fire evolution using time labeled NIR orthomosaics from a small fixed-wing UAS;

3. Invented a novel NIR intensity variance thresholding method for grass fire front classification and extraction;

4. Conducted comprehensive measurement, analysis, and validation of prescribed fire ROS in a typical tallgrass prairie, which has not been sufficiently addressed in existing remote sensing literature;

5. Acquired, analyzed, and shared a UAS multispectral grass fire data set including thermal and NIR orthomosaics and supporting weather, terrain, and fuel data;

6. Developed a new and low-cost satellite-based cross-calibration method for UAS spectral reflectance estimation;

7. Provided comprehensive quantitative and qualitative comparisons between multiscale remote sensing images from KHawk UAS, NEON manned aircraft, and Landsat 8 satellite.

1.4 Dissertation Organization

This dissertation is organized as follows. Research motivations and dissertation contributions are summarized in Chapter 1. Important considerations for development of a UAS multispectral sensing system for disaster mapping applications are presented in Chapter 2 along with detailed descriptions of the KHawk system and representative disaster data sets. Chapter 3 focuses on the mapping and ROS measurement of a prescribed grass fire using multitemporal thermal orthomosaics that are generated from UAS aerial images with limited footprints. In Chapter 4, a low-cost

and effective NIR-based fire detection algorithm is introduced that can enable accurate mapping and measurement of grass fires without using expensive thermal cameras. Chapter 5 presents a novel satellite-based cross-calibration method for UAS spectral reflectance estimation using free and open satellite data. Finally, conclusions and future recommendations are provided in Chapter 6.

Chapter 2

UAS Development and Multispectral Data Acquisition for Disaster Mapping and Measurement

2.1 Chapter Introduction

This chapter focuses on important considerations for the successful design and use of Unmanned Aircraft System (UAS) for multispectral data acquisition missions to support disaster mapping, measurement, and analysis. Typical disaster applications include wildland fire metrics measurement (location, rate of spread (ROS)), hail, tornado, or storm damage assessment, and post-disaster vegetation recovery mapping. The main challenge for such missions is that they are often time-critical and require quick and accurate data acquisition and analysis. This is true not only for in-situ disaster sensing applications such as wildland fire monitoring, when the fire is still burning, but also for post-disaster applications such as hail or tornado damage assessment. For example, the UAS needs to be deployed for data acquisition over a tornado-affected field before it is recovered by residents or emergency response teams for accurate damage assessment. This means that there is generally a short time window available for the UAS to acquire useful disaster information. Therefore, the UAS flight path and associated sensing payload need to be well designed and integrated for successful data acquisition. This chapter presents the KHawk UAS multispectral remote sensing system and the disaster mission design strategies that are used for successful disaster mapping applications in this dissertation. Example KHawk disaster sensing missions are presented including the path planning and acquired multispectral data sets that can serve as a foundation for the following chapters.

2.2 UAS Multispectral Sensing System

A fleet of small KHawk fixed-wing UAS (shown in Fig. 4.1) were developed by the Cooperative Unmanned Systems Lab (CUSL) for multispectral remote sensing missions. These UAS are equipped with either a Paparazzi TWOG autopilot or a Pixhawk Cube autopilot and are capable of manual and autonomous flight with endurance of about 20-30 minutes. These platforms are light-weight (< 6 lbs. with payload), bungee-launched, and easy to handle. They are well-suited for dull, dirty, and dangerous missions such as fire monitoring and disaster reconnaissance.

Figure 2.1: KHawk fixed-wing UAS fleet.

The major aspect of designing a UAS disaster sensing system is the selection of multispectral cameras. Important considerations for the multispectral camera selection include, weight, size, spectral response, image resolution, update rate, field of view (FOV), and operational specifications, such as autopilot geo-tagging capabilities. Depending on whether the UAS is deployed for in-situ disaster mapping or post-disaster damage assessment, some of these considerations can

be further prioritized. For example. thermal cameras with autopilot geo-tagging capabilities are highly recommended for wildland fire mapping missions, while an NIR camera with high image resolution is preferred for tornado crop damage assessment missions. In this dissertation, three multispectral cameras are used for the acquisition of images in true color (RGB), near infrared (NIR), and thermal bands. Important specifications are provided in Table 2.1.

Table 2.1: KHawk UAS Multispectral Camera Specifications.

Properties	PeauPro82 RGB	PeauPro82 Modified NIR	FLIR Vue Pro R Thermal
Weight	90 g	90 g	142 g
Spectral Response	425.4 – 710 nm	630-880 nm	7.5-13.5 μm
Image Resolution	1920 $\times$ 1080 pix.	1920 $\times$ 1080 pix.	640 $\times$ 512 pix.
Update Rate	29.97 Hz	29.97 Hz	1 Hz
FOV	74°$\times$ 45°	74°$\times$ 45°	69°$\times$ 56°
Geo-Tagging	Manual Post-Processing	Manual Post-Processing	MAVlink-Pixhawk

2.2.1 KHawk RGB & NIR Sensing System

Two PeauPro82 GoPro Hero 4 cameras are selected and used for KHawk UAS RGB and NIR image acquisition. As shown in Table 2.1, these cameras are light-weight and acquire images at high-resolution, which are desired for successful post-disaster crop damage assessment. The NIR camera is modified using an NIR band pass filter and acquires images in red, green, and NIR bands. The spectral response for the red and NIR channels is shown in Fig. 2.2. These cameras are inexpensive and do not possess autopilot geo-tagging capabilities, which is one drawback of this system. For these cameras, the images can be geo-tagged post flight by manual synchronization with onboard GPS and IMU data [3].

One application of these cameras is for the estimation of vegetation indices such as the Normalized Difference Vegetation Index (NDVI). NDVI can be used to identify and quantify crop damage caused by disasters. In this dissertation, data from these cameras are used to develop a novel UAS reflectance estimation method using free and open satellite data, further discussed in chapter 5.

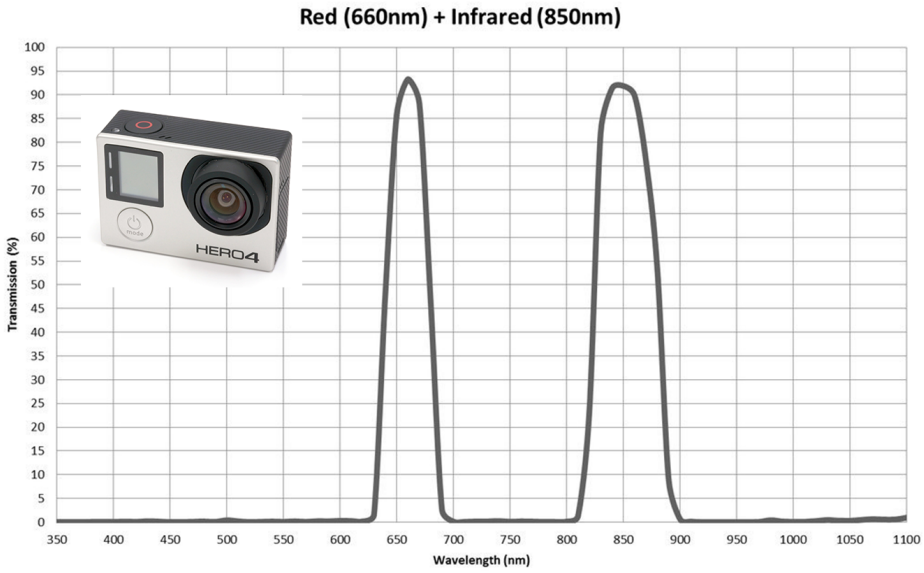

Figure 2.2: PeauPro82 modified NIR camera spectral response plot [1].

Additionally, the NIR camera is used to map and measure the ROS of a prescribed grass fire using a novel Intensity Variance Thresholding (IVT) method (chapter 4).

2.2.2 KHawk Thermal Sensing System

The FLIR Vue Pro R thermal camera (shown in Fig. 3.2) is used for KHawk UAS thermal image acquisition. This camera was selected because it is a radiometric camera capable of temperature measurements and has autopilot geo-tagging capabilities. This camera comes with cables that can be connected to the Pixhawk autopilot for autopilot geo-tagging. The connection diagram is shown in Fig. 3.2. This camera can also be operated in the low-gain (-40/+1022°F) and high-gain (-13/+275°F) modes and can produce images in 8-bit JPEG, 8-bit radiometric JPEG, and 14-bit TIFF. Generally, radiometric JPEG format is required for temperature measurements and TIFF images are preferred for orthomosaic generation [2].

One of the main roles for thermal cameras in disaster mapping is the detection and monitoring of wildland fires. Given their ability to capture temperature differences, thermal images can be easily used to accurately detect fire fronts. This is further shown in chapter 3, where FLIR thermal cameras are used to map a prescribed grass fire.

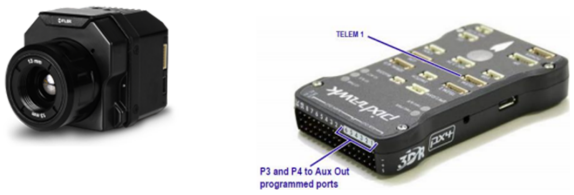

P1 - Accessory Port (DF13-7S-1.25C)		Wire color	P2 - MAVLink (DF13-6S-1.25C)		P3 - AUX Out (M20-1060300)		P4 - AUX Out (M20-1060300)	
PWM_1	1	green	RX in	3				
PWM_2	2	white	TX out	2				
GND	3	black	GND	6				
PWM_3	4	orange	→		PWM_3	1		
GND	5	black	→		GND	3		
PWM_4	6	blue	→		→		PWM_4	1
GND	7	black	→		→		GND	3

Figure 2.3: FLIR Vue Pro R thermal camera and Pixhawk autopilot connection diagram [2].

2.3 UAS Path Planning

Autonomous GPS waypoint tracking is mostly preferred for UAS remote sensing missions due to image quality requirements. This can be achieved by generating desired waypoints on the UAS ground control station (GCS) software such as Mission Planner for Pixhawk powered UAS. For general UAS remote sensing applications, the waypoints are usually generated such that the UAS path satisfies structure from motion (SFM) requirements of longitudinal and lateral image overlapping for best image georeferencing and stitching purposes. However, these requirements may not be sufficient for disaster mapping missions. The mission type will also greatly affect the UAS path planning, depending on whether the UAS is deployed for in-situ (generally fast-evolving) mapping or post-disaster damage assessment. The following subsections gives an overview of these considerations.

2.3.1 UAS Path Planning for Fast-Evolving Processes

The UAS flight path is very critical for successful mapping of fast evolving environmental processes such as wildland fires, chemical leaks, or floods. The main difference between such missions and general remote sensing missions such as precision agriculture or structural monitoring is that they rapidly change spatiotemporally during the UAS flight. This is discussed in detail in

chapters 3 and 4, where the KHawk UAS thermal and NIR images are used to map and measure a prescribed grass fire in Kansas. The KHawk UAS was deployed over the prescribed grass fire to observe, map, and measure the fire front location and fire ROS in different parts of the burning field. Acquired thermal and NIR images from this mission are required to produce short time-series orthomosaics that can accurately depict the state of the fire spread at specific time intervals during the fire. A simple concept is shown in in Fig. 2.4 as an example to demonstrate the UAS path planning strategies for this mission.

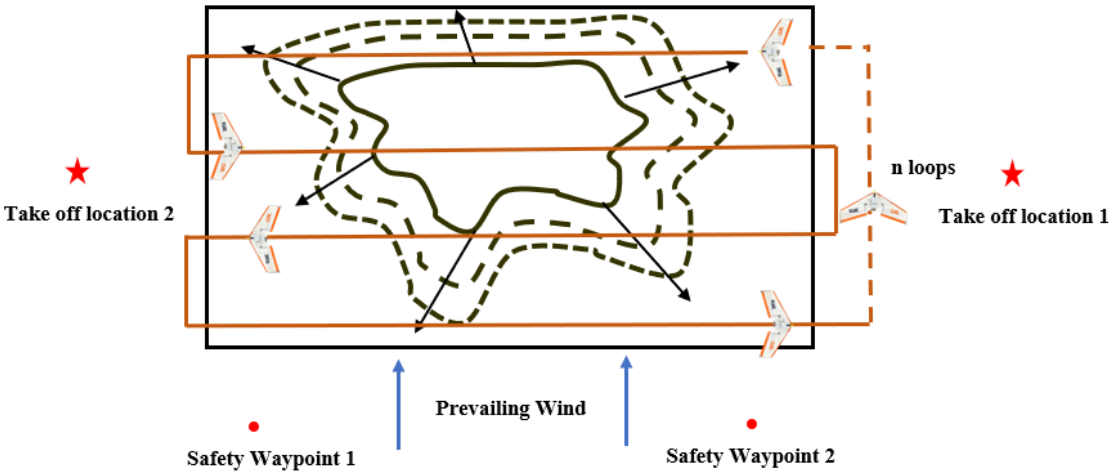

Figure 2.4: UAS mission for wildland fire mapping.

Similar to general UAS remote sensing missions, the UAS flight altitude and initial flight path will need to be determined first based on airspace regulations, UAS operating conditions (range, endurance, desirable wind speeds), and camera specifications (FOV and update rate). In addition, fire monitoring applications demand other considerations such as take-off location, UAS cruise heading, and additional safety waypoints in case of emergencies. An example implementation can be found in Fig. 2.4. The UAS is required to take-off and land against the wind and cruise cross-wind. If the UAS cruises into or against the wind, it may have different ground speeds over different parts of the field which can create complications in the fire mapping and measurements.

2.3.2 UAS Path Planning for Post-Disaster Damage Assessment

UAS path planning for post-disaster damage assessment can be similar to other general UAS-based remote sensing missions, which usually requires sufficient overlapping and stable image acquisition. Typical examples of post-disaster damage assessment include, crop damage assessment and damage swath measurements such as survey of swath length and width caused by tornadoes or hail. The special considerations for such missions include the location and time selection for optimal data acquisition, given the large spatial-scale of a damage site and limited UAS coverage within a given time frame. For instance, a hail storm can generate a damage scar covering tens or hundreds of miles. Which areas of the damage scar should be surveyed and after how many days are primary questions that need to be addressed for UAS hail damage assessment missions. Ideally, the UAS should be deployed over selected areas with varying damage levels within the scar for comprehensive analysis before the field is recovered by landowners or emergency response teams. Also, the UAS can be deployed at the same time satellite or manned aircraft flyby to create opportunities for comprehensive multiscale and multitemporal damage analysis.

2.4 KHawk UAS Disaster Multispectral Data Sets

The developed KHawk fixed-wing UAS with suitable multispectral cameras was deployed for several environmental and disaster mapping missions. This section presents representative disasters and associated multispectral data collected by the UAS.

2.4.1 UAS Prescribed Grass Fire Data Sets: April 8, and Oct. 8, 2019

The KHawk fixed-wing UAS was deployed for grass fire monitoring over two prescribed burns in Kansas (Table 2.2). The objective of these missions is to map the evolution of the grass fire and measure the fire location, spread direction, and fire ROS. The UAS was programmed to autonomously fly multiple loops over the burn site for repeat-pass multispectral image acquisition. One flight loop from the KHawk UAS flight path is shown in Fig. 2.5. Representative multispectral

images (RGB, NIR, and thermal) of the two grass fires are shown in Fig. 2.6.

Table 2.2: KHawk UAS Grass Fire Data Sets.

Location	Date	Wind Speed ms^{-1}	Burn Site Area sq. m	Sensing Payload
Baldwin Woods Forest Preserve, KS	April 8, 2019	3.1	430×70	RGB & NIR
Anderson County Prairie Preserve, KS	October 8, 2019	6.26	530×250	Thermal & NIR

Figure 2.5: Partial KHawk UAS flight path over Baldwin Woods Forest Preserve fire.

Among these two grass fire data sets, the Anderson County fire was more comprehensively observed due to the use of both thermal and NIR cameras and supporting ground wind measurements. The grass fire mapping and measurement methods developed and presented in this dissertation are demonstrated using this data set in Chapters 3 and 4.

2.4.2 UAS Tornado Damage Assessment Data Set: July 12, 2017

The developed KHawk UAS was also deployed for autonomous multispectral data acquisition over a tornado-affected field in Farragut, Iowa on July 12, 2017. The pre-planned UAS flight path is

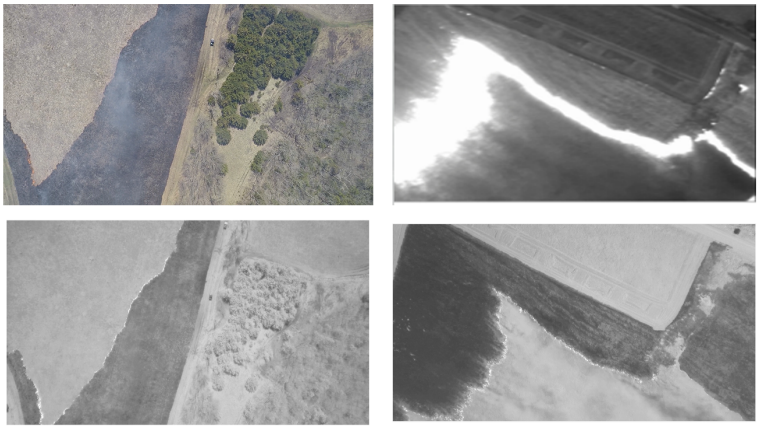

Figure 2.6: Example multispectral images of prescribed grass fires at the Baldwin Woods Forest Preserve (RGB and NIR) (left) and Anderson County Prairie Preserve (thermal and NIR) (right) fields.

shown in Fig. 2.7, illustrated over an orthomosaic, generated using the Agisoft Photoscan Pro software. The purpose of this flight was to analyze the damage caused by an EF2 tornado which touched down on June 28, 2017.

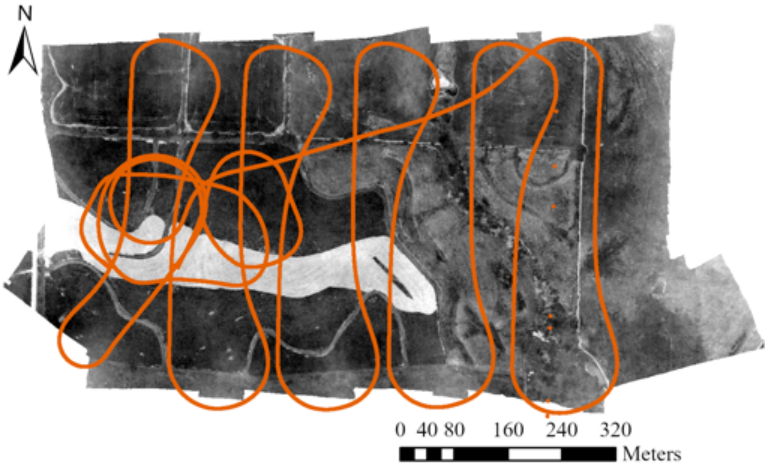

Figure 2.7: KHawk UAS flight path for Iowa tornado damage assessment.

The KHawk UAS was equipped with PeauPro82 GoPro Hero RGB and NIR cameras operating at 29.97 Hz video mode with image resolution of 1920 $\times$ 1080 pix. The collected RGB and NIR images were manually geo-tagged and orthorectified using Agisoft Photoscan Pro software.

Fig. 2.8 and Fig. 2.9 shows the RGB, red (top), NIR (middle), and the derived NDVI (bottom) orthomosaics of the damage field. The NDVI is calculated using the calibrated NIR and red

Figure 2.8: RGB orthomosaic of tornado damage area.

reflectance values. In this data set, the digital number (DN) images are calibrated to reflectance using low-cost target boards.

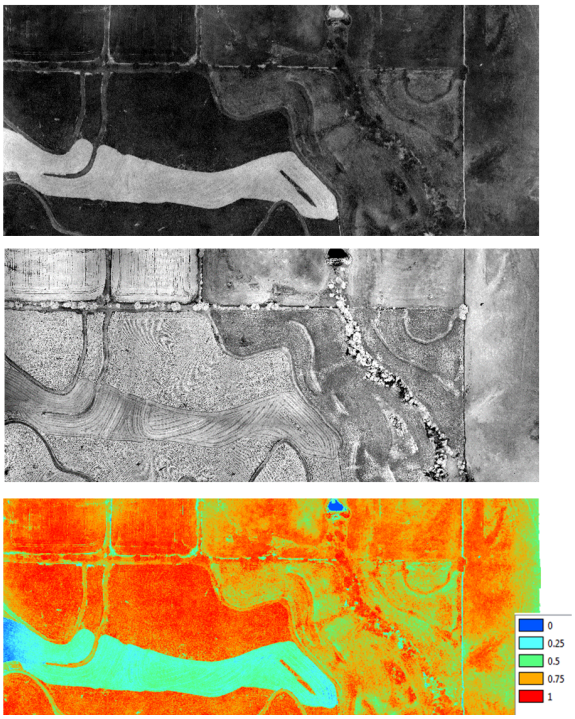

Figure 2.9: Red (top), NIR (middle), and NDVI (bottom) orthomosaics of tornado damage area.

The observed damage track from these multispectral orthomosaics may not be an accurate representation of the tornado damage as the field was mowed by farmers before the KHawk UAS mission.

2.4.3 UAS Hail Damage Assessment Data Set: July 23, 2017

The KHawk UAS was deployed for the multispectral data acquisition and post-disaster damage assessment of the June 22, 2017 hail damage in South Dakota. This hail storm generated a 60-mile swath of crop damage extending from Thomas, South Dakota to Marshall, Minnesota. Fig. 2.10 shows the damage track as observed by the Aqua and Landsat 8 (L8) satellites on July 2, 2017 and July 7, 2017 (top left) respectively. The main objective of the KHawk UAS mission was to acquire NIR and RGB imagery that can be used to map the crop damage caused by this hail storm and also generate damage maps for comparison with medium resolution Landsat 8 (L8) imagery. The KHawk UAS survey was conducted on July 23, 2017. Fig. 2.10 shows a ground picture of the damage site (bottom left) and a KHawk RGB map acquired on July 23, 2017 (bottom right).

Figure 2.10: South Dakota hail damage assessment: a) MODIS image from NASA Aqua satellite captured on July 2, 2017, b) Landsat 8 image captured on July 7, 2017, c) ground picture captured on July 23, 2017, and d) KHawk RGB map acquired on July 23, 2017.

Fig. 2.11 shows the NIR and red orthomosaics in DN. Horizontal stripes in these orthomosaics may be a result of insufficient lateral image overlapping. One of the main objectives of this mission was to analyze the differences between UAS and satellite damage observations, such as small-scale features. Fig. 2.12 shows a zoomed-in view of the northwest region of the damaged area using KHawk images (NIR in top left and RGB in top right) and L8 NIR image in the bottom. It can be observed that the UAS is able to identify a region (denoted by black dotted curve) that was

protected from the hail storm by a treeline that is vaguely observed by the satellite image. This observation showcases the main advantage of UAS imagery for disaster damage assessment.

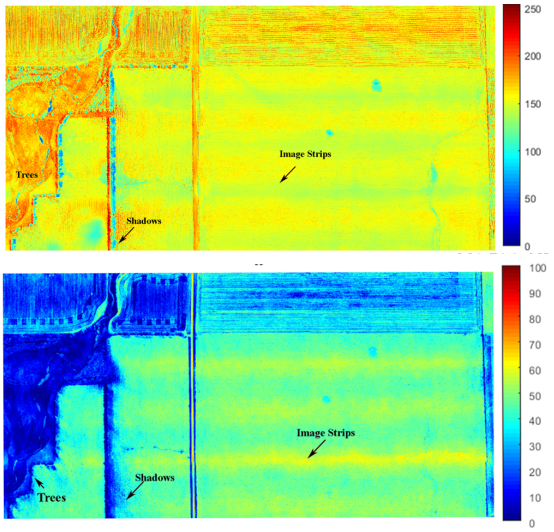

Figure 2.11: NIR (top) and Red (bottom) orthomosiacs of the South Dakota hail damage site.

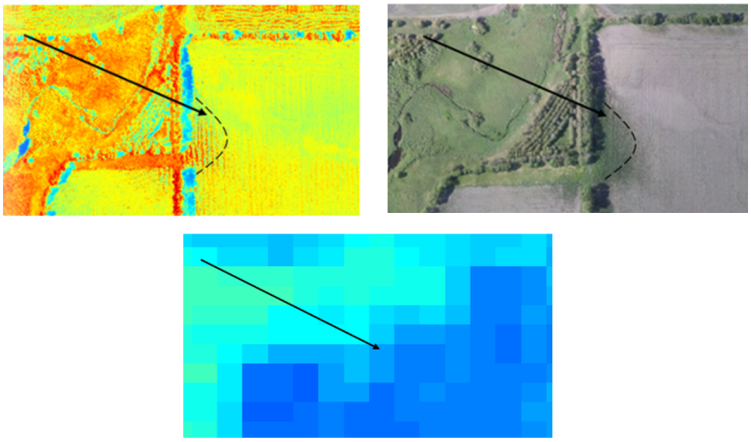

Figure 2.12: Zoomed-in view of the northwest tree range in the South Dakota hail damage site: KHawk NIR (top left), KHawk RGB (top right), L8 NIR (bottom) images.

One main takeaway from this data set is that accurate UAS surface reflectance estimates are needed for UAS disaster damage assessment. This problem is addressed in chapter 5 of this dissertation using a novel satellite-based cross calibration method for UAS reflectance estimation.

2.5 Chapter Conclusions

This chapter describes the important design and mission considerations for the KHawk UAS multispectral remote sensing system in disaster mapping applications. Example UAS disaster remote sensing missions and acquired data sets are also provided including KHawk UAS multispectral data acquired over Kansas prescribed grass fires, Iowa tornado damage site, and South Dakota hail storm damage areas, which lays the foundation for the following chapters in this dissertation.

Chapter 3

Prescribed Grass Fire Evolution Mapping and Rate of Spread Measurement Using Orthorectified Thermal Imagery from a Fixed-Wing UAS

3.1 Chapter Introduction

Accurate understanding of wildland fire behavior in different environmental and fuel contexts is critical to prescribed fire planning and operation as well as wildfire prevention and mitigation. The fire front location and rate of spread (ROS) are two important fire behavior metrics that are very useful to fire ecology researchers [4] interested in understanding the impact of fuel and vegetation on fire evolution, fire modeling researchers [5] who may focus on developing accurate fire spread models, and operational fire forecasting researchers [6] interested in building accurate predictive fire models. Many of these above applications often use fire ROS measurements for fire spread modeling and evaluation and therefore, value the accuracy and scale of these measurements over the processing time.

Most remote sensing-based fire location and ROS measurements are performed by the post-processing of satellite or airborne images acquired during the fire activity. Historically, satellites have been a major source of data for fire mapping, including the detection of active fires and hot spots [7–9], fire spread modelling [10], and fire damage assessment [11]. However, due to coarse spatial resolutions (250 - 1000 m) and slow revisit times (twice a day or more), satellite data may not be effective in measuring fire ROS at fine spatial and temporal scales, especially for prescribed fires that are usually completed within hours or wildfires that are contained within a

day. Additionally, it is suggested that spatial and temporal resolutions of 10 m and 10 min are desired for reliable data-enabled operational wildfire spread modelling and forecasting [6]. This has encouraged the use of other remote sensing sources such as manned aircraft for fire ROS measurements.

Repeat-pass thermal infrared imagery collected by Pacific Southwest Research Station (PSW) FireMapper fire imaging system aboard a manned aircraft were processed post-fire for the measurement and analysis of wildfire ROS in the San Dimas forest in 2002 at a spatial scale of $10^1 - 10^3$ m, which was validated using ground-observations of similar fields from previous literature [12]. A series of image processing tools were developed for the automatic extraction of fire line parameters including, fire line location and fire front direction using airborne multispectral images and post processed NDVI [13]. Similarly, airborne imagery from the King Air B200t research aircraft was used for remote measurements of fire intensity, fire line geometry, heat and carbon fluxes during large wildland fires in Brazil [14]. Airborne images from the Forestry Services of Castilla-La Mancha were orthorectified post-fire to form fire isochrones which were then used to calculate the fire location and fire ROS for forest fires [15, 16]. In summary, manned aircraft have been successfully used for real-time fire mapping and post-fire ROS measurements since they can collect images with high spatial and temporal resolutions (sub-meter level every few hours). However, they are limited by cost of operation, pilot safety, and limited flexibility in flight path modifications, which has motivated the use of Unmanned Aircraft Systems (UAS) for these applications.

UAS with low-cost multispectral or hyperspectral cameras are generally easier to handle and can fly autonomously over fires without putting human pilots at risk, making them an ideal platform for fire-related applications. However, since they generally fly at low altitudes ($\leq$120 m above ground level in USA due to FAA regulations), fire generated turbulence and smoke can have an impact on their safety and data quality if not well planned [17]. Although UAS has been used for many wildland fire applications, including vegetation impact mapping [18–21], fire ignition [22], and fire detection [23, 24], its use in fire ROS measurements is still limited in existing literature. The few UAS-based fire ROS measurements to date have been restricted to small spatial scales

(less than 1 ha.) and use hovering multi-rotor UAS likely due to safety concerns for operation in dangerous fire environments. For example, multispectral images from a multi-rotor UAS were used for the estimation of complex fire progression, ROS, and spread direction in prescribed fires, where the UAS was positioned at a fixed-location while capturing a fire in a spatial scale of 0.01 - 1 ha [25]. The use of autonomous fixed-wing UAS for mapping and measurement of fire ROS is lacking, which we aim to address in this chapter.

This chapter introduces a novel method for fire evolution mapping and fire ROS measurement using a small fixed-wing UAS operating at a low altitude above the burning field. The proposed method is demonstrated using a data set collected by a KHawk fixed-wing UAS while observing a prescribed burn of a tallgrass prairie in Welda, Kansas. The main contributions of this chapter include:

1. A new and effective method for accurate recapturing of grass fire behavior (especially grass fires) using multitemporal thermal orthomosaics generated by UAS images acquired at low-altitudes .

2. A UAS prescribed fire thermal data set over a tallgrass field in Kansas, which includes individual georeferenced thermal images and orthorectified thermal maps (https://cusl.ku.edu/Flight_Log).

3. Comprehensive measurement, analysis, and validation of fire ROS in a typical tallgrass prairie, which has not been sufficiently addressed in existing remote sensing literature.

4. Discussions, lessons, and recommendations for safe and efficient operation of small fixed-wing UAS for fire observation.

Through our work, we aim to provide accurate thermal maps and ROS measurements of a tallgrass fire that can be directly used by fire modelling researchers [5, 26] who are interested in understanding grass fires, fire and tallgrass ecologists, land managers, and the prescribed grass fire community. Other UAS and remote sensing researchers can use our methods, lessons learned, and shared data as a resource to develop their systems and to set up future collaborations.

3.2 Prescribed Fire and Data

This section provides detailed descriptions of the prescribed fire event, including the aerial data collected by a fixed-wing UAS, and wind data collected by a ground weather station during the burn.

3.2.1 Prescribed Fire Experiment

A prescribed grass fire was conducted on October 8, 2019, between 11:38 AM and 12:25 PM (Central Daylight Time (CDT)) at the Anderson County Prairie Preserve, Kansas ($38.183347^{\circ}, -95.279201^{\circ}$), shown in Fig. 4.1. This site is a rectangular grassland field approximately 530 m $\times$ 250 m, relatively flat (1-3 % slope), spanning three soil types (SSURGO Soils: Clareson complex, Wagstaff silty clay loam, Kenoma silt loam) with fine fuel vegetation cover dominated by C4 tallgrasses and a mixture of herbaceous forbs and legumes (shown in Fig. 3.2). The mean wind during the burn was around 6.26 ms^{-1} from the south based on the ground weather station measurement at $\sim$ 1.9 m above the ground. The ambient temperature was around 73° F while the relative humidity was around 41 %. A small (approx. 0.1 inch) rain event was recorded in the area on October 5, 2019 [27]. This prescribed burn was performed by the Kansas Biological Survey (KBS) for grassland ecosystem management using a ring pattern ignition with two teams starting around the midpoint of the northern boundary (due to south wind). Each team then moved in opposite directions along the boundaries before meeting around the midpoint of the southern boundary. The fire propagated towards the center of the field from all the boundaries.

3.2.2 KHawk UAS Data

Thermal remote sensing data was collected by a KHawk 55 thermal fixed-wing UAS during the Anderson County fire. The KHawk 55 thermal UAS is a low-cost multispectral remote sensing platform developed by researchers at the CUSL at the University of Kansas, shown in Fig. 3.3. It is equipped with a Ublox M8P Here GPS and a Pixhawk Cube autopilot [28], which can support

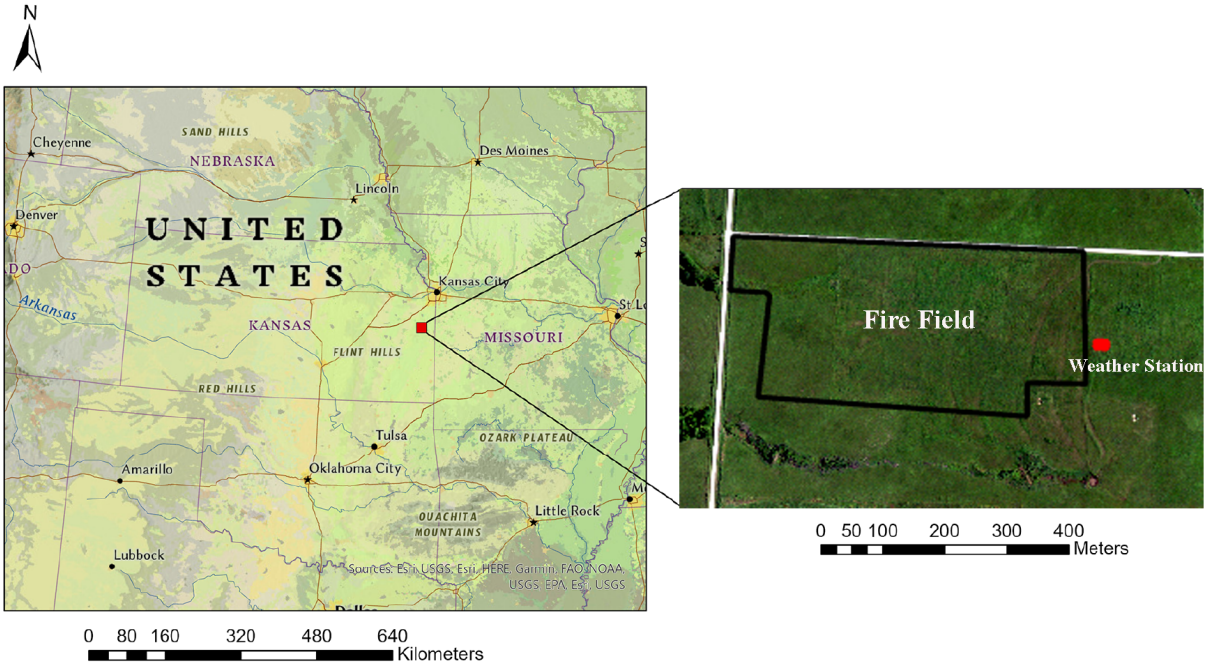

Figure 3.1: Anderson County Prairie Preserve: fire field (black perimeter) and weather station (red circle) labelled.

Figure 3.2: Anderson County Prairie Preserve ground picture.

both manual and autonomous flight. The detailed UAS specifications are provided in Table 3.1.

A FLIR Vue Pro R camera is used for thermal image acquisition and its specifications are listed in Table 3.2. These images were acquired in a 14-bit TIFF format and geotagged real-time through the MAVLink connection with the Pixhawk autopilot.

The KHawk thermal 55 UAS was deployed to follow a pre-planned flight path for fire monitoring, with minor adjustments made by the ground control station operator during the burning based on the observed fire evolution. The UAS was programmed to fly autonomously at around 120 m

Table 3.1: KHawk 55 Thermal UAS Specifications.

Description	Value
Take-off Weight	2.5 kg
Wingspan	1.4 m
Cruise Speed	20 ms^{-1}
Maximum Endurance	30 min
Typical Altitude	120 m
Spatial Resolution (at 120 m above the ground)	0.23 m

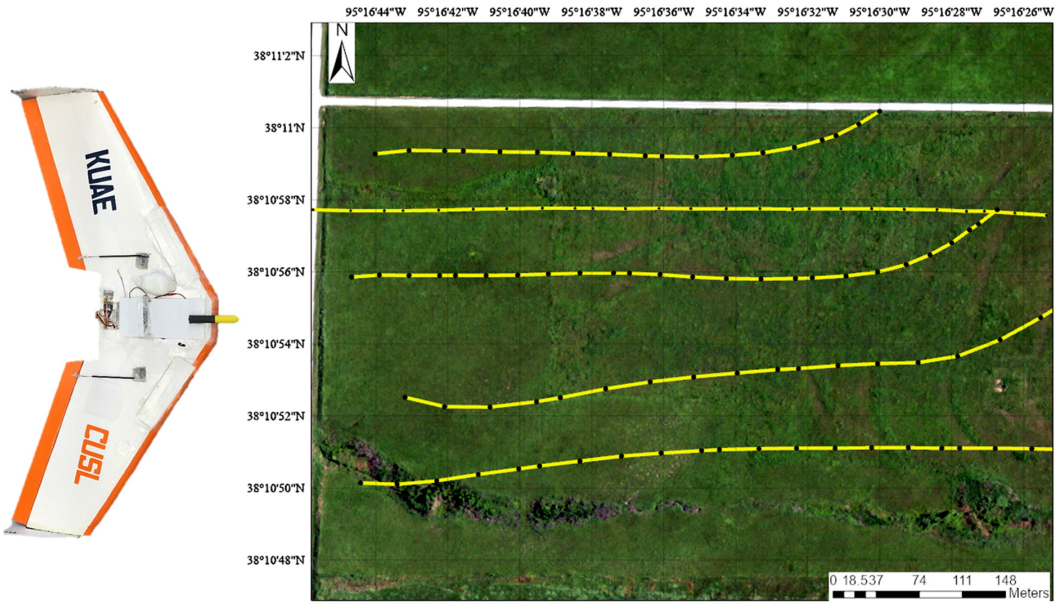

Figure 3.3: KHawk 55 thermal UAS (L) and its flight path during the fire (R).

Table 3.2: FLIR Vue Pro R Thermal Camera Specifications.

Description	Value
Spectral Bandwidth	7.5 to 13.5 μm
Sensor Resolution	640×512 pix
Field-of-View (FOV)	$69^\circ \times 56^\circ$
Frame Rate	1 Hz

above the ground to collect repeat-pass time-sequential images which can be used to generate multitemporal orthomosaics. A pair of repeat-pass thermal images with their respective time stamps

observing the same area are shown in Fig. 3.4 as an example, where the top images are acquired one second apart from one UAS flight loop and bottom images are from a different flight loop. The collected thermal images from 12:06:05 PM to 12:17:47 PM were processed and used in this chapter. The UAS flew multiple loops over the field at an approximate interval of about 2 min such that the set of images captured within each loop can be used to generate one orthomosaic. Only images from straight path with wings level flight are used for orthorectification. The majority of the UAS flight path is shown in Fig. 3.3 with effective image acquisition overlaid on a National Agriculture Imagery Program (NAIP) image (spatial resolution of 1 m). The NAIP image was used as a reference image for orthomosaic registration, which is further discussed in Sec. 4.1.

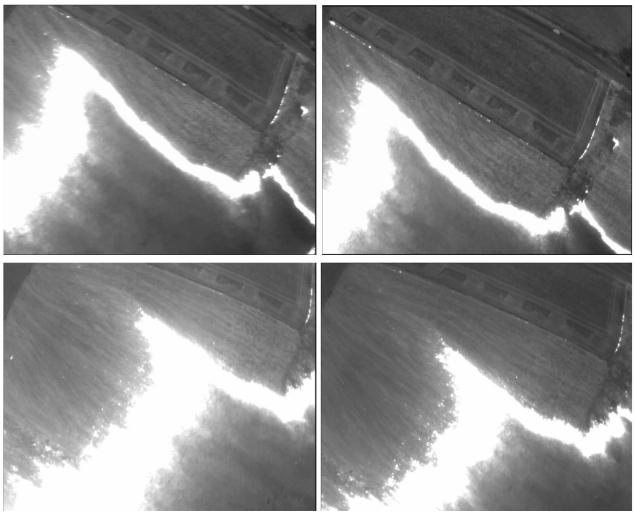

Figure 3.4: Example KHawk thermal repeat-pass image pairs along the west boundary: top and bottom images are from different UAS flight loops.

3.2.3 Ground Wind Measurement Data

A Campbell Scientific CSAT3B wind anemometer was placed about 20 m east of the eastern boundary (labelled in Fig. 4.1) at a height of $\sim$ 1.9 m from the ground to measure the 3D wind speed and temperature at an update rate of 100 Hz.

Note that although the fire ignition and burning lasted for about 43 minutes, only 10 min of

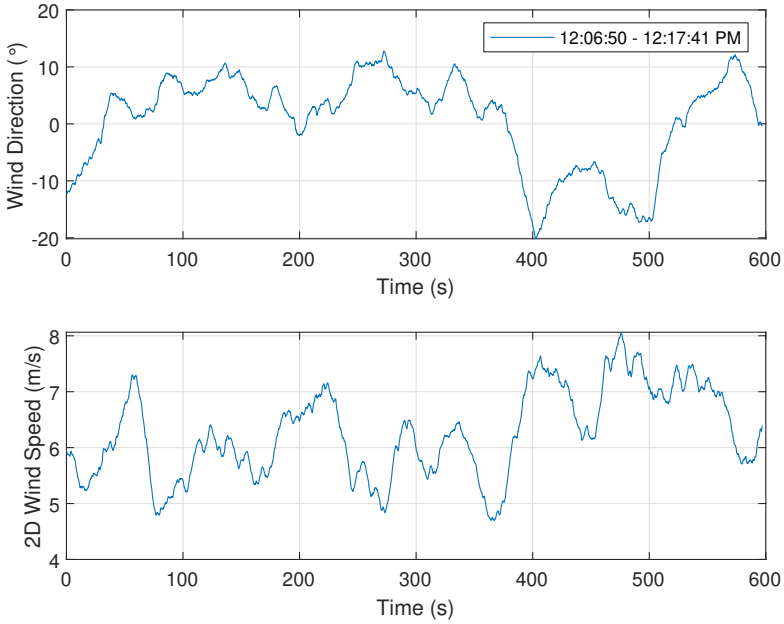

Figure 3.5: Wind direction and 2D horizontal wind speed between 12:06:50 PM and 12:17:47 PM from Campbell Scientific anemometer.

thermal and wind data from 12:06:50 PM to 12:17:47 PM were used for analysis in this chapter. This is due to UAS battery constraints, field planning limitation, and safety precautions for UAS operations in close vicinity of fires and fire generated smoke. Fig. 3.5 shows the measured wind direction and 2D horizontal wind speed (smoothed by a 20-sec moving average filter) during this time. The prevailing wind was from the south at an average speed of 6.26 ms^{-1} with an exception around 380 seconds (about 12:13:10 PM) when a brief change in direction towards south occurred as the fire front passed the weather station, and caused a temporary change in the local wind direction (see orthorectified images shown in Sec. 4).

3.3 Methods

A new method is introduced in this section for fixed-wing UAS-based fire evolution mapping and ROS measurement. The proposed method utilizes UAS acquired repeat-pass thermal images to generate multitemporal orthomosaics, which can be used to represent the dynamic evolution of a fire at regular time intervals. The derived fire evolution map can then be used for the ROS

calculation at different time stamps and locations. The main components of this method are shown in Fig. 3.6 including, 1) multitemporal orthomosaic generation, 2) fire evolution mapping, and 3) fire ROS calculation.

3.3.1 Generation of Multitemporal Orthomosaics

The first step of this method is to generate multitemporal orthomosaics using UAS collected repeat-pass thermal images. Each orthomosaic corresponds to a specific interval of time and is generated using multiple images belonging to a single UAS flight loop. Here, a flight loop is defined as the UAS path that can provide a complete coverage of the field once. These orthomosaics capture the fire evolution at different stages and can be combined to form a fire evolution map. This process can be formulated as below.

Given a UAS flying m loops over a fire field acquiring n geotagged images per loop, $I_b = \{i_{1b}, i_{2b}, ...i_{nb}\}$ *with corresponding timestamps,* $T_b = \{t_{1b}, t_{2b}, ...t_{nb}\}$*, where b refers to the loop index. A total of m orthomosaics,* $O_b = \{O_1, O_2....O_m\}$ *can be generated by georeferencing and stitching all the images corresponding to each loop as shown below.*

$$\begin{aligned} I_1 &= \{i_{11}, i_{21}, ...i_{n1}\} \rightarrow O_1 \\ I_2 &= \{i_{12}, i_{22}, ...i_{n2}\} \rightarrow O_2 \\ &\cdot \\ I_m &= \{i_{1m}, i_{2m}, ...i_{nm}\} \rightarrow O_m \end{aligned} \tag{3.1}$$

Each orthomosaic, O_b contains information from n images with n timestamps from t_{1b} to t_{nb}. Generation of such orthomosaics is illustrated in the top block of Fig. 3.6. Due to possible spatial uncertainties and misalignments, each orthomosaic is recommended to be registered with a high-accuracy reference image before they are used for any fire metric measurements.

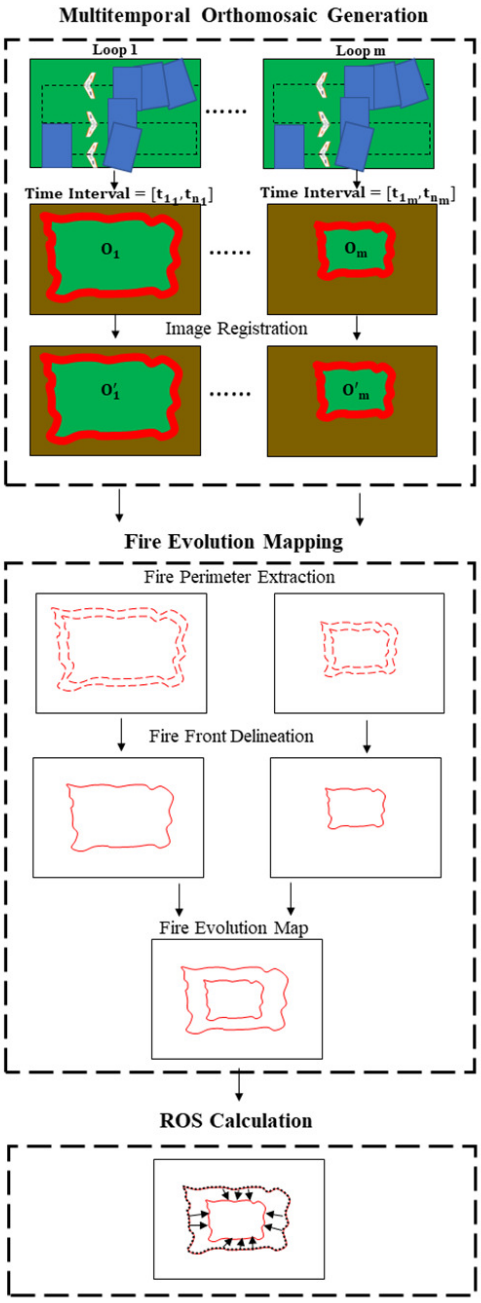

Figure 3.6: Flow diagram for fixed-wing UAS-based fire evolution mapping and ROS calculation.

3.3.2 Fire Evolution Mapping

Registered orthomosaics can be used to generate a fire evolution map that contains multiple fire fronts from each orthomosaic using two steps, 1) fire perimeter extraction and 2) fire front delineation. The fire perimeter, f' is defined as the entire outer edge of a fire [29], including the leading and trailing edges, where the leading edge represents the fire front. The fire perimeter can be extracted from a thermal orthomosaic using temperature or intensity-based thresholds as shown below.

$$f'_b = \begin{cases} 1, & \text{if } O'_b \geq \alpha \\ 0, & \text{otherwise,} \end{cases} \tag{3.2}$$

where α is a temperature or intensity-based threshold.

The extracted fire perimeter is usually in the form of discrete points, which is not desirable for further determination of fire ROS spread vector. The next step is to delineate fire fronts, f_b from each orthomosaic, where continuous curves are created from discrete pixels along the leading edge of the fire perimeter, f'_b. A manual delineation procedure can be used to connect these discrete pixels to result in continuous fire fronts [30]. The final delineated fire fronts corresponding to each orthomosaic can be added to form the fire evolution map, F, such that $F = f_1 + f_2 .... + f_m$. An illustration of the fire evolution mapping procedure for orthomosaics O_1 and O_m is shown in the middle block of Fig. 3.6.

3.3.3 Fire ROS Measurement

The final step of this method is the fire ROS calculation. The calculation of fire ROS between consecutive fire fronts, f_b and f_{b+1}, requires the distance and time-lapsed between them. First, p equally-spaced points are selected such that $f_b = \{A_1, A_2, ...A_p\}$, where A_p is the location of the pth point along f_b.

Next, the spread vectors, $\vec{AB}$ can be drawn along the direction perpendicular to the local curve from A_p until they intersect the consecutive fire front at B along f_{b+1}. Note that other approaches

for fire spread vector determination exist in the literature including drawing the vector along the visual and wind direction trends, however, no substantial differences were observed between these different approaches [30]. Finally, the time interval between the individual images ΔT can be calculated. The ROS can be calculated using the following equation.

$$ROS_A = \frac{\|\vec{AB}\|}{\Delta T} \tag{3.3}$$

The bottom part of Fig. 3.6 illustrates the ROS calculation between the two fire fronts corresponding to orthomosaics I_1 and I_m.

3.4 Results

The proposed method is implemented and validated using the Anderson County fire data set and corresponding results are presented in this section.

3.4.1 Generation of Multitemporal Orthomosaics

Repeat-pass thermal images collected by the KHawk thermal UAS from 12:06:50 PM to 12:17:47 PM are used to generate four multitemporal orthomosaics (O_1,O_2,O_3,O_4), as shown in Fig. 3.7. The Agisoft Photoscan Pro software was used for the orthorectification process. It is known that orthorectifying thermal images can be challenging due to low image resolution and contrast in the thermal band [31]. To overcome this challenge, the FLIR Vue Pro R camera was set at the 14-bit tiff mode such that the resulting images had the least compression and highest radiometric resolution. Additionally, since these thermal images contained fire pixels, there was a sufficient contrast for feature matching. Therefore, the overall process for the thermal orthomosaic generation in the Agisoft Photoscan software was similar to that of RGB images. Each orthomosaic covers the same area at spatial scales of order 10^4 m^2 with a temporal resolution about two minutes. Important properties including number of images used and time-interval for each orthomosaic are listed in Table 3.3. Note that not all the images within the start and end flight loop times were used for

stitching and some images were manually excluded due to blurriness or when the UAS was not flying straight and wings-level. O_2 (top right) has some stitching errors due to a few improperly aligned images in areas where the fire is not present, caused mainly by slow and inaccurate UAS flight path adjustments during the burn.

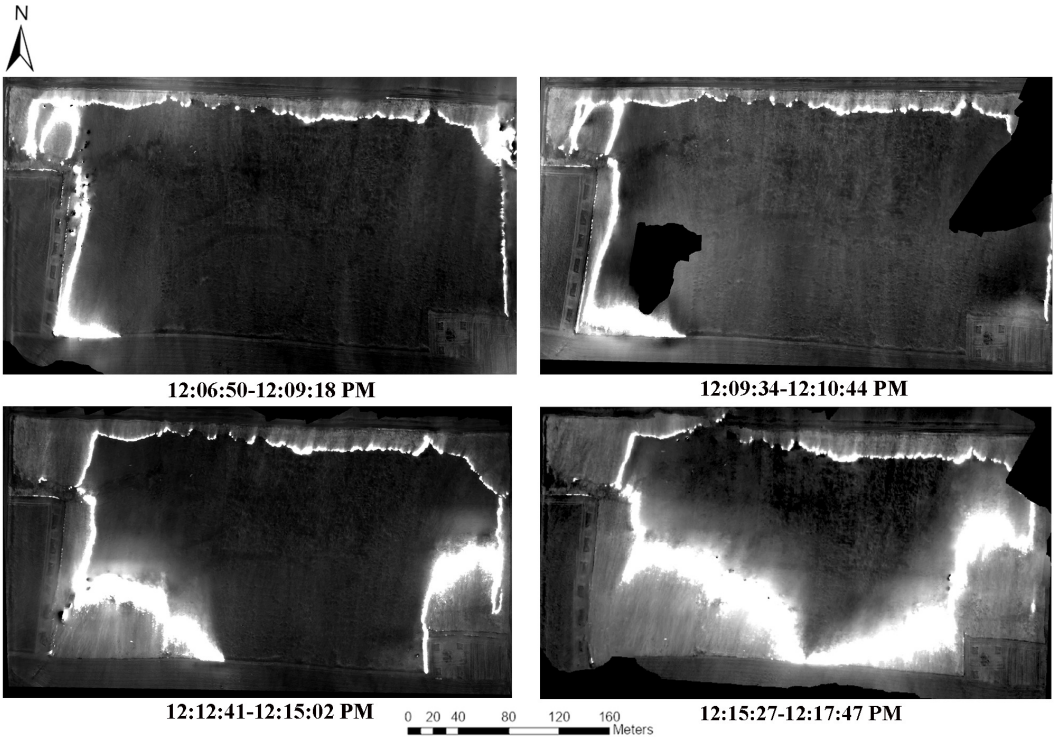

Figure 3.7: Multitemporal thermal orthomosaics: O_1 (top left), O_2 (top right), O_3 (bottom left), and O_4 (bottom right).

Table 3.3: Multitemporal Thermal Orthomosaic Properties.

Orthomosaic	Number of Images	Start-End Time (CDT)
O_1	119	$12:06:50 - 12:09:18$ PM
O_2	103	$12:09:34 - 12:10:44$ PM
O_3	96	$12:12:41 - 12:15:02$ PM
O_4	85	$12:15:27 - 12:17:47$ PM

The generated orthomosaics are co-registered with a NAIP image with a spatial resolution of 1 m using the ArcGIS Georeferencing tool. The NAIP image was acquired on June 30, 2019 and

has a horizontal position accuracy of about 6 m at a confidence level of 95% [32]. Multiple control point pairs are manually selected from each KHawk orthomosaic and the NAIP image such that they are spread out across the whole field. Table 3.4 shows the registration attributes for each orthomosaic where the registration errors for all the orthomosaics are at similar levels (about 1.5 m root mean squared error (RMSE)). Another observation is that only 5 and 7 control point pairs are used for O_2 and O_4 as compared to 10 pairs for the other two. This is because the images from the UAS flight loop used for O_2 were not very stable due to turbulence experienced by the UAS and caused some stitching errors. The fire and its surrounding regions (smoke, hot regions, etc.) occupy a large portion of the field in O_4 preventing the visibility of many feature points (can be seen in the top and bottom right of Fig. 3.7).

Table 3.4: Image-to-Image Registration Attributes for Multitemporal Thermal Orthomosaics Using 1 m NAIP Imagery.

Orthomosaic	Spatial Resolution (m)	Control Point Pairs	Transformation Type	RMSE (m)
O_1	0.23	10	Affine	1.32
O_2	0.23	5	Affine	1.59
O_3	0.23	10	Affine	1.49
O_4	0.23	7	Affine	1.52

3.4.2 Fire Evolution Mapping

The fire perimeter is extracted from all the orthomosaics using the standard deviation data classification method in ArcGIS Pro. With class breaks set at one-third of the standard deviation of each orthomosaic, the range of values corresponding to the fire perimeter is determined through visual inspection. It is found that in all the orthomosaics, the fire perimeter pixel values are around 90% of the maximum intensity pixel value in the orthomosaic. Fig. 3.8 shows the fire perimeter extracted from each orthomosaic.

The fire front isolated from each orthomosaic corresponds to the time interval associated with that orthomosaic (Table 3.3). The delineated fire fronts are combined into one image, called the fire evolution map, shown in Fig. 3.9. Here, fire fronts from each orthomosaic are shown in

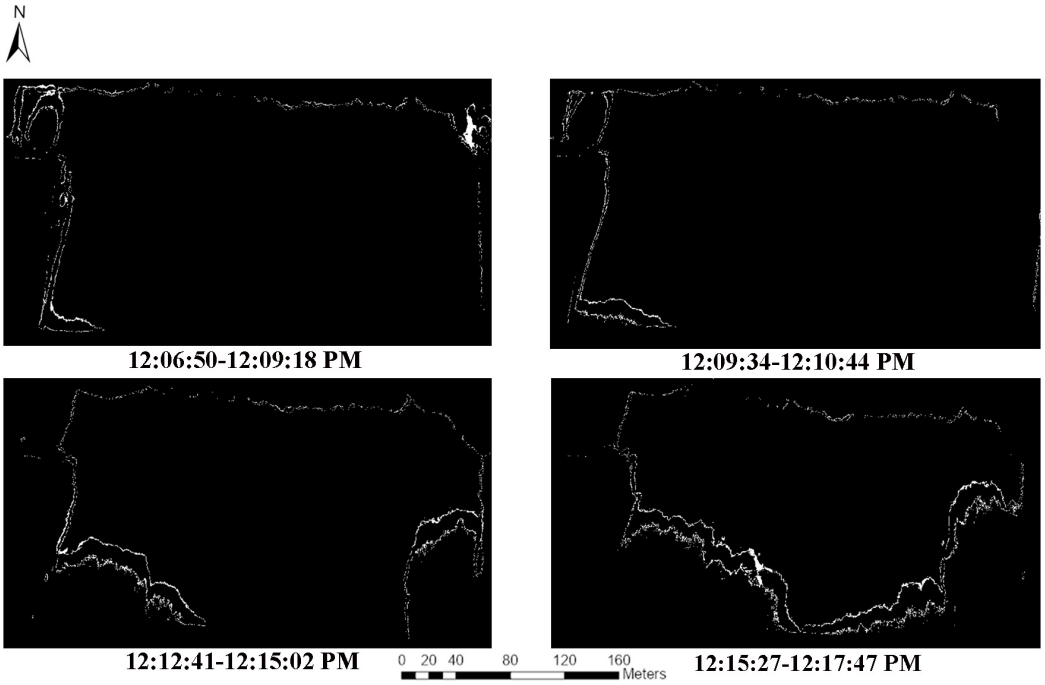

Figure 3.8: Extracted fire perimeter from multitemporal thermal orthomosaics: f_1' (top left), f_2' (top right), f_3' (bottom left), and f_4' (bottom right).

different colors and their corresponding time-intervals are labelled. It is worth mentioning that the time-intervals of these fire fronts are subsets of time-intervals associated with their corresponding orthomosaics. The arrows in this figure represent spread vectors, which are discussed in more detail in the next subsection. The evolution of fire fronts from the northern boundary is not focused in this analysis since they evolve very slowly during due to the strong prevailing south wind.

3.4.3 Fire ROS Measurement

Equally-spaced sample points (every 10 m) are selected along each delineated fire front to calculate the fire ROS. Then spread vectors are drawn from them in the direction of the local normal to the curve, f_b and are extended until they intersect the consecutive fire front, f_{b+1}. These vectors depict the direction of fire spread from each point. The distance between the starting and ending points of the spread vector can then be calculated and used in the fire ROS calculation for a given point

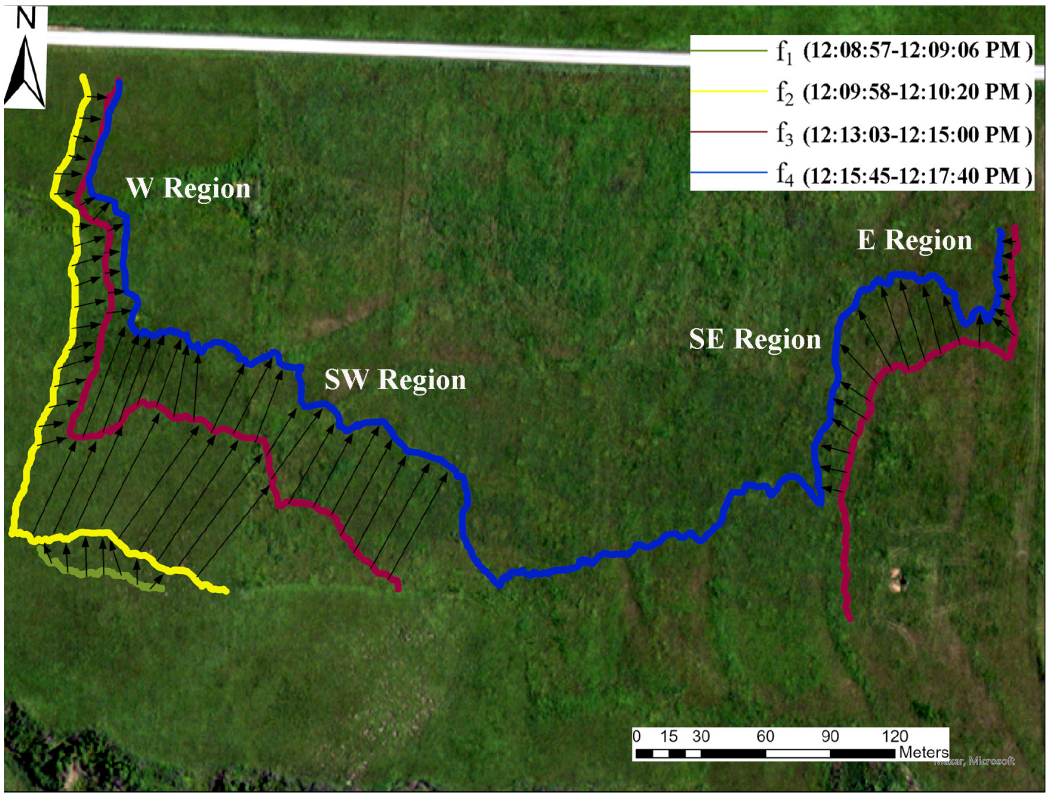

Figure 3.9: Fire evolution map.

in f_b. Note that the vectors may need to be manually adjusted for cases where two or more vectors intersect or collide. This could occur as a direct consequence of the manual delineation when spread vectors from f_b are drawn in opposite directions or point to the same location in f_{b+1}. The ROS for each point is calculated by dividing the distance by the elapsed time between them. The elapsed time is calculated by subtracting the timestamps corresponding to individual images respectively.

The obtained fire ROS measurements are analyzed statistically in different regions based on the location and the fire spread direction. These regions include West (fire spread towards the east), South West (fire spread towards the north/north east), South East (fire spread towards the north/north west), and East (fire spread towards the west). These spread directions are mostly influenced by the prevailing wind direction (from south to north from Fig. 3.5) and the fire ignition

sequence (ring-fire pattern starting from the northern boundary), since the study area is relatively flat with a uniform fuel load. The fire fronts from each map intersect the southern boundary at different locations, indicating that the fire setting is still in progress (Fig. 3.9).

The fire ROS measurements in the divided subgroups are visualized in polar plots, shown in Fig. 3.10. The statistics are further shown in Table 3.6-3.8, where the ROS in the South West and South East boundaries have a mean value of 0.26 ms^{-1} and 0.28 ms^{-1} respectively. These values are substantially higher than the West and East boundaries whose mean ROS values are observed to be 0.06 ms^{-1} and 0.11 ms^{-1}. The maximum ROS is found to be 0.4 ms^{-1} in the South West region. Given the wind direction (mostly south to north) and these observed trends, the fire front from the southern boundary can be treated as the head fire while the fire fronts from the east and west can be treated as the flank fire. Based on the analysis shown in this section, the mean head fire ROS is found to be 0.27 ms^{-1} which falls within the ROS range observed in similar tallgrass prairies in north central Oklahoma [4].

Table 3.5: ROS Statistics in the West Region.

Average Lapsed Time	ROS Statistics (ms^{-1})			
	Min	Mean	Max	Std
f_2-f_3 (178.3 s)	0.05	0.08	0.1	0.01
f_3-f_4 (163 s)	0	0.03	0.07	0.02
Cumulative				
	0	0.06	0.1	0.03

3.4.4 Uncertainty Analysis of Fire ROS

The objective of this subsection is to estimate the accuracy of the fire ROS calculated in Sec. 4.3. The ROS measurement accuracy mainly depends on the spatial and temporal uncertainties in the multitemporal orthomosaics, as shown in (3). These factors are discussed below.

1. Time uncertainty of the images: Each multitemporal orthomosaic is generated using n im-

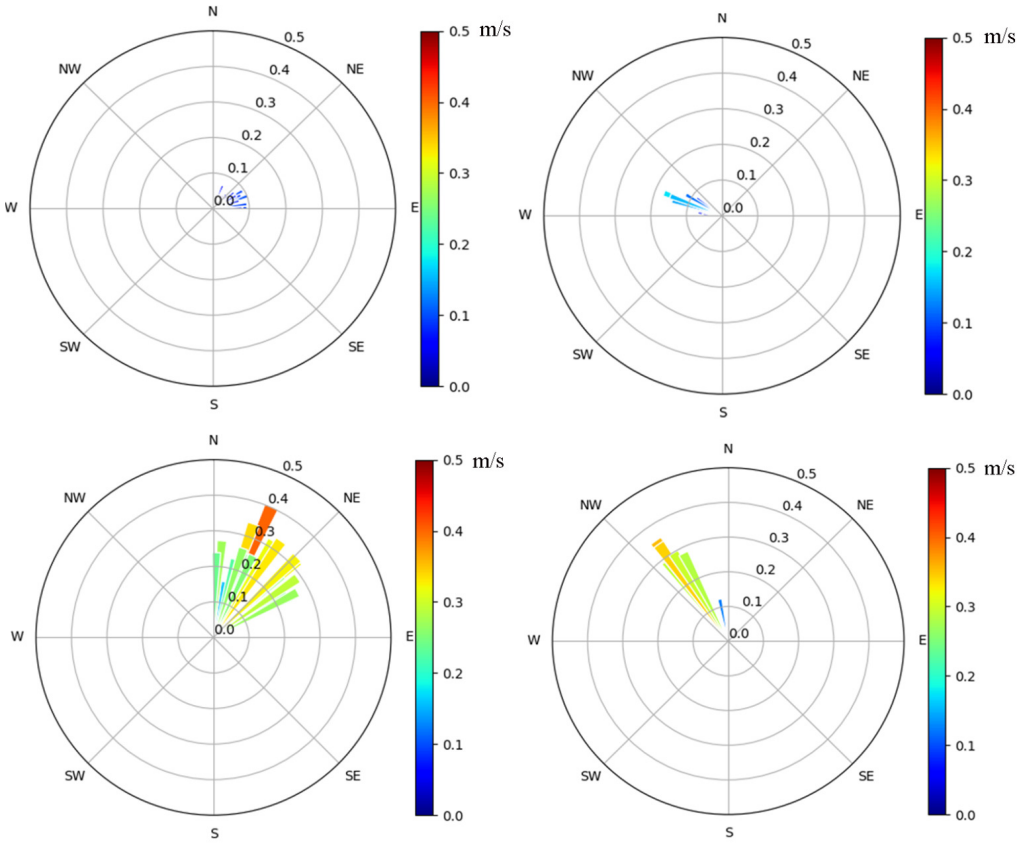

Figure 3.10: ROS in W (top left), E (top right), SW (bottom left), and SE (bottom right) regions.

Table 3.6: ROS Statistics in the South West Region.

Average Lapsed Time	ROS Statistics (ms^{-1})			)
	Min	Mean	Max	Std
f_1-f_2 (80.8 s)	0.18	0.25	0.32	0.05
f_2-f_3 (269.4 s)	0.16	0.22	0.26	0.04
f_3-f_4 (140.8 s)	0.23	0.28	0.4	0.04
Cumulative				
	0.16	0.26	0.4	0.06

ages, each having its own timestamp. The main source of uncertainty comes from the selection of specific individual images corresponding to the starting and ending of the fire spread

Table 3.7: ROS Statistics in the South East Region.

Average Lapsed Time	ROS Statistics (ms^{-1})			
	Min	Mean	Max	Std
f_3-f_4 (118 s)	0.12	0.28	0.35	0.07

Table 3.8: ROS Statistics in the East Region.

Average Lapsed Time	ROS Statistics (ms^{-1})			
	Min	Mean	Max	Std
f_3-f_4 (178 s)	0.04	0.11	0.17	0.05

vector between consecutive fire fronts. In this chapter, a time accuracy of ± 1 second was observed for the fire ROS calculation since the FLIR camera was set to sample at 1 Hz. This has a trivial impact on the final ROS calculation because the time difference between any two fire fronts were around or more than 120 seconds.

2. Spatial uncertainty of the multitemporal orthomosaics: The ROS is directly influenced by the spatial uncertainties of the multitemporal orthomosaics. For example, given a horizontal position error of δX for each of the consecutive orthomosaics, the ROS during a time interval ΔT can vary as much as $\frac{2\delta x}{\Delta T}$. Given the δX of about 1.5 m (Table 3.4) for these thermal orthomosaics and an assumed ΔT of about 120 seconds between consecutive fire fronts, the ROS uncertainty can be calculated as $\pm 0.025 ms^{-1}$, which is about 9 % of the mean head fire ROS.

In addition to the above uncertainty analysis, a further validation is conducted using a different fire observation video from a DJI Phantom. This DJI Phantom quadrotor equipped with an RGB camera was launched at 12:20:28 PM (approximately 168 seconds after the last KHawk fixed-wing view of the fire for continuous aerial observation) and manually operated over the north east boundary of the fire field. The fire evolution observed by the DJI at 12:22:03 PM and 12:23:42 PM is shown in Fig. 3.11. It can be observed from this figure that fire spread predominantly from the south to the north before consuming the entire field. This confirms that the head fire in f_4 travelled

a south to north trajectory shown in blue in Fig. 3.9.

Figure 3.11: Fire observations from DJI Phantom RGB video with time stamps in central time.

For the quantitative validation, a fire front, f_{DJI} is extracted from a manually registered DJI image at 12:22:03 PM (left frame in Fig. 3.11 before registration) and is used to validate the ROS of the head fire calculated in Sec. 4.3. The extracted fire front after registration is shown as the red curve in Fig. 3.12, which shows the head fire evolution from f_4 and DJI fire front f_{DJI} overlaid on the NAIP image. The objective of this analysis is to compare the calculated mean head fire ROS of 0.27 ms^{-1} and the ROS derived between the f_4 head fire at 12:17:32 PM and the f_{DJI} at 12:22:03 PM. It is worth mentioning that the DJI frame at 12:22:03 PM was selected due to the availability of landmarks in the image FOV.

This analysis supports that the head fire in f_4 would reach f_{DJI} at the expected time if it evolved at a ROS of 0.26 ms^{-1}, which is 0.01 ms^{-1} less than the calculated mean head fire ROS. This error falls within the calculated uncertainty window. Further anecdotal validation was given by the KBS prescribed fire crew, who confirm that the fire in the area between f_3 and f_{DJI} would be expected to evolve with a fairly constant ROS given the uniform fuel loads, wind and slope distributions at that location during the described burn event.

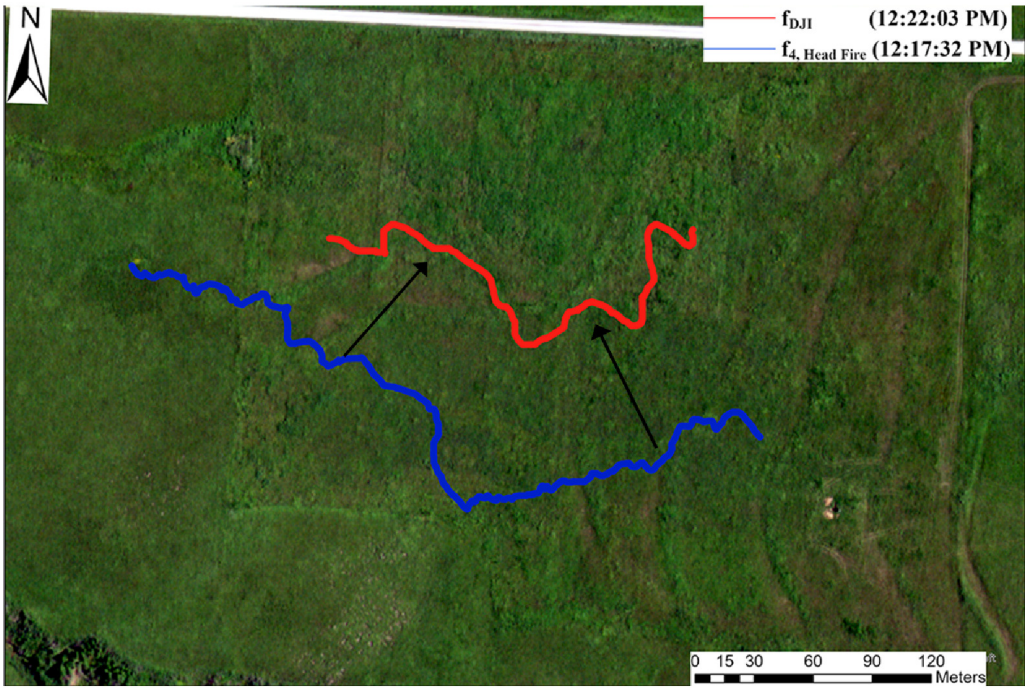

Figure 3.12: ROS validation: fire evolution between head fire from f_4 and f_{DJI} (from left frame in Fig. 3.11).

3.5 Discussions and Recommendations

The effectiveness of the proposed method is dependent on several factors from the UAS path planning to the final ROS calculation. Some of these critical factors are discussed in this section.

3.5.1 Fixed-Wing UAS Mission Design for Fire Observation

Fast evolving processes like fires pose special challenges for fixed-wing UAS based remote sensing because the environment constantly changes both spatially and temporally. To monitor such processes, the UAS has to fly multiple loops over the same field at regular time intervals for repeat-pass image acquisition, assuming that the FOV of the UAS camera cannot cover the whole field. During this prescribed fire experiment, the fixed-wing KHawk 55 thermal UAS was programmed to fly an adjustable racetrack type flight pattern with decreasing sizes over time based on prior

knowledge and human ground observation of the fire evolution. The work presented in this chapter lays a good foundation for future fixed-wing UAS missions for autonomous fire monitoring and real-time fire metric measurements. Based on lessons learned in this chapter, the following recommendations are provided for more effective fixed-wing UAS path planning for fire evolution mapping.

1. UAS cruise altitude: The UAS flight altitude needs to be carefully selected to reduce the impact of the fire-generated turbulence and smoke on the image quality. In this chapter, the KHawk UAS was flown at 120 m above ground such that it was not heavily impacted by fire-generated turbulence or smoke. This was partially due to strong winds ($\sim 6\ ms^{-1}$ from south) which blew most of the fire-generated smoke away from the UAS flight path directly above the fire.

2. UAS flight path: Cross-wind flight path is suggested on windy day, such that the UAS ground speed can be maintained throughout the mission for image acquisition at a constant spatial sampling distance.

3. UAS flight loops: The UAS needs to cover the study area repeatedly at regular time intervals. It is highly recommended that the UAS flies wings-level and straight over the study area for high-quality image collection and accurate image orthorectification. The UAS can turn outside the perimeter of the fire field and return to a stable and wings-level condition as it covers the fire.

4. Longitudinal and Lateral image overlapping constraint: Maintaining a desirable longitudinal and lateral overlapping percentages between images is important for the accurate georeferencing and orthorectification. The Agisoft Photoscan Pro software recommends a minimum of 60 % and 70 % for longitudinal and lateral directions respectively. Satisfying these requirements can be challenging due to limited availability of real-time fire information and safety precautions for the UAS. The effect of sub-optimal lateral overlapping can be seen in O_2 (the top right of Fig. 7). The images used to stitch this orthomosaic had less lateral

overlapping (< 70 %) near the bottom left and top right areas (holes can be seen in these areas) which impacted the quality of the orthomosaic. This is due to limited real-time fire information and ineffective path planning during the fire burning.

3.5.2 Effect of the Camera and Image Processing on Fire Evolution Mapping

The accuracy of the derived fire evolution map is highly affected by the imaging sensor and its associated image processing techniques. For fire observation, thermal images are highly preferred due to its ability, 1) to see through smoke and 2) easily differentiate fire regions and hot spots from the surroundings. In this study, we observed that the selected FLIR thermal camera provides high-quality data for fire evolution mapping and ROS measurement of tallgrass prescribed fires.

Unlike a general orthorectification process, which georeferences a set of images and stitches them, the multitemporal orthomosaic generation method first segregates the images into different groups based on the time they were acquired and then performs georeferencing and orthorectification for each group separately. Selection of these groups can be critical to the accuracy of the resulting orthomosaics, since the fire is constantly evolving. The fire observed by the KHawk UAS remained about the same along the longitudinal direction within a few seconds but changed along the lateral direction in between two flight lines, which can cause some errors in the orthomosaics. To minimize this problem, multiple images within one group that contain the fire at the same location need to be excluded from stitching. Additionally, images are recommended to be stable (no blurring) and nadir-facing for better spatial and stitching accuracy and quality, which can be challenging for some UAS data due to possible fire-generated turbulence. The orthomosaics shown in Fig. 3.7 are generated by careful selection and manual removal of images during each stitching process (Table 3.3).

3.6 Chapter Conclusions & Future Goals

This chapter described a low-cost, safe, and efficient method for fire evolution mapping and ROS calculation using thermal imagery collected by a fixed-wing UAS. The method was demonstrated using the KHawk UAS repeat-pass thermal images of a prescribed fire (530 m $\times$ 250 m) in Anderson County Prairie Preserve, Kansas, where the fire evolution map and associated fire ROS were calculated using four multitemporal orthomosaics at a time interval of about 2 minutes. The calculated mean head fire ROS of 0.27 ms^{-1} was found to have an uncertainty of 9 %. Based on our knowledge, this chapter provides the first remote sensing based measurement of fire ROS in tallgrass prairie in the Midwest USA. The derived fire ROS statistics can serve as a useful reference for future prescribed and wildfires in similar grasslands.

Future goals for fixed-wing UAS based fire evolution mapping and ROS measurement include, 1) Near real-time fire map generation, ROS measurement, and data transfer for fire situation awareness, 2) real-time UAS path adjustments based on fire spread behavior, 3) machine learning-based automatic fire front delineation, and 4) integration of cm-level RTK GPS on-board the UAS and use of GCP for improved orthorectification.

Chapter 4

Prescribed Grass Fire Mapping and Rate of Spread Measurement Using NIR Images from a Small Fixed-Wing UAS

4.1 Chapter Introduction

Accurate measurements of wildland fire behavior parameters such as spread direction and rate of spread (ROS) are critical to fire spread modeling and prediction. Nevertheless, it is difficult to measure wildland fire metrics given the unpredictability of fire spread in changing atmospheric and field conditions such as wind, relative humidity, temperature, fuel load characteristics, and terrain features [33]. These factors are generally used as inputs to fire spread models such as the Rothermel [34] and the CSIRO [35] models, which have been widely used to estimate and predict the fire ROS in many fuel types [36–39]. However, the effectiveness of these empirical models in fire ROS prediction is highly dependent on the accuracy and reliability of weather, fuel, and terrain information of the burn zone. Direct ROS measurements are often needed to evaluate and improve these fire spread models.

Many direct fire ROS measurements in the literature come from indoor observations through table-top and wind tunnel experiments [40, 41] or ground observations through towers or booms, which are limited to small scales and may not accurately depict the fire spread behavior in landscape scales across the whole burn zone. Direct fire ROS measurements from aerial observations can often facilitate the mapping of fire behavior in larger spatial scales, making them better suited for wildland fire measurements. Most existing airborne remote sensing-based direct fire ROS measurements use imagery from manned aircraft [12–14, 16]. The collected airborne imagery can be

post-processed for detection and extraction of fire fronts and ROS measurement. However, deploying manned aircraft over fires can be challenging due to adverse flight conditions (smoke and heat), limited flight path flexibility (to avoid turbulence), and high operating costs.

In recent years, small Unmanned Aircraft System (UAS) are increasingly used in fire missions. Small UAS are light-weight, easy to handle, and cost-effective, making them very handy for fire ROS measurements at low flying altitudes. Thermal cameras can be installed on these UAS for fire measurement due to their ability to see through smoke and measure temperature [42]. However, such thermal cameras are generally quite expensive and have lower image resolution as compared to RGB and modified near infrared (NIR) cameras [43], that are widely used among UAS operators. NIR images may be used for certain fire missions since it is not affected by smoke occlusion as much as RGB images [44]. The main challenge for NIR-based fire mapping is that it does not capture temperature changes and may create challenges in fire front detection. There have been a few studies on NIR-based fire detection using ground images [44, 45]. Airborne NIR-based fire detection has also been explored in literature, where aircraft NIR images are first converted to Normalized Difference Vegetation Index (NDVI) and then used for fire line detection and extraction [13].

The objective of this chapter is to develop a low-cost grass fire mapping and ROS measurement system using NIR aerial images from a fixed-wing UAS. The proposed methods can be directly adopted by other UAS operators with low-cost NIR cameras for fire mapping applications. The methods are demonstrated using a low-cost NIR UAS data set over a prescribed grass fire that was conducted in Welda, Kansas. The main contributions of this chapter are as follows.

1. A new method for spatiotemporal representation of grass fire evolution using time labeled UAS NIR orthomosaics generated from aerial images with limited footprints.

2. A UAS prescribed fire data set over a tallgrass field in Kansas, including short time-series NIR orthomosaics and local weather measurements (https://cusl.ku.edu/Flight Log).

3. A novel NIR intensity variance thresholding method for grass fire front classification and

extraction.

4. Discussions and lessons learned using low-cost NIR imagery for grass fire mapping.

4.2 Prescribed Fire and UAS Data

This section describes the prescribed grass fire and the UAS data that is used for the demonstration and analysis of the proposed methods.

4.2.1 Prescribed Grass Fire Event

A prescribed grass fire was conducted from 11:38 AM to 12:25 PM (US Central Time) by the Kansas Biological Survey (KBS) [46] at Welda, KS on October 8, 2019. The burn site is a relatively flat rectangular field ($530m \times 250m$) with uniform fuel vegetation cover dominated by C4 tallgrasses and a mixture of herbaceous forbs and legumes (shown in Fig. 4.1). A ring fire pattern was conducted by two fire setting teams using drip torches for ignition. The fire ignition was initiated near the center of the north boundary and terminated near the center of the south boundary, with one team travelling clockwise and the other travelling counter-clockwise from the initial point. The ignition process was completed around 12:17:32 PM after which the fire evolved naturally in the field. The boundary of the fire field is shown in Fig. 4.1. There were some inconsistencies in the fire ignition process with the teams having to spend more time to ignite the north east and north west corners. The weather conditions during the burn were measured in the field as 73°F temperature with 41% relative humidity and 6.26 ms^{-1} prevailing wind from the south. The wind measurement is from a Campbell Scientific CSAT3B wind anemometer installed at 1.9 m above the ground level close to the east boundary of the fire field, also shown in Fig. 4.1.

4.2.2 KHawk UAS Data

A KHawk 55 fixed-wing UAS was deployed over the prescribed fire for multispectral image acquisition. The KHawk 55 UAS is a low-cost multispectral remote sensing platform developed by the

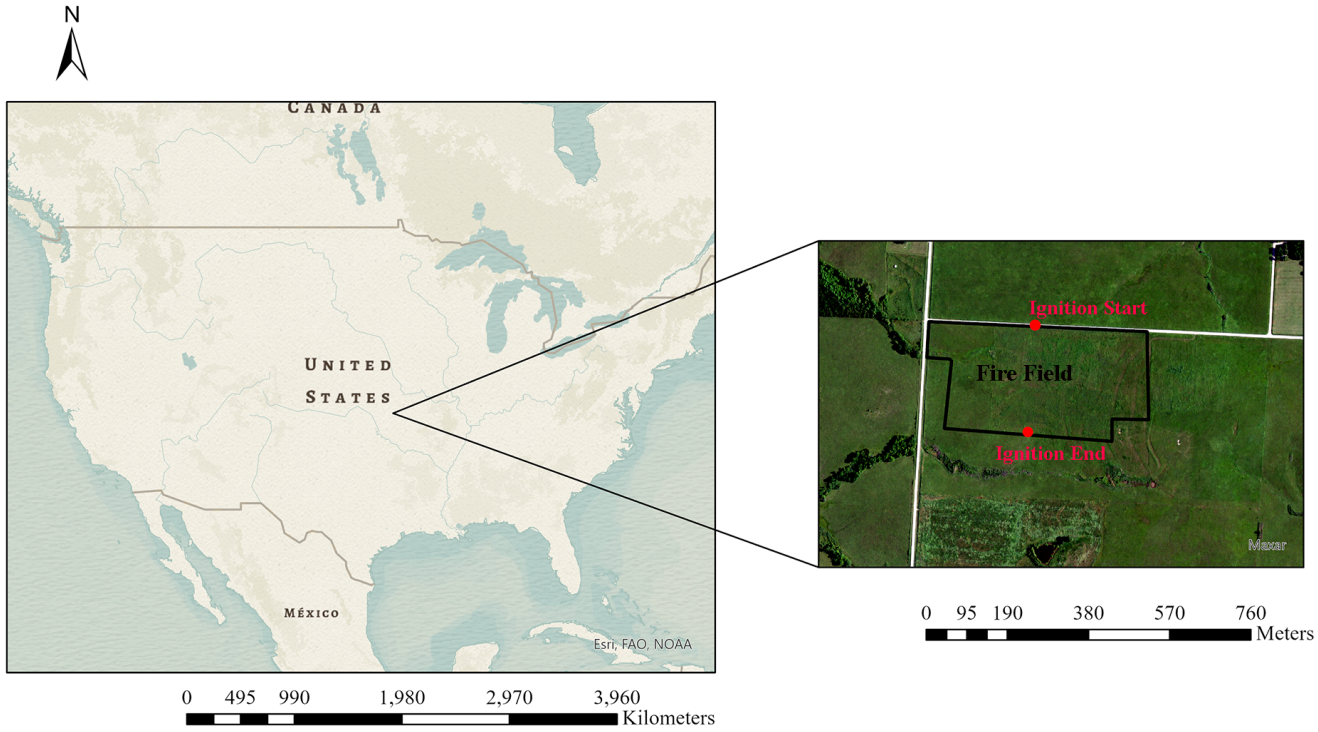

Figure 4.1: Anderson County Prairie Preserve: fire field (black perimeter) and prescribed fire ignition starting and end locations (red circle) labelled.

Cooperative Unmanned Systems Lab (CUSL) at the University of Kansas, shown in Fig. 4.3. It is equipped with a Ublox M8P Here GPS and a Pixhawk Cube autopilot (ArduPilot 2021), which can support both manual and autonomous flight. Key UAS specifications are provided in Table 4.1.

Table 4.1: KHawk 55 UAS Specifications

Description	Value
Take-off Weight	2.5 kg
Wingspan	1.4 m
Cruise Speed	20 ms^{-1}
Maximum Endurance	30 min
Typical Altitude	120 m

The KHawk UAS was equipped with a low-cost PeauPro82 modified GoPro Hero 4 Black camera for NIR video acquisition. This camera was modified with an 850 nm IR pass filter making it sensitive to light in the NIR spectrum and was operated in a video mode at a frame rate of 29.97 Hz with radiometric and pixel resolutions of 8-bit and 1080×1920 pix respectively (see Table 4.3). Manual synchronization is performed after the flight for image geotagging. Example images

of the fire field are shown in Fig. 4.2. It can be observed from this figure that the NIR images are partially obstructed by smoke.

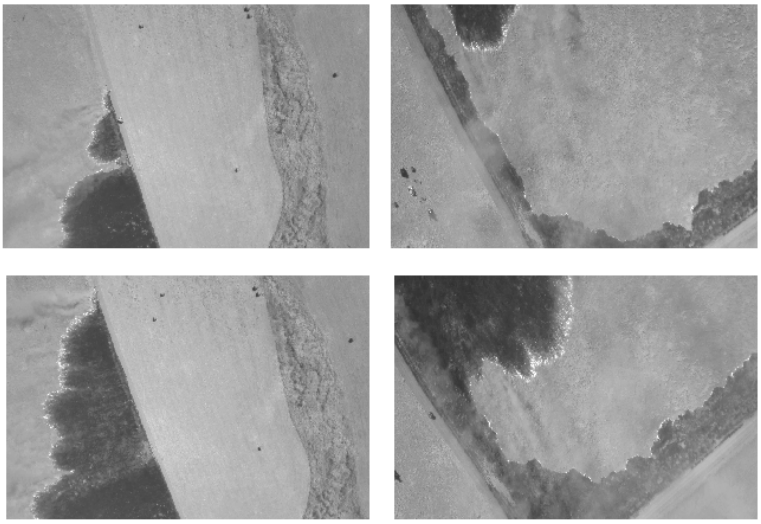

Figure 4.2: PeauPro82 GoPro NIR images of fire field.

Table 4.2: PeauPro82 Modified GoPro Hero 4 NIR Camera Specifications.

Description	Value
Spectral Bandwidth	825.4 to 880 nm
Sensor Resolution	1920×1080 pix
Field-of-View (FOV)	$74^\circ \times 45^\circ$
Frame Rate	29.97 Hz
Spatial Resolution (at 120 m above the ground)	0.1 m

The KHawk UAS was programmed to autonomously fly multiple loops over the burning field at 120 m above the ground level to collect repeat-pass imagery of the burning field. Here, repeat-pass imagery are defined as the images collected at the same location over the field at different time steps. The objective of such a flight plan is to collect images for the generation short time-series orthomosaics, where one orthomosaic corresponds to one flight loop. In addition to the pre-planned flight path, the ground control station operator can also perform real-time adjustments of flight loops based on the ground observation of the fire evolution. In this mission, the UAS completed one loop in around 2 minutes and achieved 4 loops in total from about 12:06 PM to 12:18 PM, with images from 3 loops used for orthomosaic generation. The majority of the UAS

flight path is overlaid on a National Agriculture Imagery Program (NAIP) image (spatial resolution of 1 m), shown in Fig. 4.3.

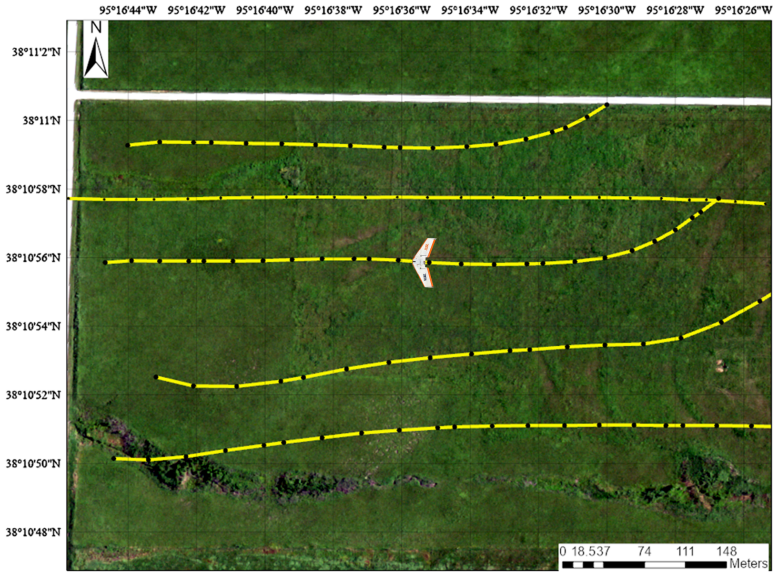

Figure 4.3: KHawk 55 UAS flight path during the fire.

4.3 Methods

This chapter introduces a new method for the mapping and ROS measurement of grass fires using low-cost NIR images from a small UAS. The first part of this method focuses on the spatiotemporal representation of the state of the fire field during different time intervals using short time-series orthomosaics generated using repeat-pass images with limited footprints. Different regions within an orthomosaic are then assigned time labels based on the time they are observed by the UAS. The second part is dedicated to fire front extraction from these orthomosaics using a novel NIR Intensity Variance Thresholding (IVT) method. Finally, these fire fronts are combined to form a fire evolution map that facilitates the calculation of the fire ROS. This section provides detailed descriptions of this method by presenting each of its main components.

4.3.1 Spatiotemporal Representation of the Fire Field Using Time-Labelled Orthomosaics

One of the main contributions of this chapter is a new method for the spatiotemporal representation of the fire field using UAS short time-series orthomosaics with time labels. Small UAS flying at low altitudes generally observe only small patches of the burning field at a time, which is not ideal for the mapping and measurement of fire spread. For the spatial representation of the fire spread within a specific duration of time, images from each loop can be grouped and orthorectified to form one orthomosaic. With the UAS collecting data in multiple loops over the fire field, short time-series orthomosaics can be generated [42] as shown in Fig. 4.4.

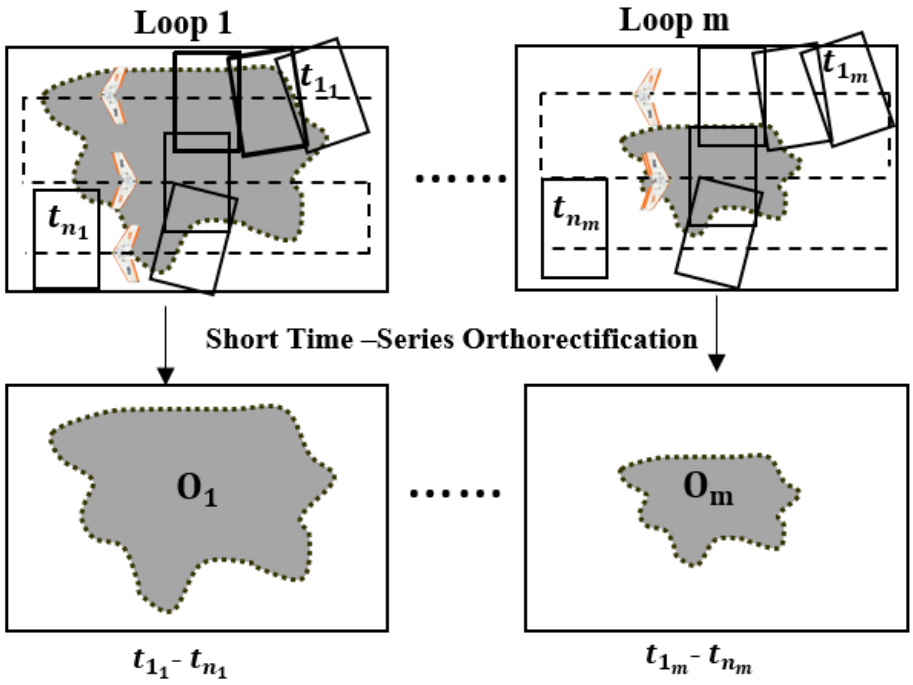

Figure 4.4: Short time-series orthomosaic generation.

Since each orthomosaic is formed using multiple images collected at different times, a time interval can be assigned to each orthomosaic, where the starting and ending time corresponds to the time stamps of the first and last image in the loop. This is illustrated in Fig. 4.4. However, such time representation may not be ideal for fire situational awareness and ROS calculation at finer scales since the fire front may evolve considerably within the assigned time interval. A new

data representation is proposed in this chapter to address this problem. The basic idea is shown in Fig. 4.5. Instead of using only one time step or a time period for an orthomosaic, the orthomosaic will be divided into small zones with their own time labels. The size of each time zone and time difference between them can be customized based on desired temporal resolution, camera footprint, and ground speed of the UAS. One way to determine the grid size is to use the camera footprint size at the flight altitude.

Given the UAS altitude of h above the ground and camera FOV of θ_x and θ_y, the size of one time zone in the orthomosaic can be computed as follows.

$$O_{m_t} = 2h\tan\frac{\theta_x}{2} \times 2h\tan\frac{\theta_y}{2}. \tag{4.1}$$

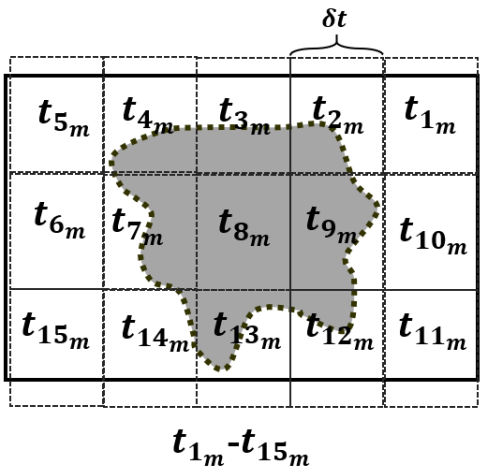

Figure 4.5: Time-labelling of fire field.

The generated orthomosaics are then analyzed to for fire front detection and extraction for the generate fire evolution maps. It is worth mentioning that the needed fire detection methods can vary depending on the spectral and radiometric properties of the images. In other words, fire front detection algorithms used for thermal images will not work for NIR images since the NIR band is mainly sensitive to vegetation while the thermal band is more sensitive to temperature.

4.3.2 NIR Intensity Variance Thresholding Method for Grass Fire Front Extraction

A new method is proposed for the fire front extraction problem based on airborne NIR imagery, which is called NIR Intensity Variance Thresholding (IVT) method. Given an NIR DN orthomosaic O_m of size $X \times Y$ pix. with pixel values ranging from 0 to 1 (normalized from 255 for an 8-bit image), the IVT method can be used to identify and extract the pixels that represent the fire front, O_{mf}. This method can be categorized into four steps, 1) image grid generation, 2) fire grid classification, 3) fire front extraction, and 4) fire front manual delineation as illustrated in Fig. 4.6. The main advantage of this method is that it uses NIR images in DN and not in surface reflectance and therefore doesn't require vicarious radiometric calibrations, making it inexpensive and feasible to UAS operators and researchers.

4.3.2.1 Fire Grid Classification

O_m is divided into n equally spaced grids of dimensions $x \times y$ pix. The size of the grid is selected based on the size of the image (see second row of Fig. 4.6). The main objective of this step is to classify the divided orthomosaic into fire and non-fire grids. This can be achieved by quantifying the pixel distribution within each grid. Non-fire grids can either be grids that represent only the burned or the unburned areas of the fire field.

The main difference between the non-fire grids and fire grids, Γ_F is that non-fire grids typically contain a smaller range of pixel intensity values with lower standard deviations, as they either represent burned areas (low-intensity values) or unburned areas (high intensity values), as illustrated in Fig. 4.7. Note that this figure shows the grids in normalized (0-1) DN values. The fire grid classification can be formulated as follows.

An orthomosaic, O_m can be classified into non-fire grids and fire grids Γ_F based on the distribution of all pixels enclosed within them. Two thresholds, α and β can be defined pertaining to the coefficient of variation CV and range R of each grid as criteria for classification. Here, CV_Γ is defined as the ratio of standard deviation σ_Γ and mean μ_Γ and R_Γ is defined as the difference

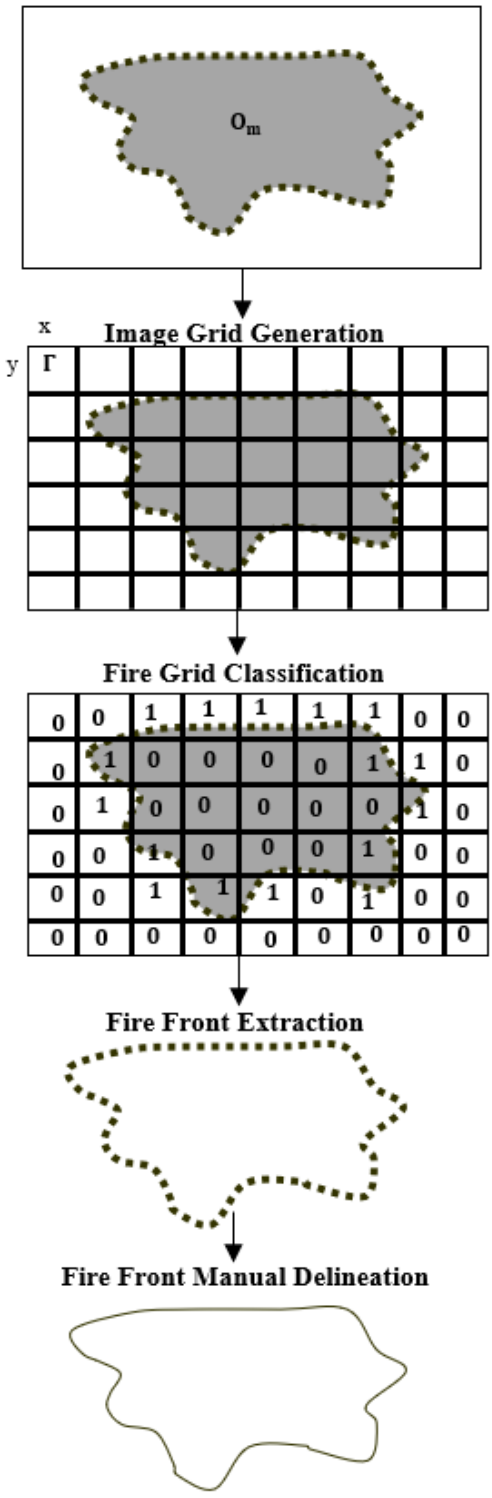

Figure 4.6: Intensity Variance Thresholding method.

between the maximum and minimum pixel values within a grid Γ. *The grids that satisfy the* α *and* β *criteria are classified as fire grids,* Γ_F *and are assigned as 1, while all other grids are classified*

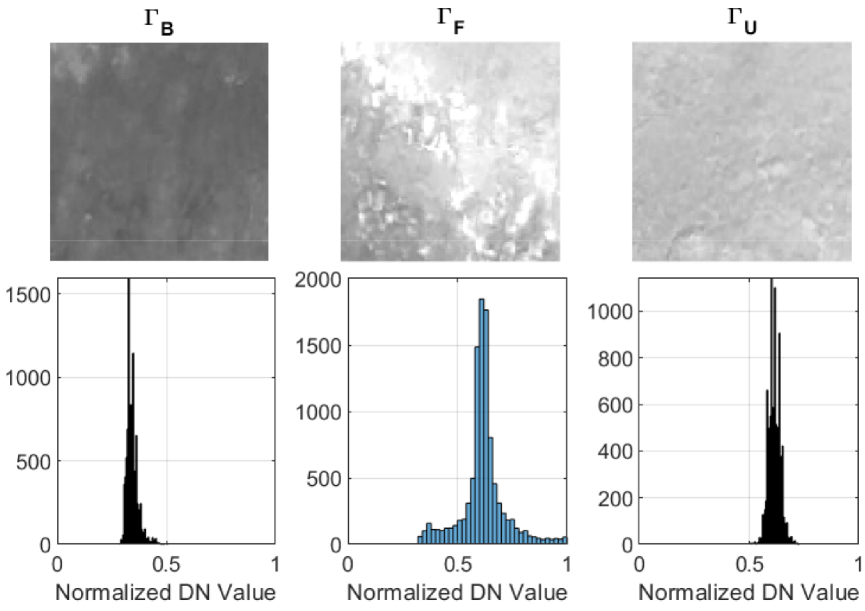

Figure 4.7: Examples of burned (left), fire (center), and unburned (right) grids and their respective histograms (bottom).

as non-fire grids and are assigned as 0.

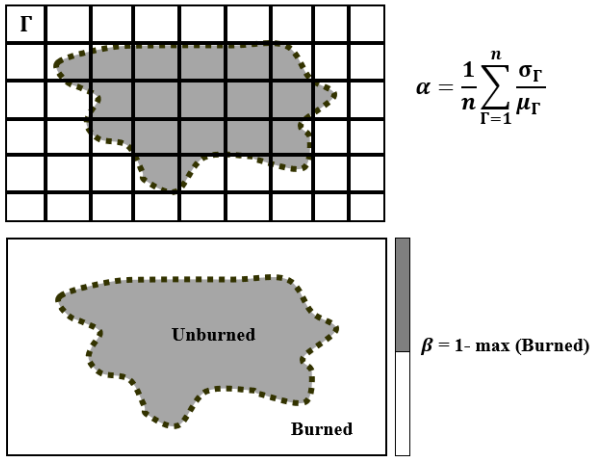

Figure 4.8: Fire grid classification thresholds: α (top) and β (bottom).

$$\Gamma = \begin{cases} 1, & \text{if } CV_\Gamma \geq \alpha \;\&\; R_\Gamma \geq \beta \\ 0, & \text{otherwise,} \end{cases} \tag{4.2}$$

where $CV_\Gamma = \frac{\sigma_\Gamma}{\mu_\Gamma}$ and $R_\Gamma = max(\Gamma) - min(\Gamma)$.

α-Selection The α threshold is to classify grids based on the extent of pixel intensity variability within the grid using the coefficient of variation CV. The α can be selected as the mean CV of all the grids.

$$\alpha = \frac{1}{n}\Sigma_{\Gamma=1}^{n} CV_\Gamma \tag{4.3}$$

β-Selection The β threshold is to classify grids based on the range of pixel intensity values within the grid. β can be determined empirically using the distribution of pixels in the orthomosaic O_m. The maximum pixel intensity value in O_b corresponding to the burned areas is used to calculate β.

$$\beta = 1 - max(O_{m,B}) \tag{4.4}$$

where $O_{m,B}$ are the pixels in O_m that represent the burned areas (low-intensity).

The reason for using the pixel intensity variation and range criteria is to ensure that the algorithm observes the distribution of all the pixels within a grid and not just the minimum and maximum values. For example, if only the range criteria is used, grids with smoke occlusion or saturated pixels may wrongly be classified as fire grids.

4.3.2.2 Fire Front Extraction

Given the identified fire grids in $x \times y$ pix. region, the next step is to locate the fire pixels within these regions for fire front extraction. This is also achieved using the pixel distribution within the fire grids. Since, these grids exhibit a Gaussian distribution (shown in Fig. 4.7) and the maximum pixel values enclosed within them can be identified as fire pixels, a threshold γ can be defined based on the empirical rule of a Gaussian distribution. The pixels within each Γ_F that satisfy the γ rule can be classified as fire pixels as shown below.

$$O_{mf} = \begin{cases} 1, & \text{if } \Gamma_{Fx,y} \geq (\mu_{\Gamma_F} + \gamma\sigma_{\Gamma_F}) \\ 0, & \text{otherwise,} \end{cases} \tag{4.5}$$

where $\Gamma_{Fx,y}$ is a pixel value at a location (x,y) within a Γ_F grid and γ is an empirically selected value between 2 and 3.

The value of γ can be empirically selected between 2 and 3, as according to the empirical rule for Gaussian distribution (68-95-99.7 rule), these values correspond to values above 95 % of a distribution.

4.3.2.3 Fire Front Manual Delineation

As shown in Fig. 4.6, the fire front extraction algorithm isolates fire pixels that are often discrete and undesirable for fire evolution mapping and ROS measurement. Therefore, the extracted fire front pixels can be manually joined to form a continuous fire front curve for better representation.

4.3.3 Fire Evolution Mapping

The delineated fire fronts from each orthomosaic are then combined to form a fire evolution map. The main components of this map include the fire front locations, associated time labels, and their spread direction vectors. For the spread direction vectors, a normal to the curve approach is used which is generally defined as the direction of the spread of a fire front [13, 30, 47]. An example of such a map is shown in Fig. 4.9.

The fire evolution map contains the information required to calculate the ROS for any given point along a fire front, namely, distance of spread, d_i and time difference, $(t_{n_{i+1}} - t_{n_i})$ as shown in Fig. 4.9.

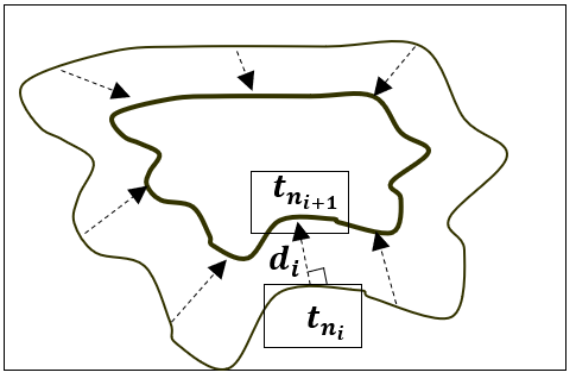

Figure 4.9: Fire evolution map and ROS calculation.

4.4 Results

The methods described in Sec. 3 are demonstrated using a GoPro NIR video collected by the KHawk 55 fixed-wing UAS over a Kansas prescribed grass fire. The detailed results and analysis are presented in this section.

4.4.1 Spatiotemporal Representation of the Fire Field Using Time-Labelled Orthomosaics

Repeat-pass individual frames are extracted from the NIR video and grouped accordingly for the generation of short time-series orthomosaics as shown in Fig. 4.10. Each orthomosaic is generated using the same processing parameters in the Agisoft Photoscan Pro software using about 120-150 NIR images. Using the time labelling descriptions and formulations provided in Sec. 3.1, each orthomosaic was roughly divided into 190 m $\times$ 110 m areas for time-labelling. Table 4.3 shows the number of images used and corresponding time intervals for each orthomosaic.

Table 4.3: Short Time-Series NIR Orthomosaic Properties.

Orthomosaic	Number of Images	Time Interval (Central)
O_1	147	12 : 07 : 03 – 12 : 09 : 19 PM
O_2	133	12 : 12 : 41 – 12 : 15 : 03 PM
O_3	119	12 : 15 : 26 – 12 : 17 : 47 PM

The orthomosaics shown in Fig. 4.10 are all registered to a NAIP image with a spatial resolution

Figure 4.10: NIR short time-series orthomosaics.

of 1 m using the ArcGIS Georeferencing tool. Note that the NAIP image was acquired on June 30, 2019 and has a 95 % confidence accuracy of around 6 m [32]. Control points pairs between each orthomosaic and the NAIP image were manually selected such that they covered the whole field. All the orthomosaics were registered using an Affine transformation and achieved a root mean square error (RMSE) of about 1.3 to 1.45 m, as shown in Table 4.4.

Table 4.4: Image-to-Image Registration Attributes for Short Time-Series NIR Orthomosaics Using 1 m NAIP Imagery.

Orthomosaic	Spatial Resolution (m)	Control Point Pairs	RMSE (m)
O_1	0.1	9	1.45
O_2	0.1	9	1.3
O_3	0.1	10	1.37

4.4.2 NIR-based IVT Method for Fire Front Extraction

The proposed IVT method (Sec. 3.2) is then implemented on the registered NIR orthomosaics for fire front extraction. First, the registered orthomosaics are divided into equally spaced grids Γ of size 100×100 pix. Then, the pixel distribution within each grid Γ is analyzed for fire grid classification. The NIR orthomosaics are normalized to 0-1 range, shown in Fig. 4.10. The α and β are selected as 0.02 and 0.6 respectively. All the grids with CV greater than 0.02 and range greater than 0.6 are classified as fire grids, while all the other grids are classified as non-fire grids, as shown in Fig. 4.11.

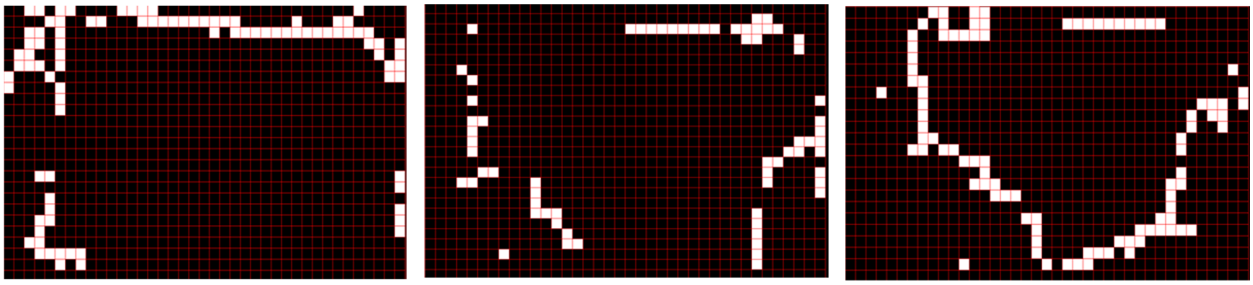

Figure 4.11: Fire grid classification.

The fire grids are then searched for fire pixel extraction using (4) in the previous section, where all pixels within a grid that satisfy the γ condition are classified as fire pixels while all other pixels are classified as non-fire pixels. It was found that the fire pixels within the classified fire grids represented the 95th percentile and above values. Therefore, γ was selected to be 2. Fig. 4.12 shows the extracted fire fronts from each orthomosaic. Finally, these fire front pixels are manually delineated using a line feature class in ArcGIS pro to form continuous fire front curves.

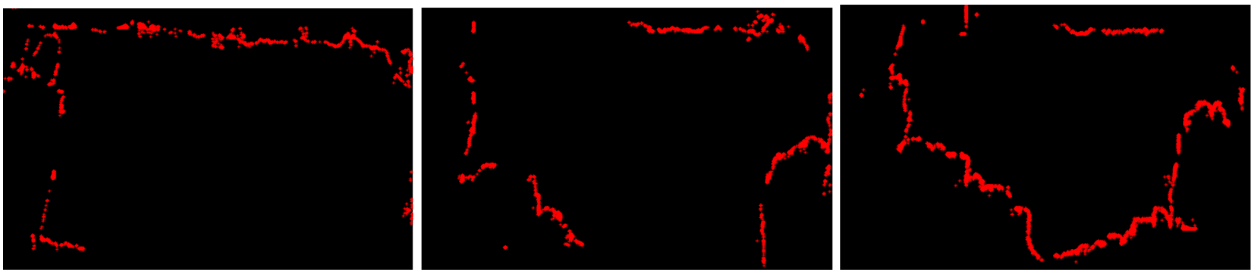

Figure 4.12: Fire front extraction.

4.4.3 Validation of Fire Front Extraction

Qualitative and quantitative validation analyses are conducted to show the effectiveness of the proposed IVT method. For qualitative validation, popular edge detection methods including, the Canny and LoG methods [48] are applied to the NIR orthomosaics and the results are visually compared to those generated by the proposed method. The objective of this analysis is to illustrate the effectiveness of the proposed method in rejecting noisy pixels such as saturated and smoke pixels that are not often rejected by existing edge detection methods. The Canny, LoG edge detection,

and the proposed IVT methods are applied to O_2 and shown in Fig. 4.13. From this figure, it is evident that proposed IVT method performs better than the existing edge detection methods for fire front extraction from high-resolution (0.1 m) NIR DN images. The main reason is that the IVT first identifies fire regions at a coarser resolution and then applies the fire front extraction algorithm to only those areas which rejects outliers that are often a problem when searching for the fire front directly in high-resolution images.

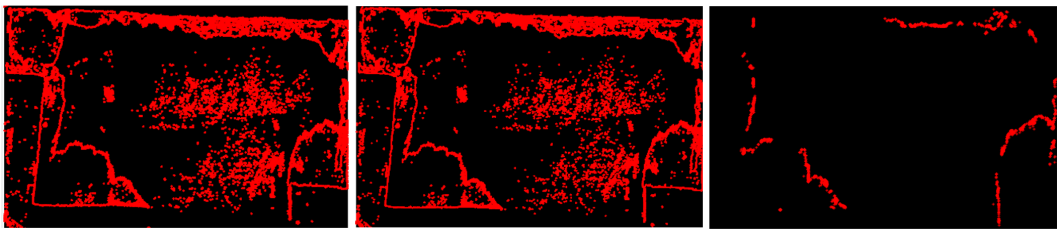

Figure 4.13: Qualitative comparison between fire fronts from Canny(left), LoG edge detection(center), and IVT methods (right).

For quantitative validation, the IVT extracted fire fronts are compared to manually extracted fire fronts from the orthomosaics. The minimum distance between the manual and IVT fire fronts are compared for error quantification.

Fig. 4.14 shows the manual and IVT fire fronts for O_2 on the left. On the right side of this figure, examples of high and low errors are shown. The high error area showed an error of 7.52 m which was the maximum error for O_2.

Table 4.5: Fire Front Error Statistics.

Orthomosaic	Min	Mean	Max	Std.
O_1	0.01	0.46	1.61	0.35
O_2	0.002	1.01	7.52	1.05
O_3	0.002	1.01	7.52	1.05

This analysis is conducted on all the NIR orthomosaics and the resulting errors are tabulated in Table 4.5. It can be observed that the mean errors for each orthomosaic are less than or around 1 m. This error is reasonable and does indicate that the IVT is effective in accurate extraction of fire fronts.

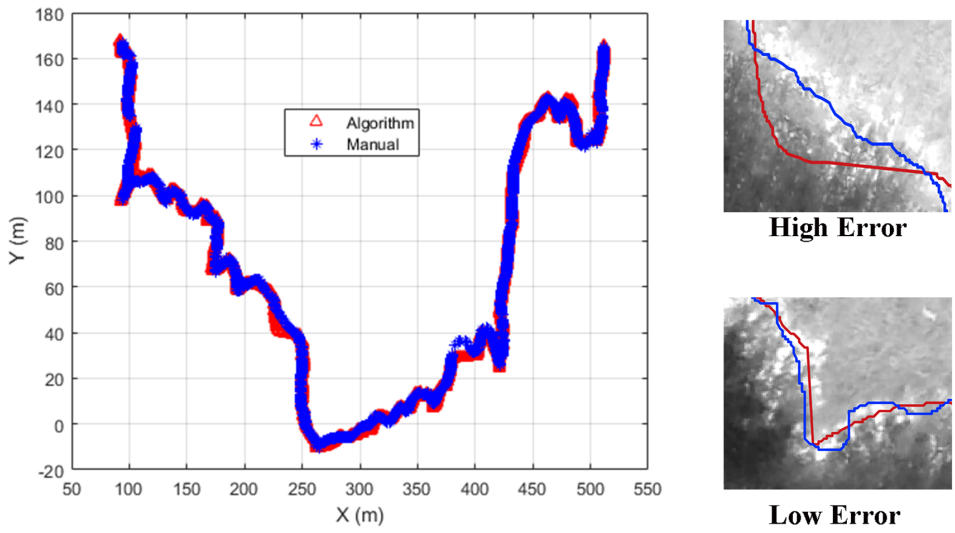

Figure 4.14: Quantitative comparison between manual and IVT fire fronts (left) and examples of high and low error regions (right).

4.4.4 Fire Evolution Mapping

The extracted and delineated fire front curves, f_1, f_2, f_3 are then combined to form a fire evolution map which provides information about the fire front location, spread direction, and the ROS. Fig. 4.15 shows the fire evolution map with labels defining the head fire, flank fire, and back fire. Only parts of the fire evolution map with smallest errors are used for ROS calculation and therefore have spread vectors defined. Certain regions with stitching inconsistencies are not used for the ROS analysis such as the west and east fire fronts of f_1.

The fire fronts shown in Fig. 4.15 are categorized into head, flank, and back fires based on the spread directions. Since this field experienced mainly south winds of 6.26 ms^{-1}, the fire fronts spreading north are categorized as the head fire, while the fire fronts spreading east or west are categorized as the flank fire, and the fire fronts spreading south are categorized as back fire.

The fire fronts with defined spread vectors are used to calculate the ROS. For analysis, the head and flank fire fronts are divided into two categorizes based on spread direction, NE, NW for the head fire front and E, W for the flank fire front. Note that these categories indicate the direction towards which the fire front is spreading. For example, the portion of head fire front spreading towards the NE is categorized as a NE fire front. The back fire ROS is calculated between f_1 and

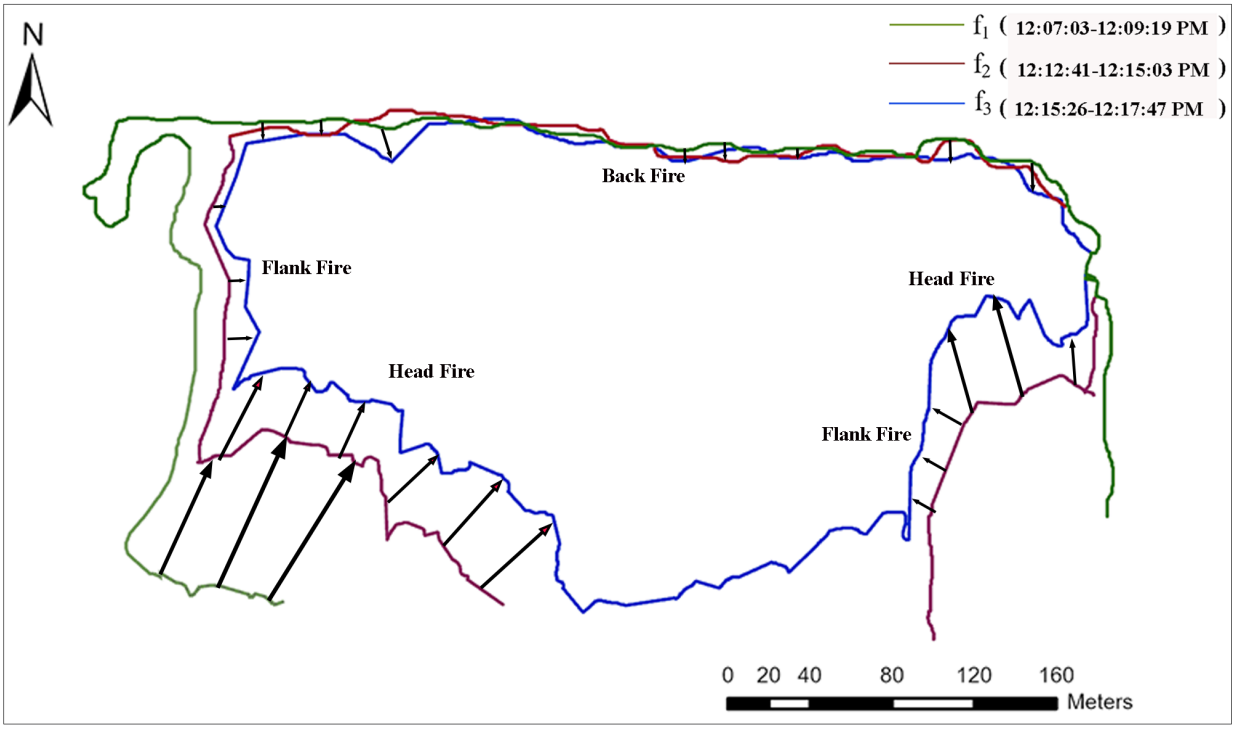

Figure 4.15: Fire evolution map.

f_3. The ROS between these fire fronts are calculated as described in Sec. 3.3 and tabulated in Table 4.6, Table 4.7, and ,Table 4.8.

Table 4.6: Head Fire ROS Statistics.

Fire Fronts	Min	Mean	Max	Std.
$f_1 - f_{2NE}$	0.21	0.24	0.25	0.016
$f_2 - f_{3NE}$	0.18	0.26	0.35	0.05
$f_2 - f_{3NW}$	0.27	0.45	0.44	0.07
		Cumulative		
	0.18	0.28	0.44	0.07

Table 4.7: Flank Fire ROS Statistics.

Fire Fronts	Min	Mean	Max	Std.
$f_1 - f_{2E}$	0.04	0.06	0.07	0.001
$f_2 - f_{3E}$	0.03	0.06	0.09	0.02
$f_2 - f_{3W}$	0.02	0.1	0.2	0.06
		Cumulative		
	0.02	0.1	0.2	0.06

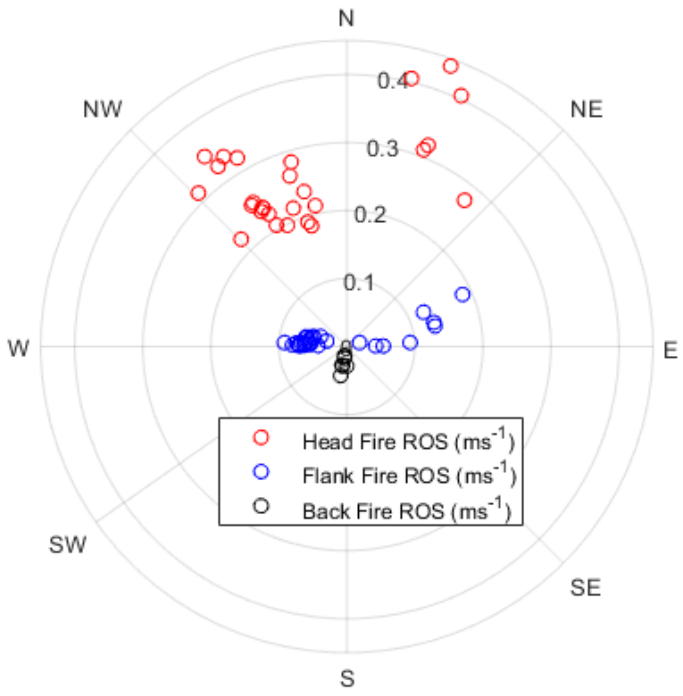

Figure 4.16: ROS polar plot.

Table 4.8: Back Fire ROS Statistics.

Fire Fronts	Min	Mean	Max	Std.
$f_1 - f_3$	0.0136	0.025	0.0435	0.0106

From these tables, it can be observed the mean head fire, flank fire, and back fire ROS are found to be 0.28 ms^{-1}, 0.1 ms^{-1}, and 0.025 ms^{-1} respectively. The measured ranges of head fire, flank fire, and back fire ROS are $0.18-0.44$ ms^{-1}, $0.02-0.2$ ms^{-1}, and $0.01-0.04$ ms^{-1} respectively. further visualized in a polar plot, as shown in Fig. 4.16.

4.5 Chapter Conclusions & Future Goals

This chapter proposed a novel NIR-based grass fire mapping and ROS measurement method that uses UAS short time-series orthomosaics with time labels. This method uses low-cost NIR cameras instead of expensive thermal cameras, which are feasible to many UAS operators. Moreover, the proposed method is developed for DN images and does not require vicarious radiometric calibra-

tions that can be challenging for UAS images. This method was demonstrated using a GoPro NIR video that was collected by KHawk fixed-wing UAS when flying multiple loops over a prescribed grass fire (530 m $\times$ 250 m) in Welda, KS and yielded an accurate fire evolution map (about 1.5 m registration error compared to the NAIP image), using three NIR short time-series orthomosaics at regular time intervals (about 2 minutes). Finally, it was found that this prescribed grass fire had mean head fire, flank fire , and back fire ROS of 0.28 ms^{-1}, 0.1 ms^{-1}, and 0.025 ms^{-1} respectively.

Future goals for fixed-wing UAS based fire evolution mapping and ROS measurement include 1) Real-time fire mapping and ROS measurement for better fire situation awareness, 2) autonomous UAS path adjustments based on onboard fire spread measurements, 3) machine learning-based automatic fire front delineation, and 4) integration of cm-level RTK GPS on-board the UAS and use of GCP for improved orthorectification.

Chapter 5

Spectral Reflectance Estimation of UAS Multispectral Imagery Using Satellite Cross-Calibration Method

5.1 Chapter Introduction

Unmanned aircraft systems (UAS) have been widely used for many multispectral remote sensing applications, including tornado damage track identification [49, 50] agriculture mapping [51–53], and forest fire monitoring [13, 21, 54]. UAS aerial images can facilitate real-time observations for regions of interest at high spatiotemporal resolutions (e.g. sub-meter spatial resolution and hourly temporal resolution), which can enable small-scale feature detection that may or may not be clearly visible in satellite or aircraft imagery. They can also provide data under cloudy conditions when satellite and aircraft imagery are obstructed. However, the biggest challenge for UAS based multispectral remote sensing is the retrieval of reflectance from raw orthorectified UAS images in digital numbers (DN).

In recent years, there have been notable contributions towards ground based-radiometric calibration methods for UAS multispectral imagery [55, 56]. The most popular methods use either commercial or customized ground reflectance target boards as a reference before, during, and after the UAS flight to identify the relationship between DN and reflectance for each spectral band. A semi-automatic-model-based method was proposed to convert raw UAS images to reflectance using a white Barium Sulfate panel and a Halon board [57]. Similarly, a customized gray gradient Masonite panel with nine different levels was used for UAS image radiometric calibration using a simplified empirical line method [58]. Their results showed that the relationship between UAS

imagery in DN and reflectance is non-linear for many commercial off-the-shelf cameras. Recently, a subband empirical line radiometric calibration method was proposed using a six-band miniature multiple camera array (mini-MCA) by Tetracam [59], which used standard diffuse panels as reference boards. The above methods have been widely used in research communities for reflectance estimation of UAS images. However, they are dependent on the accuracy and the Lambertian properties of the reference boards. To avoid this issue, most UAS groups use spectroradiometers before every survey mission to accurately measure the reflectance of the reference boards. These instruments can be expensive and not feasible to many UAS end users, who are constrained by a budget. In addition, there are many existing UAS data sets which have not been converted to spectral reflectance due to lack of ground spectroscopy measurements.

Satellites have been the primary source for large-scale multispectral remote sensing applications including burn severity mapping, earthquake damage assessment, and landslide extent mapping [60, 61]. Free and open satellite data can be obtained from National Aeronautics and Space Administration's (NASA) Landsat, Terra, Aqua, and European Space Agency's (ESA) Sentinel. However, these satellites provide imagery at lower spatial resolutions (10 m or lower) with relatively slow revisit times (1 - 16 days).

While satellite imagery possesses reliable radiometric accuracy, UAS can acquire images at desirable spatiotemporal resolutions, which has led to efforts towards understanding the relationship between UAS and satellite remote sensing data. High-resolution aerial observations from UAS were used to increase the spatial resolution of satellite data for precision agriculture [62]. Similarly, the variations in Normalized Difference Vegetation Index (NDVI) across different pixel scales were studied among canopy and non-canopy vegetation using various sensing payloads including UAS cameras, Landsat 8 (L8) Operational Land Imager (OLI), and the Moderate Resolution Imaging Spectroradiometer (MODIS) [63]. Airborne data from manned aircraft has also been explored for multispectral remote sensing [64]. Detailed statistics and cost analysis between UAS, manned aircraft, and satellite remote sensing platforms were provided for precision viticulture applications [65] and a satellite-based local bidirectional reflectance distribution function

(BRDF) correction method was introduced for radiometric correction of digital aerial images using data from Landsat 5 and 7 [66]. While satellite, manned aircraft, and UAS all have their own advantages and disadvantages, it is important to understand the radiometric relationships of different remote sensing data from various sources for future integrated and improved earth observations using multi-source and multi-scale data.

For accurate integration and comparison of remote sensing data, UAS and satellite reflectance imagery acquired at the same time are preferred to minimize radiometric differences. However, this can be difficult to guarantee due to other constraints. In such cases, satellite imagery acquired a few days before or after the UAS campaign can be used for radiometric studies and comparison. UAS and RapidEye images three days apart were used for precision viticulture applications [65] and L8 images acquired one day before the UAS survey were used to study NDVI variations in the canopy and non-canopy vegetation [63]. Similarly, an adaptive approach for precision agriculture was developed where drone and L8 images acquired 7 days apart were used [67] and L8 images acquired two days after a UAS mission were compared to reflectance and NDVI acquired by commercial digital cameras for multitemporal vegetation monitoring [68].

This chapter focuses on development of a low-cost cross-calibration method for estimation of UAS spectral reflectance at high spatial resolution using satellite reflectance data of the same area which can be beneficial to UAS operators and research groups who want to: 1) collect new UAS data but do not possess accurate spectroradiometers and ground target boards, 2) calibrate existing UAS data collected without a ground reflectance reference, and 3) study the radiometric relationships between multi-scale remote sensing data from satellite, manned aircraft, and UAS for enhanced Earth observations. The proposed method is demonstrated using orthorectified UAS DN imagery and L8 OLI Level-2 (L2) surface reflectance (SR) data of a forest/grassland area in Kansas. The cross-calibration functions between these two data are first identified for each spectral band and then used to convert high-resolution UAS DN images to reflectance. The proposed Satellite-based Cross-Calibration (SCC) method is finally validated by comparing the estimated UAS reflectance images with National Ecological Observatory Network (NEON) Image spectrom-

eter (NIS) atmospherically corrected SR data.

5.2 UAS and Satellite Remote Sensing Data

This section provides descriptions of the study area and the remote sensing data used to formulate and validate the proposed method.

5.2.1 Study Area

An area of 0.5 square kilometers in Kansas is selected as the study area (Fig. 5.1). It is located at $39.054^{\circ}, -95.190^{\circ}$, elevation 331 m in the deciduous forest and tall grass prairie ecotone of north-eastern Kansas [69]. Fig. 1 shows the study area and the corresponding orthorectified UAS image. Note that this area contains a 32-subplot hayfield (labelled in Fig. 5.1) close to the northwest boundary, which is maintained annually by the Kansas Biological Survey (KBS). Each subplot (10 m $\times$ 10 m) is given the same treatment (seeded, fertilized, or hayed) and is maintained to have the same vegetation. This hayfield is well suited for validation of the proposed SCC method. This area is also one of the 81 NEON field sites, a 30-year ecological monitoring project, and one of the most extensive initiatives of the National Science Foundation (NSF) [70].

5.2.2 UAS Data

A low-cost fixed-wing UAS, shown in Fig. 5.2 is used for multispectral image acquisition. It is equipped with a Ublox-Lea 6h GPS receiver and a Paparazzi TWOG autopilot, which can support both manual and autonomous flight. The detailed specifications are provided in Table 5.1. The UAS can carry one camera at a time for image acquisition. In this chapter, two PeauPro82 modified GoPro Hero 4 Black cameras [1] are used for multispectral image acquisition with one providing imagery in the visible spectrum (RGB) and the other in the NIR spectrum. The spectral characteristics of the modified GoPro camera are shown in the end of this section.

The UAS was deployed for multispectral data acquisition over the study area on June 7, 2017.

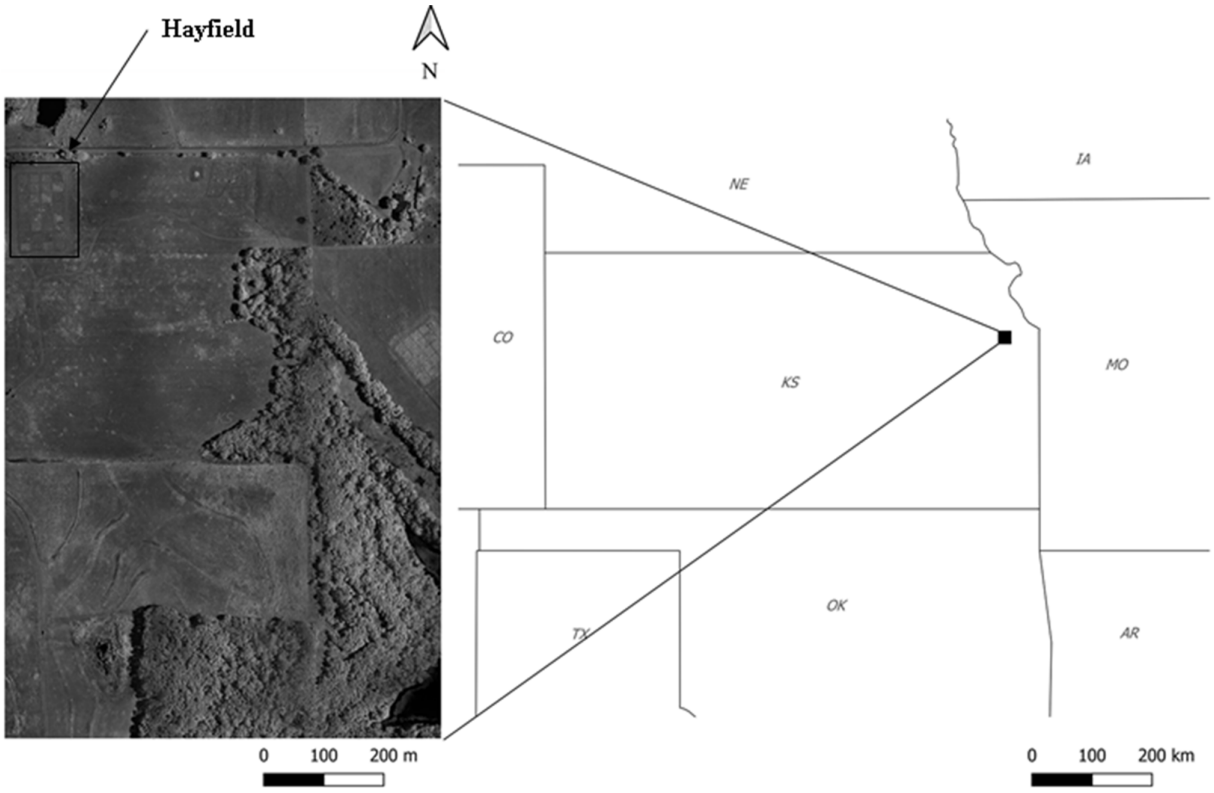

Figure 5.1: Study area.

Table 5.1: UAS Specifications

Description	Value
Take-off Weight	1.7 kg
Wingspan	1.2 m
Cruise Speed	16 m/s
Endurance	30 min
Spatial Resolution (at 120 m above the ground)	0.1 m

Two flights were conducted, one for NIR (09:49-10:19 AM) and the other for RGB (12:11-12:32 PM) video acquisition. It was flown autonomously at an altitude of 120 m above ground level with a minimum horizontal and vertical overlapping percentage of 75% between flight lines to ensure accurate image orthorectification. The UAS flight locations (white circles) used for the orthorectification are also overlaid to show the flight trajectory. The acquired UAS images were georeferenced and orthorectified using Agisoft Photoscan Professional software to produce orthomosaics in visible and NIR bands at a spatial resolution of 0.1 m, shown in Fig. 5.2. The spatial accuracy of the

generated orthomosaics were calculated by performing a comprehensive comparison with ArcGIS World Image which has a spatial resolution of 0.5 m or better in the continental United States [71]. A total of 10 high-quality control point pairs were randomly selected from the UAS and ArcGIS World images and compared. The horizontal root mean squared error (RMSE) is 4.72 m.

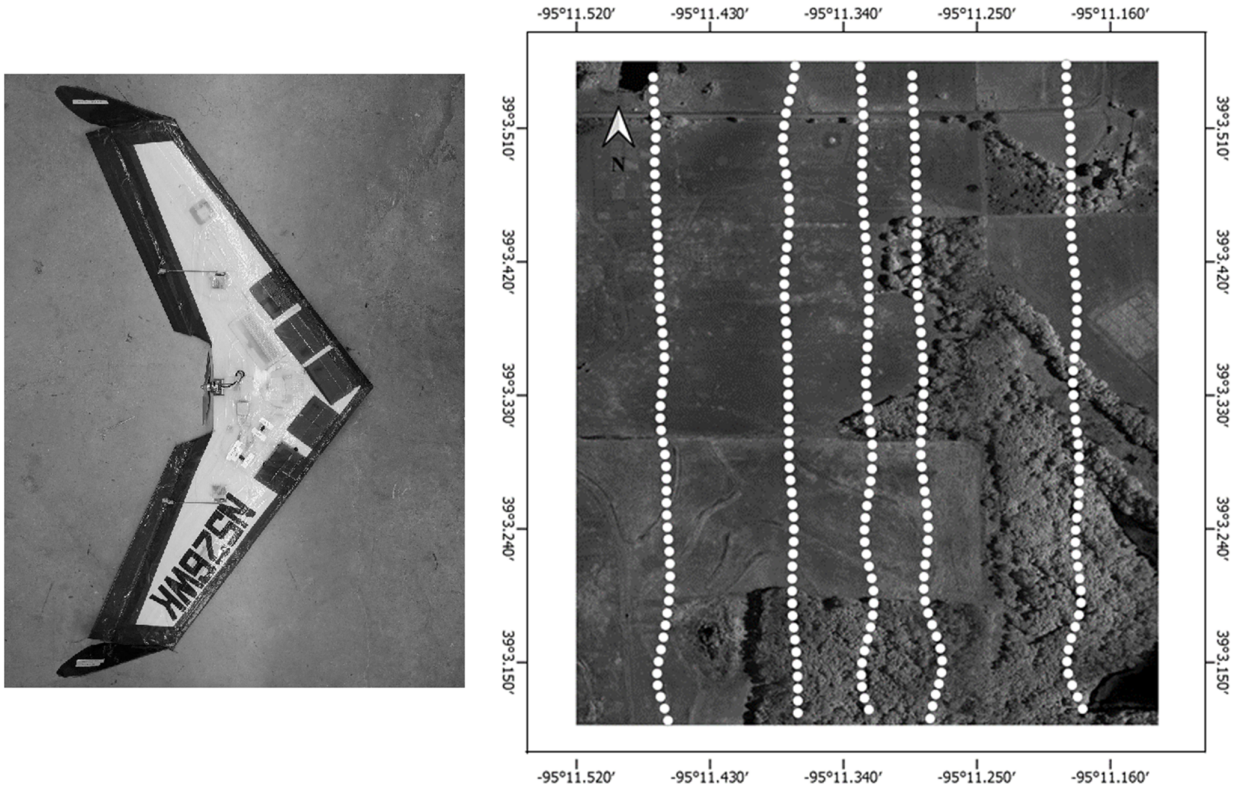

Figure 5.2: Fixed-wing UAS (L) and UAS flight path over the study area (R).

5.2.3 Landsat 8 Satellite Data

The L8 satellite is equipped with OLI and Thermal Infrared Sensor (TIRS) instruments for multi-spectral image acquisition. The OLI measures light at 9 spectral bands ranging from 430 to 1380 nm [72] . Operating at an altitude of 705 km above ground level, the OLI can provide calibrated reflectance images of the Earth every 16 days at spatial resolutions of 15 m (panchromatic band) and 30 m (all other bands). In this chapter, OLI L2 SR images of the study area acquired on June 7, 2017 at 12:00 PM are used to demonstrate the proposed method. The OLI L2 SR images are de-

rived through the atmospheric correction of OLI Level-1 (L1) products using the Landsat Surface Reflectance Code (LaSRC) algorithm [73]. The L8 OLI images demonstrate a spatial accuracy of 12 m or better [74].

The GoPro and OLI sensor spectral characteristics [1] are compared and shown in Table 5.2. It can be observed that the NIR band of OLI is similar to the GoPro camera while the Red band of OLI is narrower than that of the GoPro camera.

Table 5.2: Spectral Characteristics of UAS and L8 Remote Sensing Systems

Sensor	Bands	FWHM (nm)	Peak (nm)
OLI	Red	635.85 – 673.32	654.59
	NIR	850.54 – 878.79	864.67
Modified PeauPro 82 GoPro (RGBt)	Red	583.9 – 710	627.6
Modified PeauPro 82 GoPro (NIR)	NIR	825.4 – 880	852.7

5.3 Spectral Reflectance Estimation of UAS Imagery: Conversion from DN to Reflectance Value

This section provides detailed descriptions of the proposed method for spectral reflectance estimation of multispectral UAS DN imagery. The objective of this method is to convert raw UAS images in DN at high spatial resolution to reflectance using available satellite reflectance data. The main advantage of this method is that spectral reflectance can be estimated from UAS DN images for free or at very low-cost. In addition, this method will ensure high similarity between the UAS and satellite imagery, which can later be used for multi-scale remote sensing of large fields such as crop monitoring and disaster assessment. The proposed method can be broken into the steps below for researchers who want to collect new UAS data.

1. UAS Campaign Planning - Plan the UAS survey based on the availability of satellite data and favorable weather conditions. UAS campaign should follow the time schedule of satellite imagery collection.

2. UAS Data Processing - Collect UAS multispectral imagery of a given region of interest and perform georeferencing and orthorectification.

3. Satellite Data Acquisition - Satellite reflectance data of the region of interest should be acquired based on certain factors including acquisition time, cloud cover, and atmospheric correction (explained in further detail in Sec. 3.1).

4. Cross-Calibration and Conversion - After the acquisition of UAS DN and satellite reflectance imagery, the SCC method can be implemented to identify the cross-calibration function for each spectral band (explained in further detail in Sec. 3.2). The identified cross-calibration function can then be used to convert raw UAS DN imagery to reflectance values.

For researchers who already acquired their raw UAS data without ground calibration boards or ground spectrometer measurements, the following steps can be used instead.

1. Find suitable reference of surface reflectance either from satellites (L8, Sentinel 2, Planet, etc.) or from airborne data (NAIP, NEON, etc.).

2. UAS Data Processing – (same as above).

3. Cross-Calibration and Conversion – (same as above).

5.3.1 Satellite Data Acquisition

Satellite reflectance data for a given region of interest (UAS survey area) can be downloaded for free or at low-cost from designated websites such as United States Geological Survey (USGS) Earth Explorer, Copernicus Open Access hub, Planet, etc. Reflectance data from any satellite (Landsat, Sentinel, Planet, etc.) can be used in this method and the following factors need to be considered during the selection.

1. Acquisition Time: The satellite data acquisition time can be a critical factor in the effectiveness of the method. It is desired that the satellite data is acquired at the same time as that

of the UAS image so that the reflectance is the same. In case of unavailability of such data, satellite data acquired close to the time of UAS campaign can be potentially used.

2. Cloud Cover: Ideally, cloud free satellite observations of the region of interest are desired. In cases with partial cloud obstruction, the unobstructed areas can be used to identify the cross-calibration functions which can then be used to calibrate the UAS data in cloud-obstructed areas. If there is a total cloud obstruction, satellite images acquired before or after the UAS survey can be used if available.

3. Atmospheric Correction: Satellite images are required to be atmospherically-corrected to convert UAS DN to surface reflectance. Therefore, level 2 data is recommended.

Satellite images acquired at the same time with UAS are preferred for this method. In cases where no satellite images are available, aircraft imagery from National Agriculture Imagery Program (NAIP) or NEON can also be used. The main requirement is to have a reference reflectance image of the same area as the UAS survey. The satellite-based cross calibration method is described in the following subsection.

5.3.2 Satellite-based Cross-Calibration Method

Given an orthorectified UAS image X' in DN at high spatial resolution ($kM \times kN$ pix.) and a satellite atmospherically-corrected reflectance image Y at medium spatial resolution ($M \times N$ pix.), a cross-calibration function $F(X')$ can be identified for each spectral band that can convert UAS images in DN at high spatial resolution to spectral reflectance. Here, k is the ratio between the spatial resolutions of satellite and UAS images which can be derived from the dataset. For example, k is 30 if the spatial resolutions of satellite and UAS images are 30 m and 1 m respectively. The main steps of this method (Fig. 5.3) include:

1. UAS image resampling: Resample the high-resolution UAS image (X') to a medium-resolution image (X) to match the spatial resolution of the satellite image (Y). Existing methods like

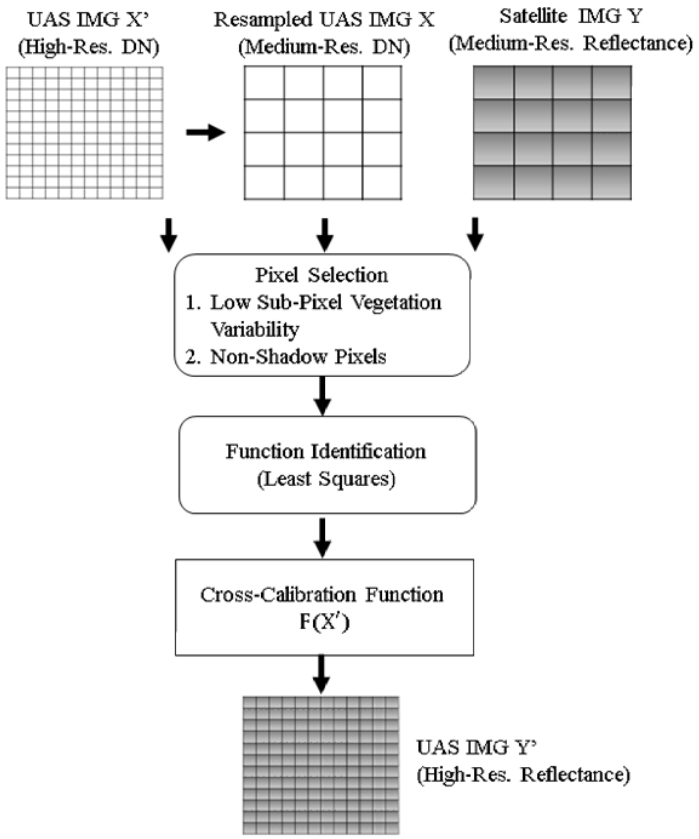

Figure 5.3: SCC method flowchart.

nearest neighbor, bilinear, or bicubic methods can be used. Bicubic interpolation is used in this work.

2. Pixel selection: Select UAS and satellite pixel pairs at medium spatial resolution, (X_1, Y_1) which is a subset of the original UAS and satellite image pair, (X, Y). Here, the objective is to exclude pixels that can potentially induce errors in the function identification and is explained in detail later in Sec. 3.2.1.

3. Function identification: Use least-square optimization methods to find the optimal cross-calibration function based on selected pixel pairs.

4. UAS reflectance estimation: Apply the identified function to the high-resolution UAS DN

image (X') and finally obtain UAS reflectance image (Y').

5.3.2.1 Pixel Selection

In this work, the pixel pairs are selected based on two conditions, a) low sub-pixel variability and b) non-shadow pixels.

The first condition is to exclude pixels with high sub-pixel variability within a medium-resolution pixel (e.g. a 30 m $\times$ 30 m area for one OLI pixel). This is an important step as it can reduce the impact of mixed pixel effect of the lower satellite image on the overall method. Essentially, this condition filters out the pixels that correspond to areas with varying vegetation such that all the pixels in the UAS image that correspond to one pixel in the satellite image represent the same vegetation. This is determined based on the sub-pixel Coefficient of Variation (CV), calculated from high spatial resolution UAS image in DN. CV is the standard deviation divided by the mean value (σ/μ) within a pixel at medium resolution. The concept is further shown in Fig. 4. CV_B represents the CV of pixel B in X calculated using the mean (μ_A) and standard deviation (σ_A) of all the pixels in a subgroup $A(k \times k$ in $X')$. A threshold can be empirically defined to exclude all pixels in X with higher CV. The recommended threshold can be selected as the mean CV of all the pixels in the image, $\bar{CV}$.

The second condition aims to exclude all the shadow pixels. Generally, UAS images collected at low altitudes tend to capture leaf canopy shadows. Since these shadows may not be observed in fine detail from satellite images due to lower spatial resolutions and may also show different patterns due to different acquisition time and different viewing angles/distance, it is not recommended to include the shadow regions for function identification. An empirical pixel thresholding method can be used to detect shadows in the UAS images, where thresholds can be applied to identify all the shadow pixels [75]. It is worth mentioning that there exist other feature-based image processing methods for shadow detection which can also satisfy this condition. After detection of the shadow pixels in high resolution UAS imagery, the corresponding pixels in resampled UAS imagery at medium resolution can then be rejected.

In summary, the low sub-pixel variability condition can be first applied to the UAS image, X, which rejects pixels exhibiting high sub-pixel variability ($CV \geq \bar{CV}$). This condition detects and rejects many shadow pixels as long as the shadows occupy only a portion of the pixel. However, in cases where pixels are mostly covered with shadows, the second condition is needed.

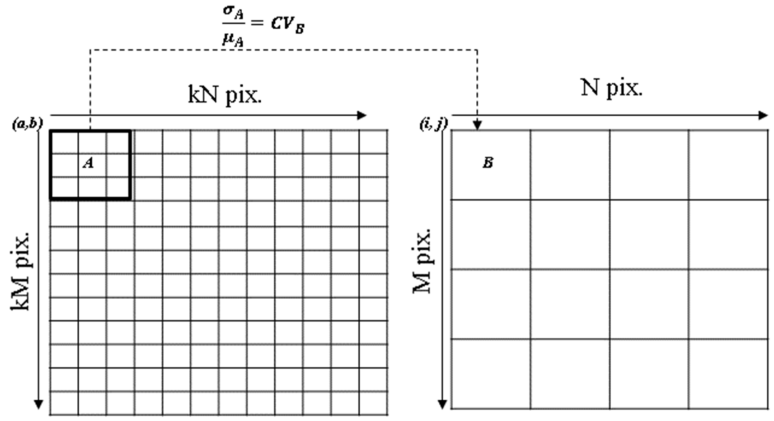

Figure 5.4: Coefficient of variation calculation using images X' (L) and X (R).

5.3.2.2 Function Identification

The objective of this step is to identify the cross-calibration functions between the selected sample, (X_1, Y_1). Both linear and nonlinear functions have been used in the literature to convert DN to reflectance. In this chapter, the exponential function is selected based on recent literature [58, 59] using similar cameras (commercial grade). The Ordinary Least Squares (OLS) and Weighted Least Squares (WLS) regression methods are used for the parameter identification of the optimal cross calibration functions.

Ordinary Least Squares The OLS method is used to estimate the unknown parameters in a linear regression model by minimizing the sum of squared errors. It is worth emphasizing that, the OLS method is optimal under the assumption that the errors or the residuals are homoscedastic and serially uncorrelated across the measurement range [76]. For remote sensing images from different sources and at varying spatial resolutions, there is a high possibility of outliers and changing uncertainties across the reflectance range which may violate this condition.

Weighted Least Squares When the OLS assumption of constant variance in the errors is violated (not homoscedastic), the WLS method can be used. The main difference is that in WLS, each data point in the given set of observations is weighed differently based on their resulting error variance. For example, data points with high error variances (e.g. outliers) are weighed very low compared to points with lower error variances. As a result, the WLS method is less sensitive to outliers as compared to the OLS method and has been used in remote sensing [77–79]. Another difference is that the WLS minimizes the sum of weighted squared error instead of sum of squared error as shown below [80].

$$S = \sum_{i=1}^{n} w_i (y_i - \hat{y}_i)^2, \tag{5.1}$$

where w_i are the weights of each data point.

In this chapter, a variant of the WLS, called the Iteratively Weighted Least Square Regression (IWLSR) is used. This method has been successfully implemented for automatic relative radiometric normalization of satellite imagery [77]. The IWLSR method, initialized with the error residuals from the OLS method iteratively determines the optimal weights for each data point in the given set of observations. The method is described below [77].

Consider a set of observation data, (x_j, y_j) such that $j = 1, 2, 3....n$. The OLS is first used to estimate the slope and intercept, m and p respectively, such that:

$$y_j = mx_j + p + \varepsilon_j, \tag{5.2}$$

where ε_j is the error residual for the jth data point. Next, a variable t is defined such that $t = \varepsilon/\sigma_\varepsilon$, where σ_ε is the standard deviation of the error residual vector. Here, t is an approximate one degree of freedom chi-square distribution ($\chi^2(1)$). This is used to calculate the weight vector, w, for the next iteration.

$$w = P\{\chi^2(1) > t\} = 1 - P\{\chi^2(1) \leq t\}. \tag{5.3}$$

P in the above equation represents the chi-squared cumulative probability function. The above steps constitute one iteration. With the new weights, the updated slope and intercept are calculated, which starts the next iteration. The algorithm runs until the difference in the weights between two consecutive iterations falls below a specified value.

Finally, cross-calibration functions are identified for each spectral band that can be used to estimate spectral reflectance of UAS DN images. The SCC method is demonstrated in the next section.

5.4 Results

The results of the proposed SCC method is presented in this section using a multispectral data set including UAS DN images and OLI SR data. The estimated UAS high-resolution reflectance images are compared with high-resolution NIS SR images for validation.

5.4.1 Reflectance Estimation of UAS DN Images

The multispectral dataset is shown in Fig. 5.5, including orthorectified high-resolution (1 m) UAS DN, resampled medium-resolution (30 m) UAS DN, and medium-resolution (30 m) OLI SR images for the NIR band. The high-resolution and the resampled medium-resolution UAS DN images share the same pixel range of 100-200 and the OLI SR image ranges from 0-0.6.

Pixel pairs are selected using the Pixel Selection method described in Sec. 3.1. In this chapter, the mean CV in the image X, $\bar{CV}$ is used as the threshold to perform this selection. Fig. 5.6 shows the selected pixels (circles) overlaid on the orthorectified and resampled UAS NIR DN image. As mentioned, the excluded pixels either represent high sub-pixel variability or shadows (example shown in Fig. 5.6).

OLS and WLS regression methods are tested on the selected pixel pairs for function identification. Fig. 5.7 shows the identified exponential cross-calibration functions using both methods for the NIR and Red bands. Note that exponential functions can be converted to linear functions by

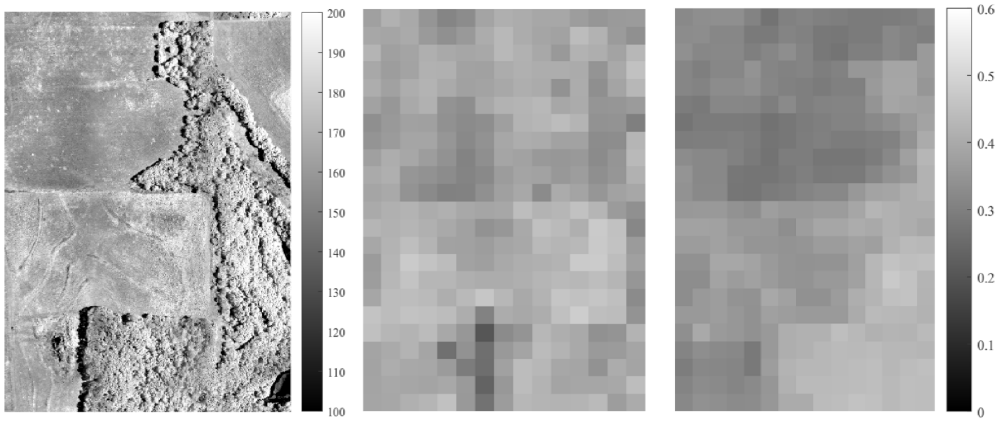

Figure 5.5: UAS and OLI NIR images of study area: orthorectifed high-resolution UAS DN image (L), resampled medium-resolution UAS DN image (M), and medium-resolution OLI SR image (R).

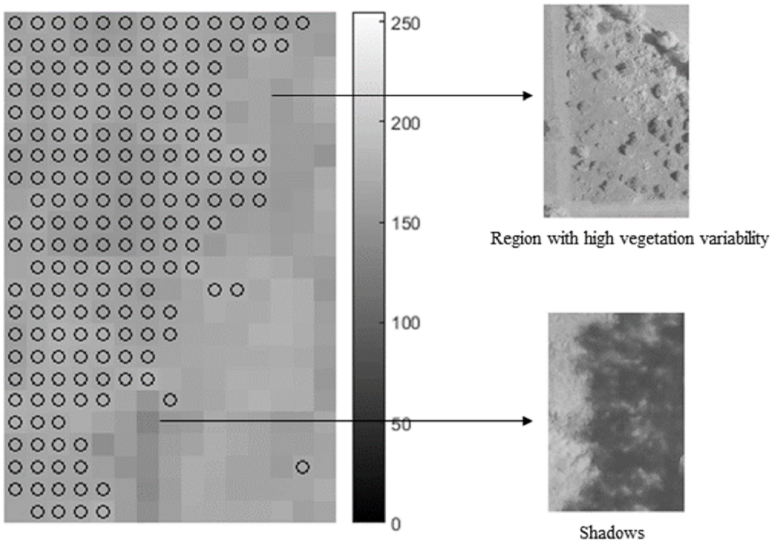

Figure 5.6: Selected sample pixels after pixel selection and example of excluded pixels.

taking the natural log on both sides of the equation.

In order to identify the optimal exponential function from the aforementioned regression methods, error residuals and error variances are analyzed. Fig. 5.8 shows the error residual plot for both methods, where the y-axis represents the error residual and x-axis (y_{hat}) represents the natural log of the estimated UAS reflectance. It can be observed that the WLS method results in smaller and more importantly, more consistent error variance as compared to OLS. The total error variance for NIR/Red bands were 0.0061/0.0156 and 0.0011/0.0025 for the OLS and WLS methods

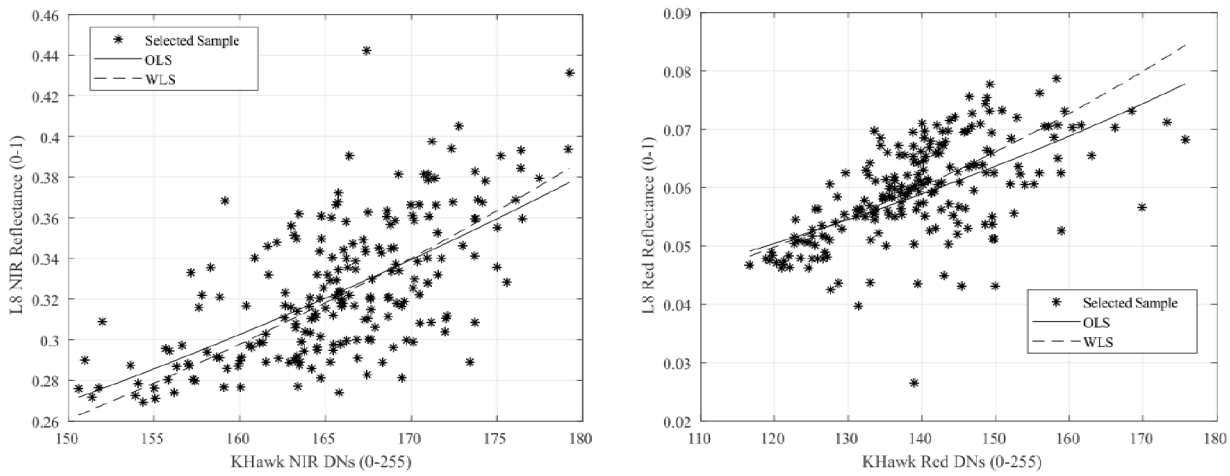

Figure 5.7: Identified cross-calibration function curves overlaid on selected sample for NIR (L) and Red (R) bands.

respectively. Therefore, the WLS method is selected for function identification. Table 5.3 shows the functions identified using the OLS and WLS methods. Here, x_i represents the UAS DN values and y_i represents the OLI SR values with $i = 1,2,3,...N$, where N is the total number of pixels in the selected pixel pairs. The identified functions are used to convert the high-resolution UAS DN images to spectral reflectance for the NIR and Red bands.

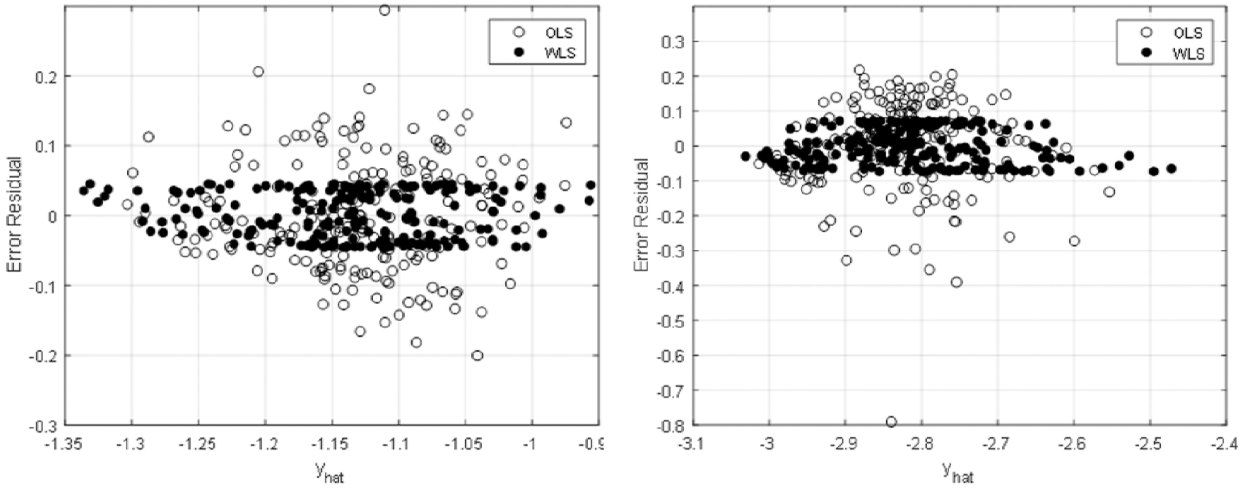

Figure 5.8: Error residuals for NIR (L) and Red (R) bands.

Table 5.3: Identified Functions Using the WLS Method.

Band	OLS	WLS
NIR	$y_i = 0.0483e^{0.0115x_i}$	$y_i = 0.0358e^{0.0132x_i}$
Red	$y_i = 0.0198e^{0.00078x_i}$	$y_i = 0.0160e^{0.00095x_i}$

5.4.2 Validation Using NIS Images

The estimated UAS reflectance images at 1 m spatial resolution are compared to NIS SR images at the same resolution for validation. Detailed analysis includes, 1) NEON data description, 2) effects of spectral and spatial resolution on reflectance, and 3) NIS and UAS reflectance comparison.

5.4.2.1 NEON Data Description

NEON is a continental-scale ecological observation facility project funded by NSF and operated by Battelle Memorial Institute [70]. NEON provides calibrated terrestrial, aquatic, atmospheric, and remote sensing data of 81 field sites across the United States to the scientific community, including the study area used in this chapter. The NEON aircraft is installed with a push broom collection style NIS, which was designed and built by NASA's Jet Propulsion Laboratory (JPL) for hyperspectral remote sensing. The NIS measures light at 426 spectral bands (with 5 nm spectral resolution) ranging from 380 to 2500 nm and produces orthorectified reflectance mosaics at a spatial resolution of 1 m [81]. The aircraft is flown once each year over the study area at an altitude of 1000 m above ground level. The orthorectified images used in this chapter correspond to a flyby on June 9, 2017 at 3:38 PM. Note that these images are atmospherically corrected using the ATCOR-4 algorithm.

5.4.2.2 Effect of Spectral and Spatial Resolutions on Reflectance

Difference in spectral and spatial resolutions can have an effect on the changes in reflectance between images from different remote sensing platforms. In order to use high-resolution NIS images for validation, consistency in reflectance between NIS and OLI SR images needs to be established.

NIS is a hyperspectral instrument and has a higher spectral resolution (narrower wavelength range) than the OLI. This can cause some inconsistencies between the reflectance images from both instruments. In order to minimize these differences, spectral convolution on the hyperspectral data can be performed to match the spectral response of the multispectral sensor [82–84]. In this chapter, a weighted-sum based spectral convolution method is used, where the spectral resolution of the hyperspectral data is transformed to a lower value [85, 86]. The weights are determined using the OLI prelaunch Relative Spectral Response (RSR) for the NIR and Red bands [87]. The equation used to perform the convolution is shown below:

$$\rho_i = \frac{\int_{\lambda_1}^{\lambda_2} \rho_0(\lambda)\ RSR_i(\lambda)\, d\lambda}{\int_{\lambda_1}^{\lambda_2} RSR_i(\lambda)\, d\lambda}, \tag{5.4}$$

where ρ_i is the spectrally convoluted NIS SR corresponding to band i, $\rho_0(\lambda)$ and $RSR_i(\lambda)$ are the NIS SR and the OLI spectral response of wavelength λ in band i respectively, λ_1 and λ_2 are the lower and upper wavelengths of the OLI spectral range for band i.

In addition to spectral resolution differences, which is an instrument-dependent factor, differences in spatial resolution (study area-dependent) can also cause reflectance inconsistencies between images from different platforms. [88] observed that images of uniform grasslands show consistency across different spatial resolutions. Similar patterns have also been observed in open grasslands with varying grass species [89]. Given these findings, the grass regions of the study area are expected to be consistent across different spatial resolutions. However, the tree regions may show differences due to factors such as canopy shadows and inter tree spacings, which are generally observed in finer detail in high-resolution images.

The rest of this subsection is focused on analyzing the effect of spectral and spatial resolutions on reflectance for the study area, including, 1) spectral resolution effect: comparison between resampled NIS and OLI images at 30 m resolution (shown in Fig. 5.9) and 2) spatial resolution effect: comparison between high-resolution (1 m) and resampled medium-resolution NIS images (30 m) for the grass and tree regions.

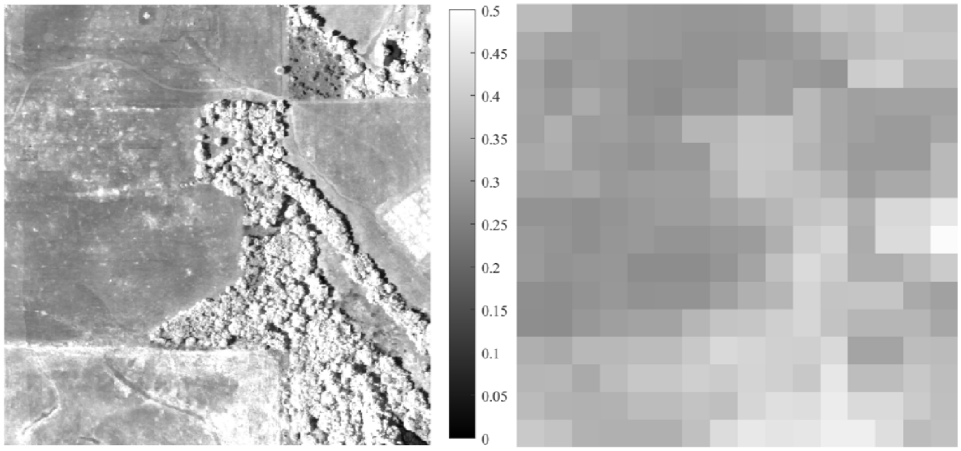

Figure 5.9: High-resolution NIS (L) and medium-resolution OLI NIR (R) images of study area.

Effect of Spectral Resolution Although the NIS images are spectrally convoluted using Eq. 4, some differences are still expected. The NIS NIR and Red SR images are resampled to 30 m resolution and compared to corresponding OLI images, shown in Fig. 5.10. It can be observed that while the NIR band shows high similarities for most of the points, a constant bias is seen in the Red band. The RMSE and mean percentage (MP) of the difference between images from the two sources are calculated for each band to be 0.0112 and -0.0043 for the NIR band and 0.0014 and -0.0274 for the Red band.

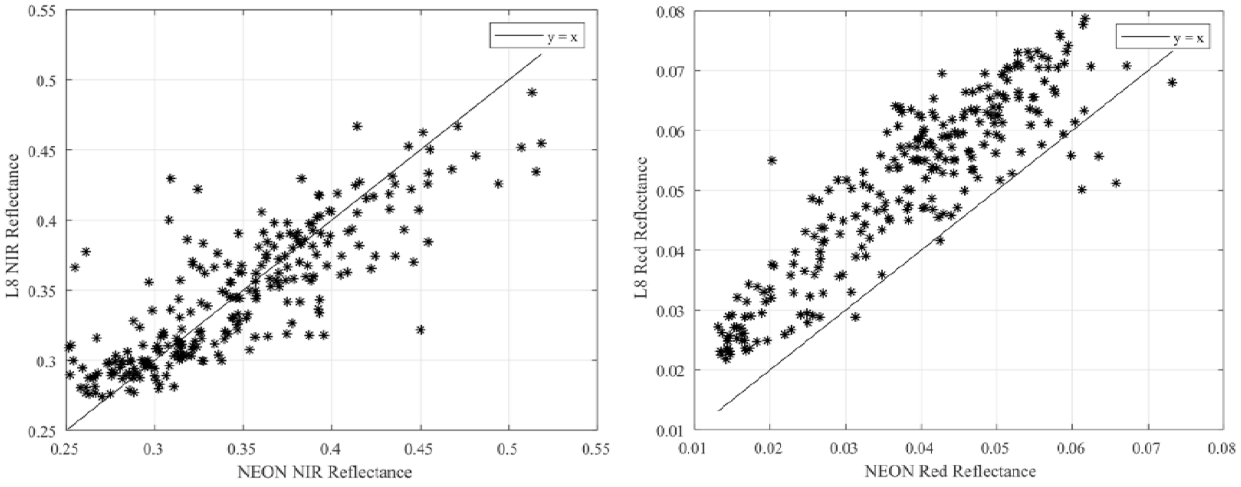

Figure 5.10: NIS and OLI SR comparisons for the NIR (L) and Red (R) bands.

Effect of Spatial Resolution The differences between the high-resolution (original) and resampled NIS images are calculated for the grass and tree areas separately. One pixel in the resampled NIS image is compared to the mean of the corresponding 30×30 pix. grid in the high-resolution NIS image. RMSE and MPE are calculated for each band and shown in Table 5.4. Additionally, sub-pixel variability within each 30×30 pix is also calculated using the CV. Mean CVs for grass and tree areas are also shown in Table 5.4.

Table 5.4: Effect of Spatial Resolution on Reflectance in Grass and Tree Areas.

Region	Mean CV (%)		RMSE		MPE (%)	
	NIR	Red	NIR	Red	NIR	Red
Grass	11.01%	17.17%	0.028	0.0073	0.1%	2.4%
Tree	30.85%	44.97%	0.040	0.0068	2.8%	8.8%

It can be observed that the grass areas show higher consistencies and lower CV than the trees. The change of spatial resolution has a small impact on the reflectance in grass areas, which also provides a justification for our proposed cross calibration method.

5.4.2.3 NIS and UAS Reflectance Comparison

The estimated UAS spectral reflectance images at 1 m spatial resolution are compared with NIS SR in detail in this section. First, the UAS images are registered with the NIS images using a point mapping technique in MATLAB [90]. This step is necessary to reduce errors due to misalignment between the two images. A projective transformation is performed on the UAS image using 12 selected control point pairs. The registered NIR and Red reflectance images from both platforms are shown in Fig. 5.11. Note that the black holes in the NIS images (close to the left boundary) and in the UAS Red image (right boundary) are caused by orthorectification and are not used for comparison. Two analyses are performed for comparison, 1) using a 32-subplot hayfield close to the northwest boundary and 2) using selected grass and tree regions.

Hayfield Comparison The 32-subplot hayfield serves as a good reference for comparison because, 1) the area is observed in images from both platforms and each subplot (grid size 10 m $\times$

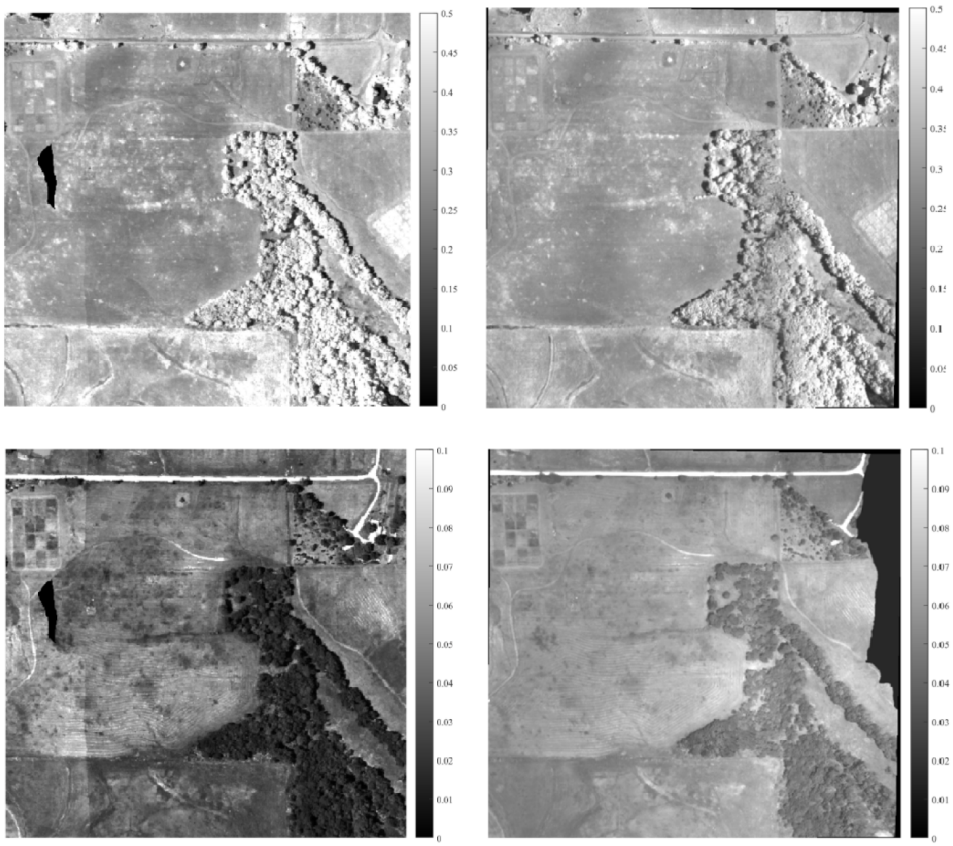

Figure 5.11: NIS (L) and UAS (R) spectral reflectance images in NIR (top) and Red (bottom) bands.

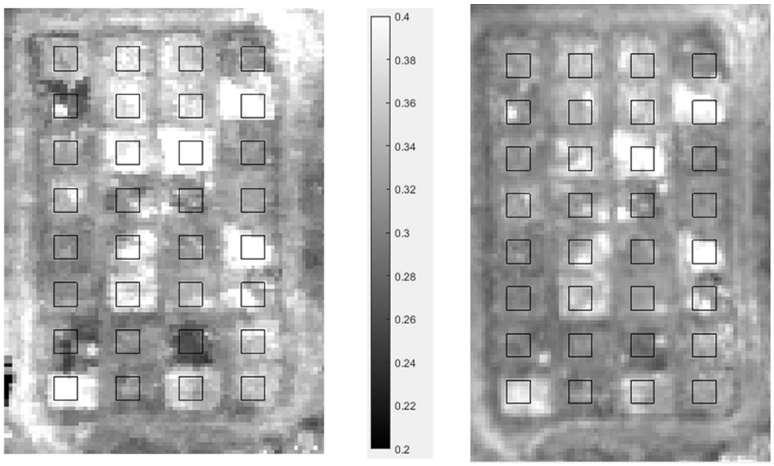

Figure 5.12: Hayfield in NIS (L) and UAS (R) NIR reflectance images (6 m $\times$ 6 m for each box).

10 m) is distinguishable, 2) the area is treated annually by KBS and the same treatment is given within each subplot, ensuring that the reflectance within each subplot is similar [91]. Fig. 5.12 shows the hayfield observed by the NIS (L) and UAS (R) NIR images. The black box in each

subplot represent a 6 m $\times$ 6 m window. All pixels within the window are averaged to produce one value per subplot.

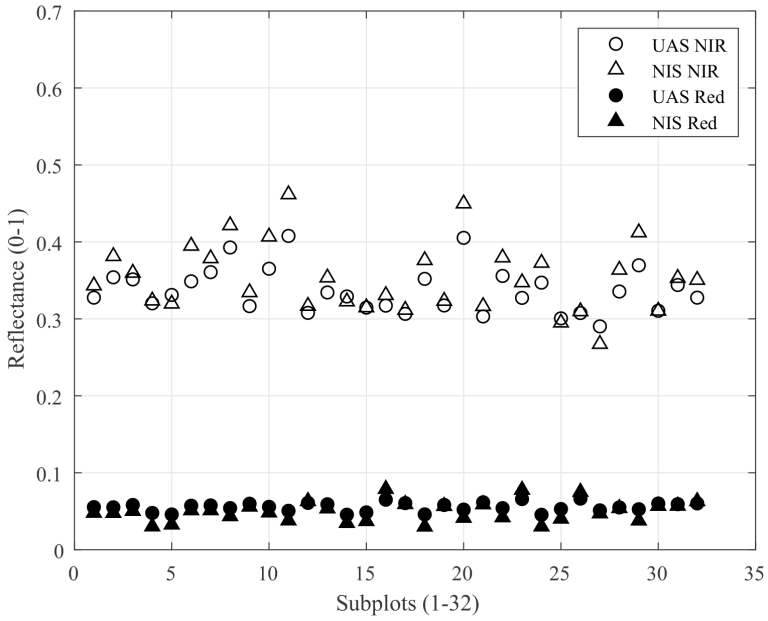

Figure 5.13: NIS and UAS reflectance values of the 32-subplot hayfield.

The averaged UAS and NIS SR values for each subplot are compared in Fig. 5.13. A good agreement can be observed between both images for the NIR and Red bands with high correlations of 97% and 95.74% and low RMSE of 0.0239 and 0.0096.

Selected Region Comparison In addition to the hayfield analysis, other regions in the area are also selected for NIS and UAS comparison. It is worth mentioning that comparing all the pixels between the two images is difficult here due to pixel alignment and georeferencing uncertainties. In fact, UAS orthorectified images are generated from many images and has a RMSE error of 10 m. Alternatively, six 3 m $\times$ 3 m regions are manually selected for comparison, including, three grass regions and three tree regions, shown in Fig. 5.14-5.15. The region size (3 m $\times$ 3 m) is selected based on the average tree canopy size observed in this data set. Note that shadows are excluded from the selected regions for a fair comparison. The six NIS and UAS reflectance values and differences between them are shown in Fig. 5.16 and Table 5.5 respectively. Mean absolute error (MAE) and RMSE were found to be 0.0243 and 0.0306 for the NIR band, and 0.0178 and

0.0163 for the Red band.

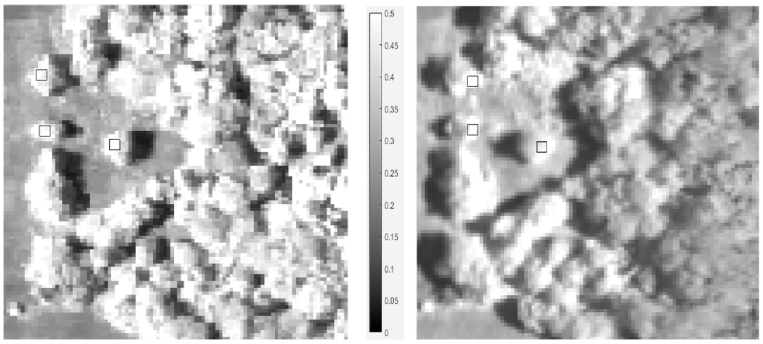

Figure 5.14: Selected tree regions in NIS (L) and UAS (R) NIR reflectance images (3 m $\times$ 3 m for each box).

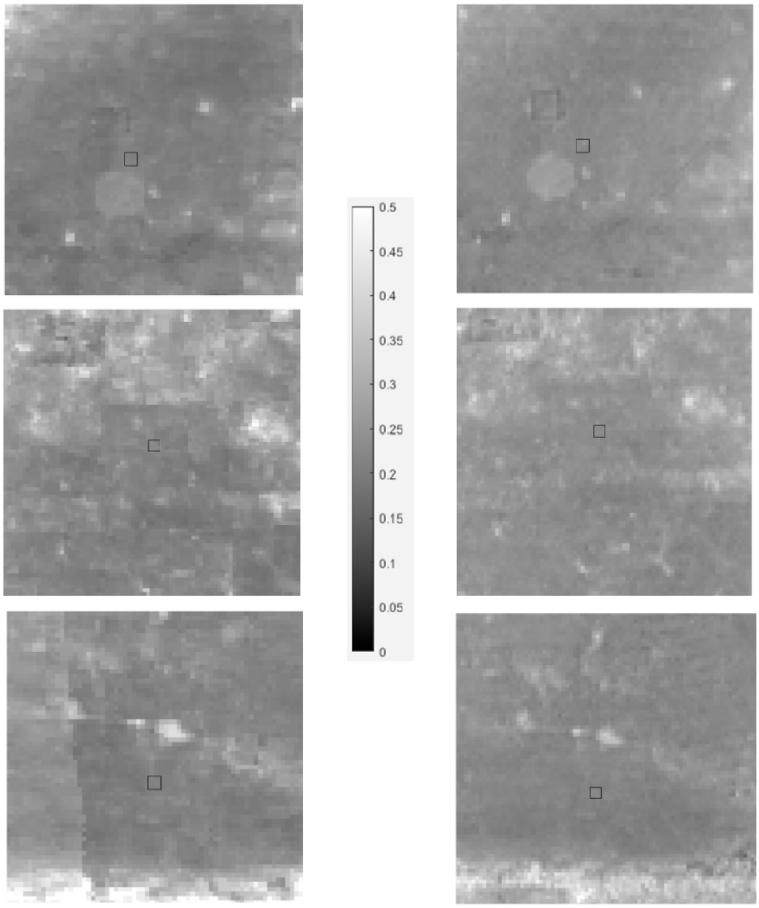

Figure 5.15: Selected grass regions in NIS (L) and UAS (R) NIR reflectance images (3 m $\times$ 3 m for each box).

Two trends can be observed from Table 5.5, 1) tree regions exhibit higher differences in both

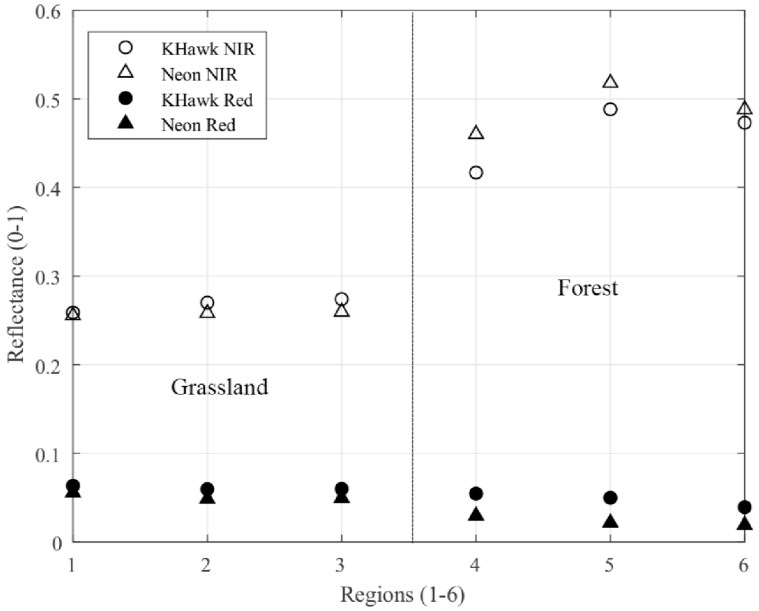

Figure 5.16: NIS and UAS reflectance values of the selected regions.

Table 5.5: Reflectance Differences between NIS and UAS.

Region	NIR			Red		
	NIS	UAS	Difference	NIS	UAS	Difference
Grass	0.2581	0.2595	0.0014	0.0577	0.0658	0.0082
Grass	0.2599	0.2736	0.0137	0.0487	0.0583	0.0096
Grass	0.2706	0.2787	0.0081	0.0501	0.0601	0.0100
Tree	0.4957	0.5454	0.0497	0.0343	0.0547	0.0204
Tree	0.5235	0.4762	-0.0473	0.0224	0.0476	0.0251
Tree	0.4860	0.5118	0.0258	0.0229	0.0473	0.0244

NIR and Red bands, 2) Red band shows slightly higher differences across most of the regions. These observations are similar to those found in Sec. 4.2.2.

In summary, the estimated UAS reflectance images showed high similarities with the NIS images in grass regions, and slightly lower similarities in the tree regions. This shows the potential of the proposed SCC method for other similar fields (e.g., dominant grassland), given the availability of an atmospherically corrected satellite reflectance image.

5.5 Discussions

The SCC method presented in this work provides an effective and low-cost solution for the spectral reflectance estimation of UAS DN images, under the assumption that there exists satellite SR data of the same area around the same time. The main advantage of this method is that UAS images can be converted to reflectance images without using ground reflectance target boards and expensive spectroradiometers. Apart from its contributions to the UAS community, the SCC method can also greatly benefit the satellite remote sensing community by establishing cross-calibration functions between UAS and satellites thus enabling future development of multisource and multi-scale data fusion.

Since the proposed method uses images from different instruments, co-registration accuracy, differences in spectral resolution [92] and differences in data acquisition conditions between UAS and satellite images can play a vital role in the accuracy of the function identification. Performing an accurate co-registration analysis between UAS and satellite images can be a challenging task considering the differences in their spatial resolutions (0.1 m and 30 m respectively). However, since the spatial accuracy of the UAS (4.72 m or better) and L8 OLI (12 m or better) images are smaller than the pixel size of the L8 OLI image, the impact of co-registration accuracy on the identified functions are not expected to be substantial. In this chapter, images from three sensors are used, namely, UAS GoPro, OLI, and NIS. Table 5.2 shows that the spectral characteristics between the GoPro and OLI sensors have low differences in peak wavelength (< 27 nm) for both bands (Table 5.2). The NIS SR data is spectrally convoluted to match the spectral response of the OLI sensor using (4). It can be observed from Fig. 5.10 that although the NIR images from the NIS and OLI sensors show high similarities, the Red images have some differences. Similar trends were also observed in [85], where the visible band images between NIS and OLI showed lower similarities. Additionally, the OLI and NIS SR data are subject to uncertainties of $5-10\%$ respectively [85], which can also cause differences between their respective SR images.

Conditions such as sun angle, clouds, and weather can also affect the accuracy of the proposed method. The ideal case is when the satellite and UAS images are acquired at the same time under

similar weather conditions. However, due to practical issues, images acquired a few days apart are also acceptable, especially during the growing season (Apr.-Sept.), when the weather conditions are similar. The UAS and OLI images used in this chapter were acquired on the same day (June 7, 2017) with the UAS NIR and RGB images acquired during 09:49-10:19 AM and 12:11-12:32 PM respectively, and the OLI images at 12:00 PM. The NIS image was acquired two days later, on June 9, 2017 at 03:38 PM. It can be observed from Fig. 5.14 that leaf canopy shadows are observed in opposite directions in NIS (towards east) and UAS (towards west) images. While the effect of shadows on the grass areas is not significant, more analysis is needed to understand why they affect the reflectance calculation for tree regions.

The proposed method is developed and tested on a forest/grassland area in Kansas which is dominated by tall grass and is expected to show small variations in reflectance values with changes in spatial resolution. This is further validated by comparing high-resolution and resampled medium-resolution NIS SR images.

It is worth mentioning that the proposed method can be implemented using any UAS camera and satellite, including, Sentinel, Planet, etc. Also, the NIS images are used in this chapter as a validation tool and is not required to implement the SCC method. In fact, this method showed its effectiveness in generating UAS reflectance image at 1 m/pix, only because the available images for validation are at that resolution. It can potentially be applied to UAS images at higher resolutions (< 0.1 m) also.

Lastly, the proposed method has the following constraints based on the current study: 1) requirement of atmospherically-corrected satellite reflectance data which can be used as a reference for the UAS survey. Note that airborne reflectance data such as NAIP or NEON can also be used when satellite data is not available, 2) the accuracy of the reference data and their acquisition time will have an impact on the calculated UAS reflectance, and 3) the effectiveness of this method has been demonstrated in a grassland/forest field and further investigations are required to evaluate its performance in more complex landscapes and other land cover areas such as crop fields.

5.6 Chapter Conclusion & Future Goals

In this chapter, a low-cost and novel SCC method is proposed for reflectance estimation of raw UAS DN images. This method only utilizes publicly available data without using ground calibration targets or expensive spectroradiometers, which makes it highly feasible for many UAS end users. The proposed method showed its effectiveness through a forest/grassland area, comprising of images from a fixed-wing UAS, L8 satellite, and NEON aircraft data. The estimated UAS NIR and Red reflectance images are validated by comparing with NIS SR images at high-resolution. High similarities are observed with reflectance differences less than 0.0137 and 0.01 for the grass regions and 0.0497 and 0.0251 for the tree regions.

Future objectives include: 1) testing the effectiveness of the proposed method with more complex landscapes and other land cover types using ground spectroscopy measurements for validation; 2) development of machine-learning based algorithms for the mapping from UAS raw DN to reflectance and validation in different types of landscapes; 3) investigating the effect of BRDF correction on UAS reflectance estimation; 4) comprehensive evaluation of this method on multiple data sets from different satellites such as Sentinel 2 and Planet.

Chapter 6

Conclusions and Future Recommendations

6.1 Conclusions

This dissertation focuses on the development of new UAS multispectral remote sensing methods for the mapping and measurement of the environment and natural disasters. The main goal is to enable a small UAS to accurately measure and visualize important disaster spatiotemporal metrics such as ROS, location, direction, intensity, etc. This can greatly improve the understanding of these disasters at fine resolutions which are often not possible in satellite or manned aircraft imagery. Each chapter in this dissertation addresses important problems and overcomes major challenges that currently limit the use of small UAS in such applications.

Chapter 2 describes important considerations for development of a UAS multispectral remote sensing system for disaster applications. The developed KHawk remote sensing system showed its effectiveness in several representative environment and disaster sensing missions including Kansas prescribed grass fire monitoring, Iowa tornado damage survey, and South Dakota damage survey. Chapter 3 focuses on the spatiotemporal mapping and ROS measurement of a Kansas prescribed grass fire using multitemporal thermal orthomosaics generated by images with limited footprints. Chapter 4 introduces a novel NIR-based fire detection method that uses raw NIR DN images to visualize the spatiotemporal dynamics of a grass fire. The methods demonstrated in this chapter can be highly beneficial to the UAS remote sensing community who use similar cameras. The UAS thermal and NIR measurements in chapters 3 and 4 showed that this grass fire had an ROS ranging from 0.01 - 0.44 ms^{-1}, which is the first UAS-based tallgrass fire measurements in the literature. Chapter 5 is dedicated to development of a low-cost UAS reflectance calibration method using

free and open satellite data. This is the first method in current literature that uses satellite data as a reference to calibrate UAS DN images to reflectance. This method showed its effectiveness through a forest/grassland data set, comprising of images from a fixed-wing UAS, L8 satellite, and NEON aircraft data. The grass regions in the field showed errors of 0.0137 and 0.01 and the tree regions showed errors of 0.0497 and 0.0251 for NIR and red images respectively.

6.2 Future Recommendations

Future research recommendations are suggested below.

1. UAS remote sensing system development:

    - Upgrade of the current KHawk UAS with high accuracy Real-time Kinematic (RTK) GPS and high accuracy Inertial Measurement Unit (IMU) for better position and orientation estimates. This will improve the spatial accuracy of UAS maps which will directly influence the accuracy of real-time disaster measurements;
    - Installation of light, detection, and ranging (LIDAR) systems for generation of accurate Digital Elevation Maps (DEM) and Digital Surface Maps;
    - In-situ sensors such as CO2, humidity, and temperature sensors to gather atmospheric measurements that is useful for smoke detection and UAS safe operation;

2. Fire location and ROS measurement:

    - Deploy multiple UAS and ground towers for fire mapping missions as sources of ground truth. For example, high altitude quadcopter for global view, ground watch towers, thermocouple arrays, etc.;
    - Extend the developed fire mapping methods to other types of wildland fires, such as forest fires;
    - Autonomous fire boundary following and real-time flight path adjustments based on real-time feedback from multispectral cameras;

- Near real-time fire mapping and ROS measurement for improved situational awareness.

3. UAS-Satellite Cross calibration:

    - Model relationships between different UAS cameras such as Micasense, Sentera, Tetracam and different satellites such as Sentinel, Planet, etc.;
    - Investigate the SCC methods on other field types, such as woodlands, short grass, etc.;
    - Use ground spectroradiometers to further evaluate the SCC method;
    - Machine Learning-based data fusion between UAS and satellites.

4. Other Considerations:

    - Investigate the influence of GPS, IMU, and camera alignment on image georeferencing accuracy;
    - Automatic feature-point based image registration instead of using manual selection.

References

[1] PeauProductions. (2017) Peaupro82 camera. [Online]. Available: https://www.peauproductions.com/products/peaupro82

[2] FLIR, "FLIR Vue Pro R," 2019, digital media. [Available online at https://www.flir.com/products/vue-pro-r/.].

[3] S. Gowravaram, "Multispectral remote sensing of the earth and environment using KHawk unmanned aircraft systems," Kansas, 2017.

[4] T. G. Bidwell and D. M. Engle, "Relationship of fire behavior to tallgrass prairie herbage production," *Rangeland Ecology & Management/Journal of Range Management Archives*, vol. 45, no. 6, pp. 579–584, 1992.

[5] X. Hu, M. Ge, S. Gowravaram, H. Chao, and M. Xin, "Simulating prescribed fire with multiple ignitions using data from UAS-based sensing," *Submitted for Review*, 2021.

[6] M. Gollner, A. Trouve, I. Altintas, J. Block, R. de Callafon, C. Clements, A. Cortes, E. Ellicott, J. Filippi, M. Finney *et al.*, "Towards data-driven operational wildfire spread modeling: A report of the NSF-funded wifire workshop," Tech. Rep., 2015.

[7] S. Wilfrid, P. Elaine, G. Louis, C. Ivan, S. Christopher, M. Jeffrey, and M. Douglas, "Validation of GOES and MODIS active fire detection products using ASTER and ETM+ data," *Remote Sensing of Environment*, vol. 112, no. 5, pp. 2711–2726, 2008.

[8] I. Csiszar, J. Morisette, and L. Giglio, "Validation of active fire detection from moderate-resolution satellite sensors: the MODIS example in northern Eurasia," *IEEE Transactions on Geoscience and Remote Sensing*, vol. 44, no. 7, pp. 1757–1764, 2006.

[9] I. Csiszar, W. Schroeder, L. Giglio, E. Ellicott, K. Vadrevu, C. Justice, and B. Wind, "Active fires from the suomi npp visible infrared imaging radiometer suite: Product status and first evaluation results," *Journal of Geophysical Research: Atmospheres*, vol. 119, no. 2, pp. 803–816, 2014.

[10] J. L. Coen and W. Schroeder, "Use of spatially refined satellite remote sensing fire detection data to initialize and evaluate coupled weather-wildfire growth model simulations," *Geophysical Research Letters*, vol. 40, no. 20, pp. 5536–5541, 2013.

[11] K. Badarinath, A. Sharma, and S. Kharol, "Forest fire monitoring and burnt area mapping using satellite data: a study over the forest region of Kerala state, India," *International Journal of Remote Sensing*, vol. 32, no. 1, pp. 85–102, 2011.

[12] D. Stow, P. Riggan, E. Storey, and L. Coulter, "Measuring fire spread rates from repeat pass airborne thermal infrared imagery," *Remote Sensing Letters*, vol. 5, no. 9, pp. 803–812, 2014.

[13] A. Ononye, A. Vodacek, and E. Saber, "Automated extraction of fire line parameters from multispectral infrared images," *Remote Sensing of Environment*, vol. 108, no. 2, pp. 179–188, 2007.

[14] P. Riggan, R. Tissell, R. Lockwood, J. Brass, J. Pereira, H. Miranda, A. Miranda, T. Campos, and R. Higgins, "Remote measurement of energy and carbon flux from wildfires in Brazil," *Ecological Applications*, vol. 14, no. 3, pp. 855–872, 2004.

[15] O. Viedma, J. Quesada, I. Torres, A. De Santis, and J. M. Moreno, "Fire severity in a large fire in a pinus pinaster forest is highly predictable from burning conditions, stand structure, and topography," *Ecosystems*, vol. 18, no. 2, pp. 237–250, 2015.

[16] O. Viedma, F. Chico, J. Fernández, C. Madrigal, H. Safford, and J. M. Moreno, "Disentangling the role of prefire vegetation vs. burning conditions on fire severity in a large forest fire in SE Spain," *Remote Sensing of Environment*, vol. 247, p. 111891, 2020.

[17] M. Valero, S. Verstockt, B. Butler, D. Jimenez, O. Rios, C. Mata, L. Queen, E. Pastor, and E. Planas, "Thermal infrared video stabilization for aerial monitoring of active wildfires," *IEEE Journal of Selected Topics in Applied Earth Observations and Remote Sensing*, vol. 14, pp. 2817–2832, 2021.

[18] P. McKenna, P. D. Erskine, A. M. Lechner, and S. Phinn, "Measuring fire severity using UAV imagery in semi-arid central Queensland, Australia," *International Journal of Remote Sensing*, vol. 38, no. 14, pp. 4244–4264, 2017.

[19] S. Reilly, M. L. Clark, L. P. Bentley, C. Matley, E. Piazza, and I. Oliveras Menor, "The potential of multispectral imagery and 3d point clouds from unoccupied aerial systems (UAS) for monitoring forest structure and the impacts of wildfire in mediterranean-climate forests," *Remote Sensing*, vol. 13, no. 19, p. 3810, 2021.

[20] S. Samiappan, L. Hathcock, G. Turnage, C. McCraine, J. Pitchford, and R. Moorhead, "Remote sensing of wildfire using a small unmanned aerial system: post-fire mapping, vegetation recovery and damage analysis in grand bay, Mississippi/Alabama, USA," *Drones*, vol. 3, no. 2, p. 43, 2019.

[21] R. H. Fraser, J. Van der Sluijs, and R. J. Hall, "Calibrating satellite-based indices of burn severity from UAV-derived metrics of a burned boreal forest in NWT, Canada," *Remote Sensing*, vol. 9, no. 3, p. 279, 2017.

[22] E. Beachly, C. Detweiler, S. Elbaum, D. Twidwell, and B. Duncan, "UAS-rx interface for mission planning, fire tracking, fire ignition, and real-time updating," in *2017 IEEE International Symposium on Safety, Security and Rescue Robotics (SSRR)*. IEEE, 2017, pp. 67–74.

[23] C. Yuan, Y. Zhang, and Z. Liu, "A survey on technologies for automatic forest fire monitoring, detection, and fighting using unmanned aerial vehicles and remote sensing techniques," *Canadian journal of forest research*, vol. 45, no. 7, pp. 783–792, 2015.

[24] S. Gowravaram, H. Chao, H. Flanagan, P. Tian, J. Goyer, M. Xin, and X. Hu, "Wildland fire monitoring and mapping using orthorectified near-infrared and thermal UAS imagery," in *American Meteorological Society Annual Meeting, 2021.*

[25] C. Moran, C. Seielstad, M. Cunningham, V. Hoff, R. Parsons, L. Queen, K. Sauerbrey, and T. Wallace, "Deriving fire behavior metrics from UAS imagery," *Fire*, vol. 2, no. 2, p. 36, 2019.

[26] X. Hu, Y. Sun, and L. Ntaimo, "Devs-fire: design and application of formal discrete event wildfire spread and suppression models," *Simulation*, vol. 88, no. 3, pp. 259–279, 2012.

[27] Mesonet, "Iowa environmental mesonet," 2021, digital media. [Available online at https://mesonet.agron.iastate.edu/sites/obhistory.php?station=OWI&network=KS_ASOS&metar=0&madis=0&year=2019&month=10&day=8&sortdir=asc.].

[28] ArduPilot, "The cube," 2021, digital media. [Available online at https://ardupilot.org/copter/docs/common-thecube-overview.html.].

[29] USDA, "Fire terminology," 2021, digital media. [Available online at https://www.fs.fed.us/nwacfire/home/terminology.html.].

[30] D. Stow, P. Riggan, G. Schag, W. Brewer, R. Tissell, J. Coen, and E. Storey, "Assessing uncertainty and demonstrating potential for estimating fire rate of spread at landscape scales based on time sequential airborne thermal infrared imaging," *International Journal of Remote Sensing*, vol. 40, no. 13, pp. 4876–4897, 2019.

[31] Y. Yang and X. Lee, "Four-band thermal mosaicking: A new method to process infrared thermal imagery of urban landscapes from UAV flights," *Remote Sensing*, vol. 11, no. 11, p. 1365, 2019.

[32] USDA, "National agriculture imagery program," 2009, digital media. [Available online at https://www.fsa.usda.gov.].

[33] NWCG. (2022) National wildfire coordinating group. [Online]. Available: https://www.nwcg.gov/

[34] R. C. Rothermel, *A mathematical model for predicting fire spread in wildland fuels*. Intermountain Forest & Range Experiment Station, Forest Service, US, 1972, vol. 115.

[35] M. Cruz, J. Gould, M. Alexander, A. Sullivan, W. McCaw, and S. Matthews, "A guide to rate of fire spread models for Australian vegetation. revised edition," 2015.

[36] J. H. Scott, *Standard fire behavior fuel models: a comprehensive set for use with Rothermel's surface fire spread model*. US Department of Agriculture, Forest Service, Rocky Mountain Research Station, 2005.

[37] N. Cheney, J. Gould, and W. R. Catchpole, "Prediction of fire spread in grasslands," *International Journal of Wildland Fire*, vol. 8, pp. 1–13, 1998.

[38] I. Noble, A. Gill, and G. Bary, "Mcarthur's fire-danger meters expressed as equations," *Australian Journal of Ecology*, vol. 5, no. 2, pp. 201–203, 1980.

[39] N. Cheney, J. Gould, and W. Catchpole, "The influence of fuel, weather and fire shape variables on fire-spread in grasslands," *International Journal of Wildland Fire*, vol. 3, no. 1, pp. 31–44, 1993.

[40] M. Finney, J. Cohen, I. Grenfell, and K. Yedinak, "An examination of fire spread thresholds in discontinuous fuel beds," *International Journal of Wildland Fire*, vol. 19, no. 2, pp. 163–170, 2010.

[41] E. Marino, J. Dupuy, F. Pimont, M. Guijarro, C. Hernando, and R. Linn, "Fuel bulk density and fuel moisture content effects on fire rate of spread: a comparison between firetec model predictions and experimental results in shrub fuels," *Journal of Fire Sciences*, vol. 30, no. 4, pp. 277–299, 2012.

[42] S. Gowravaram, H. Chao, T. Zhao, S. Parsons, X. Hu, M. Xin, H. Flanagan, and P. Tian, "Prescribed grass fire evolution mapping and rate of spread measurement using orthorectified thermal imagery from a fixed-wing UAS," *Submitted for Review*, 2021.

[43] S. Khanal, J. Fulton, and S. Shearer, "An overview of current and potential applications of thermal remote sensing in precision agriculture," *Computers and Electronics in Agriculture*, vol. 139, pp. 22–32, 2017.

[44] J. D. Burnett and M. G. Wing, "A low-cost near-infrared digital camera for fire detection and monitoring," *International journal of remote sensing*, vol. 39, no. 3, pp. 741–753, 2018.

[45] M. A. Akhloufi, T. Toulouse, and L. Rossi, "Multiple spectrum vision for wildland fires," in *Thermosense: Thermal Infrared Applications XL*, vol. 10661. International Society for Optics and Photonics, 2018, p. 1066105.

[46] KBS. (2022) Kansas biological survey. [Online]. Available: https://biosurvey.ku.edu/field-station

[47] S. Pyne, P. Andrews, and R. Laven, *Introduction to Wildland Fire*. John Wiley and Sons, 1996.

[48] R. C. Gonzalez, R. E. Woods, and B. R. MASTERs, *Digital image processing*. Society of Photo-Optical Instrumentation Engineers, 2009.

[49] M. Wagner *et al.*, "Unpiloted aerial systems (UASs) application for tornado damage surveys: Benefits and procedures," *Bulletin of the American Meteorological Society*, 2019.

[50] S. Gowravaram, P. Tian, H. Flanagan, J. Goyer, and H. Chao, "UAS-based multispectral remote sensing and NDVI calculation for post disaster assessment," in *2018 International Conference on Unmanned Aircraft Systems (ICUAS)*, 2018, pp. 684–691.

[51] A. Torres-Rua, M. A. Arab, L. Hassan-Esfahani, A. Jensen, and M. McKee, "Development of unmanned aerial systems for use in precision agriculture: The aggieair experience," in *2015 IEEE Conference on Technologies for Sustainability (SusTech)*, 2015, pp. 77–82.

[52] H. Niu, T. Zhao, D. Wang, and Y. Chen, "Evapotranspiration estimation with UAVs in agriculture: A review," 2019.

[53] T. Zhao, B. Stark, Y. Chen, A. L. Ray, and D. Doll, "A detailed field study of direct correlations between ground truth crop water stress and normalized difference vegetation index (NDVI) from small unmanned aerial system (sUASs)," in *2015 International Conference on Unmanned Aircraft Systems (ICUAS)*, 2015, pp. 520–525.

[54] L. Merino, F. Caballero, D. Martínez-de, J. Ramiro, I. Maza, and A. Ollero, "An unmanned aircraft system for automatic forest fire monitoring and measurement," *Journal of Intelligent & Robotic Systems*, vol. 65, no. 1, pp. 533–548, 2012.

[55] B. Stark, T. Zhao, and Y. Chen, "An analysis of the effect of the bidirectional reflectance distribution function on remote sensing imagery accuracy from small unmanned aircraft systems," in *2016 International Conference on Unmanned Aircraft Systems (ICUAS)*, 2016, pp. 1342–1350.

[56] J. Edwards, J. Anderson, W. Shuart, and J. Woolard, "An evaluation of reflectance calibration methods for UAV spectral imagery," *Photogrammetric Engineering & Remote Sensing*, vol. 85, pp. 221–230, 2019.

[57] B. Zaman, A. Jensen, S. R. Clemens, and M. McKee, "Retrieval of spectral reflectance of high resolution multispectral imagery acquired with an autonomous unmanned aerial vehicle," *Photogrammetric Engineering & Remote Sensing*, vol. 80, pp. 1139–1150, 2014.

[58] C. Wang and S. W. Myint, "A simplified empirical line method of radiometric calibration for small unmanned aircraft systems-based remote sensing," *IEEE Journal of Selected Topics in Applied Earth Observations and Remote Sensing*, vol. 8, pp. 1876–1885, 2015.

[59] L. Deng *et al.*, "A subband radiometric calibration method for UAV-based multispectral remote sensing," *IEEE Journal of Selected Topics in Applied Earth Observations and Remote Sensing*, vol. 11, pp. 2869–2880, 2018.

[60] D. Stow, A. Petersen, J. Rogan, and J. Franklin, "Mapping burn severity of mediterranean-type vegetation using satellite multispectral data," *Giscience & Remote Sensing*, vol. 44, pp. 1–23, 2007.

[61] S. Voigt *et al.*, "Satellite image analysis for disaster and crisis-management support," *IEEE Transactions on Geoscience and Remote Sensing*, vol. 45, pp. 1520–1528, 2007.

[62] L. Hassan-Esfahani, A. Ebtehaj, A. Torres-Rua, and M. McKee, "Spatial scale gap filling using an unmanned aerial system: A statistical downscaling method for applications in precision agriculture," *Sensors*, vol. 17, p. 2106, 2017.

[63] Y. Wang, D. Ryu, S. Park, S. Fuentes, and M. O'Connell, "Upscaling UAV-borne high-resolution vegetation index to satellite resolutions over a vineyard," in *2nd International Congress on Modelling and Simulation, Hobart, Tasmania, Australia*, vol. 3, 2017.

[64] P. Joan-Cristian, F.-J. Munoz, J. Planas, and X. Pons, "Comparison of four UAV georeferencing methods for environmental monitoring purposes focusing on the combined use with airborne and satellite remote sensing platforms," *International Journal of Applied Earth Observation and Geoinformation*, vol. 75, pp. 130–140, 2019.

[65] A. Matese *et al.*, "Intercomparison of UAV, aircraft and satellite remote sensing platforms for precision viticulture," *Remote Sensing*, vol. 7, pp. 2971–2990, 2015.

[66] S. Tuominen and A. Pekkarinen, "Local radiometric correction of digital aerial photographs for multi source forest inventory," *Remote Sensing of Environment*, vol. 89, pp. 72–82, 2004.

[67] D. Murugan, A. Garg, and D. Singh, "Development of an adaptive approach for precision agriculture monitoring with drone and satellite data," *IEEE Journal of Selected Topics in Applied Earth Observations and Remote Sensing*, vol. 10, no. 12, pp. 5322–5328, 2017.

[68] E. F. Berra, R. Gaulton, and S. Barr, "Commercial off-the-shelf digital cameras on unmanned aerial vehicles for multitemporal monitoring of vegetation reflectance and NDVI," *IEEE Transactions on Geoscience and Remote sensing*, vol. 55, no. 9, pp. 4878–4886, 2017.

[69] KBS. (2019) Kansas biological survey. [Online]. Available: https://biosurvey.ku.edu/field-station

[70] NEON. (2019) Airborne remote sensing. [Online]. Available: https://www.neonscience.org/

[71] ArcGIS. (2021) World imagery. [Online]. Available: https://www.arcgis.com/home/item

[72] NASA. (2019) NASA's earth observing system. [Online]. Available: https://eospso.nasa.gov/missions/landsat-8

[73] USGS. (2020) Landsat 8 collection 1 land surface reflectance code product guide. [Online]. Available: https://www.usgs.gov/media/files/

[74] NASA. (2021) Landsat science. [Online]. Available: https://landsat.gsfc.nasa.gov/landsat-8/landsat-8-overview

[75] M. Aboutalebi, A. F. Torres-Rua, W. P. Kustas, H. Nieto, C. Coopmans, and M. McKee, "Assessment of different methods for shadow detection in high-resolution optical imagery and evaluation of shadow impact on calculation of NDVI, and evapotranspiration," *Irrigation science*, vol. 37, pp. 407–429, 2019.

[76] StatisticsSolutions. (2020) Homoscedasticity. [Online]. Available: https://www.statisticssolutions.com/homoscedasticity

[77] L. Zhang, L. Yang, H. Lin, and M. Liao, "Automatic relative radiometric normalization using iteratively weighted least square regression," *International Journal of Remote Sensing*, vol. 29, pp. 459–470, 2008.

[78] Y. E. Shimabukuro and J. A. Smith, "The least-squares mixing models to generate fraction images derived from remote sensing multispectral data," *IEEE Transactions on Geoscience and Remote sensing*, vol. 29, no. 1, pp. 16–20, 1991.

[79] F. Nencini, L. Capobianco, and A. Garzelli, "Weighted least squares pan-sharpening of very high resolution multispectral images," in *IGARSS 2008-2008 IEEE International Geoscience and Remote Sensing Symposium*, vol. 5, 2008, pp. V–65.

[80] Mathworks. (2020) Least-squares fitting. [Online]. Available: https://www.mathworks.com/help/curvefit/.html

[81] NEON. (2020) About hyperspectral remote sensing data. [Online]. Available: https://www.neonscience.org/hyper-spec-intro

[82] H. Zhao, G. Jia, and N. Li, "Transformation from hyperspectral radiance data to data of other sensors based on spectral superresolution," *IEEE Transactions on Geoscience and Remote Sensing*, vol. 48, no. 11, pp. 3903–3912, 2010.

[83] P. Jarecke, P. Barry, J. Pearlman, and B. Markham, "Aggregation of hyperion hyperspectral spectral bands into landsat ETM+ spectral bands," in *IGARSS 2001. Scanning the Present and Resolving the Future. Proceedings. IEEE 2001 International Geoscience and Remote Sensing Symposium*, vol. 6, 2001, pp. 2822–2824.

[84] P. S. Barry, J. Mendenhall, P. Jarecke, M. Folkman, J. Pearlman, and B. Markham, "EO-1 hyperion hyperspectral aggregation and comparison with EO-1 advanced land imager and landsat 7 ETM+," in *IEEE International Geoscience and Remote Sensing Symposium*, vol. 3, 2002, pp. 1648–1651.

[85] M. Badawi, D. Helder, L. Leigh, and X. Jing, "Methods for earth-observing satellite surface reflectance validation," *Remote Sensing*, vol. 11, p. 1543, 2019.

[86] D. J. Meyer and G. Chander, "The effect of variations in relative spectral response on the retrieval of land surface parameters from multiple sources of remotely sensed imagery," in *IEEE International Geoscience and Remote Sensing Symposium*, 2007, pp. 5150–5153.

[87] NASA. (2020) Landsat8 spectral band viewer. [Online]. Available: https://landsat.usgs.gov/spectral-characteristics-viewer

[88] S. Goetz, "Multi-sensor analysis of NDVI, surface temperature and biophysical variables at a mixed grassland site," *International Journal of Remote Sensing*, vol. 18, pp. 71–94, 1997.

[89] Y. Liu *et al.*, "Using data from Landsat, MODIS, VIIRS and phenocams to monitor the phenology of california oak/grass savanna and open grassland across spatial scales," *Agricultural and Forest Meteorology*, vol. 237, pp. 311–325, 2017.

[90] MATLAB. (2020) Register images with projection distortion using control points. [Online]. Available: mathworks.com/help/images/registering-an-aerial-photo-to-an-orthophoto.html

[91] B. L. Foster *et al.*, "Integrated responses of grassland biodiversity and ecosystem properties to hay management: a field experiment," *Transactions of the Kansas Academy of Science*, vol. 113, pp. 103–120, 2010.

[92] P. Teillet, K. Staenz, and D. William, "Effects of spectral, spatial, and radiometric characteristics on remote sensing vegetation indices of forested regions," *Remote Sensing of Environment*, vol. 61, no. 1, pp. 139–149, 1997.